JETP Letters, Vol. 82, No. 3, 2005, pp. 101–104. From Pis'ma v Zhurnal Éksperimental'noĭ i Teoreticheskoĭ Fiziki, Vol. 82, No. 3, 2005, pp. 115–118.
Original English Text Copyright © 2005 by Vasiliev.

Determinant Formulas for Matrix Model Free Energy[¶]

D. Vasiliev
Alikhanov Institute for Theoretical and Experimental Physics, Moscow, 117218 Russia
Moscow Institute of Physics and Technology, Moscow, 117303 Russia
e-mail: vasiliev@itep.ru

Received June 17, 2005

The paper contains a new nonperturbative representation for the subleading contribution to the free energy of a multicut solution for a Hermitian matrix model. This representation is a generalization of the formula proposed by Klemm, Marino, and Theisen for a two-cut solution, which was obtained by comparing the cubic matrix model with the topological B-model on the local Calabi–Yau geometry $\widehat{II}$ and was checked perturbatively. In this paper, I give a direct proof of their formula and generalize it to the general multicut solution. © *2005 Pleiades Publishing, Inc.*

PACS numbers: 11.15.Pg, 11.15.Tk

1. INTRODUCTION

Interest in multicut solutions to matrix models was inspired by the studies in $\mathcal{N} = 1$ supersymmetric gauge theories of Cachazo, Intrilligator, and Vafa [1] and Dijkgraaf and Vafa [2–4], who proposed to calculate the nonperturbative superpotentials of $\mathcal{N} = 1$ SUSY gauge theories in four dimensions using the matrix model technique. These $\mathcal{N} = 1$ theories contain the multiplet of $\mathcal{N} = 2$ SUSY gauge theories but with a nontrivial tree superpotential. The nonperturbative superpotential could be obtained from the partition functions of the one-matrix model (1MM) in the leading order in $1/N$, N being the matrix size. Higher genus corrections are identified with certain holomorphic couplings of gauge theory to gravity.

The authors of [5] proposed a new ansatz for $\mathcal{F}_1$ in the two-cut case (with absent double points) and made a perturbative check. Their formula, in fact, comes from the correspondence between the so-called topological B-model on the local Calabi–Yau geometry $\widehat{II}$ and the cubic matrix model. Here, I give complete a proof of this formula and generalize it to the multicut case.

We start with a definition of the matrix integral and introduce all relevant constructions (for a complete review of the subject, see [6] and references therein). Consider the Hermitian one-matrix model:

$$\int\limits_{N \times N} DX \exp\left\{-\frac{1}{\hbar}\operatorname{tr}V(X)\right\} = e^{\mathcal{F}}, \tag{1}$$

where $V(X) = \sum_{n \geq 1} t_n X^n$, $\hbar = t_0/N$ is a formal expansion parameter and the integration goes over the $N \times N$ matrices, $DX \propto \prod_{ij} dX_{ij}$.

The topological expansion of the Feynman diagram series is then equivalent to the expansion in even powers of $\hbar$ for

$$\mathcal{F} \equiv \mathcal{F}(\hbar, t_0, t_1, t_2, \ldots) = \sum_{h=0}^{\infty} \hbar^{2h-2}\mathcal{F}_h. \tag{2}$$

Customarily, $t_0 = \hbar N$ is the scaled number of eigenvalues. We assume the potential $V(p)$ to be a polynomial of the fixed degree $m + 1$.

The averages, corresponding to the partition function (1), are defined as usual:

$$\langle f(X)\rangle = \frac{1}{Z}\int\limits_{N \times N} DX f(X) \exp\left(-\frac{1}{\hbar}\operatorname{tr}V(X)\right). \tag{3}$$

It is convenient to use their generating functionals: the one-point resolvent

$$W(\lambda) = \hbar\sum_{k=0}^{\infty}\frac{\langle \operatorname{tr}X^k\rangle}{\lambda^{k+1}} \tag{4}$$

and the s-point resolvents ($s \geq 2$)

$$W(\lambda_1, \ldots, \lambda_s) = \hbar^{2-s}\sum_{k_1, \ldots, k_s = 1}^{\infty}\frac{\langle \operatorname{tr}X^{k_1}\ldots\operatorname{tr}X^{k_s}\rangle_{\text{conn}}}{\lambda_1^{k_1+1}\ldots\lambda_s^{k_s+1}} \tag{5}$$

[¶] The text was submitted by the author in English.

0021-3640/05/8203-0101$26.00 © 2005 Pleiades Publishing, Inc.

$$= \hbar^{2-s}\left\langle \mathrm{tr}\frac{1}{\lambda_1 - X}\dots\mathrm{tr}\frac{1}{\lambda_s - X}\right\rangle_{\mathrm{conn}}.$$

The genus expansion of the resolvent has the form

$$W(\lambda_1, \dots, \lambda_s) = \sum_{h=0}^{\infty}\hbar^{2h}W_h(\lambda_1, \dots, \lambda_s), \quad s \ge 1. \qquad (6)$$

It satisfies the loop equation [7, 8]:

$$[V'(x)W(x)]_- = W(x)^2 + \hbar^2 W(x, x), \qquad (7)$$

where $[\dots]_-$ is the projector on the negative powers. In genus zero, the loop equations have the solution

$$W_0(\lambda) = \frac{1}{2}(V'(\lambda) - y) \qquad (8)$$

$$y^2 = V'(\lambda)^2 + 4P_{m-1}(\lambda), \qquad (9)$$

where P_{m-1} is an arbitrary polynomial of degree $m-1$. If curve (9) has n cuts, it can be represented in terms of branching points μ_α:

$$y \equiv M(\lambda)\tilde{y} \equiv M(\lambda)\sqrt{\prod_{\alpha=1}^{2n}(\lambda - \mu_\alpha)}. \qquad (10)$$

In this article, I concentrate on the case with $m = n$ (without double points; i.e., $M(\lambda)$ is a constant). Thus, the full set of moduli is $t_I \equiv \{S_i, t_0, t_k\}$, $i = \overline{1, n-1}$, $k = \overline{1, n}$, where occupancy numbers S_i are defined as integrals over A-cycles on the curve y,

$$S_i \equiv \frac{1}{4\pi i}\oint_{A_i} y\, d\lambda. \qquad (11)$$

To construct $\mathcal{F}_1$, we also define the polynomials $H_I(\lambda)$,

$$\frac{dy}{dt_I} = \frac{H_I(\lambda)}{y(\lambda)}, \qquad (12)$$

and matrix $\sigma_{i,j}$,

$$\sigma_{j,i} \equiv \oint_{A_j}\frac{\lambda^{i-1}}{y(\lambda)}d\lambda, \quad i, j = \overline{1, n-1}. \qquad (13)$$

It can be shown [6] that, for polynomials $H_k(\lambda) \equiv \sum_{l=1}^{n-1} H_{l,k}\lambda^{l-1}$, $k = \overline{1, n-1}$ corresponded S_k,

$$\sum_{l=1}^{n-1}\sigma_{j,l}H_{l,k} = \delta_{j,k} \quad \text{for} \quad j, k = \overline{1, n-1}. \qquad (14)$$

2. TWO-CUT CASE

According to paper [5], the holomorphic part of the genus one B-model amplitude is, up to an additive constant,

$$\mathcal{F}_1 = \frac{1}{2}\log\left(\det\left(\frac{\partial\mu_i^-}{\partial S_j}\right)\Delta^{2/3}\frac{2}{\mu_2^+ - \mu_1^+}\right), \qquad (15)$$

where $\mu_1^- = \frac{1}{2}(\mu_1 - \mu_2)$, $\mu_2^- = \frac{1}{2}(\mu_3 - \mu_4)$, $\mu_1^+ = \frac{1}{2}(\mu_1 + \mu_2)$, and $\mu_2^+ = \frac{1}{2}(\mu_3 + \mu_4)$. On the other hand, there is an answer for $\mathcal{F}_1$ obtained directly from solving the loop equations (7) for matrix model [9, 10] or using conformal field theory technique [11, 12]:

$$\mathcal{F}_1 = -\frac{1}{24}\log\left(\prod_{\alpha=1}^{2n}M(\mu_\alpha)\Delta^4(\det_{i,j}\sigma_{j,i})^{12}\right), \qquad (16)$$

which, in the two-cut case without double points, reads as

$$\mathcal{F}_1 = -\frac{1}{24}\log(\Delta^4\sigma^{12}), \qquad (17)$$

where σ (13) is a 1×1 matrix. To obtain (15) from (17), one should prove the following formula:

$$\det\left(\frac{\partial\mu_i^-}{\partial S_j}\right)\Delta\frac{2}{\mu_3 + \mu_4 - \mu_1 - \mu_2}\sigma = 1. \qquad (18)$$

We can explicitly find the derivatives $\partial S_i/\partial\mu_j^-$ (instead of $\partial\mu_j^-/\partial S_j$), keeping times t_k constant. To do so, one should first write $\partial S_i/\partial\mu_j$, then make the change of variables from $\{\mu_1, \mu_2, \mu_3, \mu_4\}$ to $\{t_1, t_2, \mu_1^-, \mu_2^-\}$. Then,

$$\frac{\partial S_i}{\partial\mu_j^-} = \frac{\partial S_i}{\partial\mu_k}\frac{\partial\mu_k}{\partial\mu_j^-}, \quad i, j = \overline{1, n}, \quad k = \overline{1, 2n}, \qquad (19)$$

$\partial\mu_k/\partial\mu_j^-$ here are obtained by inverting the matrix $\left(\frac{\partial\mu_j^-}{\partial\mu_k}, \frac{\partial S_j}{\partial\mu_k}\right)$. After this, it is easy to rewrite (18) using elliptic integrals:

$$\sqrt{\frac{\mu_4 - \mu_2}{\mu_3 - \mu_1}}\left(\frac{\mu_4 - \mu_1}{\mu_4 - \mu_2}\Pi\left(-\frac{\mu_2 - \mu_1}{\mu_4 - \mu_2}, \kappa\right)\right.$$
$$\left. + \frac{\mu_3 - \mu_2}{\mu_4 - \mu_2}\Pi\left(\frac{\mu_4 - \mu_3}{\mu_4 - \mu_2}, \kappa\right) + K(\kappa)\right) = \frac{\pi}{2}, \qquad (20)$$

where $\kappa = \sqrt{\frac{(\mu_2 - \mu_1)(\mu_4 - \mu_3)}{(\mu_4 - \mu_2)(\mu_3 - \mu_1)}}$ and $\Pi(\nu, \kappa)$ and $K(\kappa)$ are complete elliptic integrals of the third and first kinds, respectively. To prove this statement, one can rewrite the elliptic integrals of the third kind via the complete and incomplete elliptic integrals of the first and the second kinds (these formulas can be found in [13] (formulas (22), (24) from Chapter 13.8); note, however, that, in [13], there is a misprint in these formulas):

$$k'^2\frac{\sin\theta\cos\theta}{\sqrt{1-k'^2\sin\theta^2}}[\Pi(1-k'^2\sin\theta^2,\kappa)-K(\kappa)]$$
$$=\frac{\pi}{2}-(E(\kappa)-K(\kappa))F(\sin\theta,k')-K(\kappa)E(\sin\theta,k'),\tag{21}$$

$$\frac{\sqrt{1-k'^2\sin\theta^2}}{\sin\theta\cos\theta}[\Pi(-k'^2\tan\theta^2,\kappa)-K(\kappa)\cos\theta^2]$$
$$=(E(\kappa)-K(\kappa))F(\sin\theta,k')-K(\kappa)E(\sin\theta,k'),\tag{22}$$

where $k' = \sqrt{1-k^2}$, $\theta \in [0, \pi/2]$. In this case, one should put $\sin^2\theta = (\mu_3 - \mu_1)/(\mu_4 - \mu_1)$.

The same computation can be performed for any other partition of μ_i into the two sets $\mu^{\pm}_{1,2}$ (without changing σ), say, for $\mu_1^- = \frac{1}{2}(\mu_1 - \mu_3)$, $\mu_2^- = \frac{1}{2}(\mu_2 - \mu_4)$, $\mu_1^+ = \frac{1}{2}(\mu_1 + \mu_3)$, and $\mu_2^+ = \frac{1}{2}(\mu_2 + \mu_4)$. It leads to the same result (15); however, the perturbative calculation in this case is irrelevant.

3. GENERALIZATION FOR *n*-CUT SOLUTION

A natural generalization of (15) is

$$\mathcal{F}_1 = \frac{1}{2}\log\left(\det\left\|\frac{\partial\{\mu_j^-\}}{\partial\{S_i, S_n\}}\right\|\Delta^{2/3}\Delta^{-1}(\mu_j^+)\right),\tag{23}$$

where we have divided all the branching points into two ordered sets $\{\mu_j^{(1)}\}_{j=1}^n$ and $\{\mu_j^{(2)}\}_{j=1}^n$ and performed a linear orthogonal transformation of $\mu_j^{(1,2)}$ to the quantities $\{\mu_j^+\}$ and $\{\mu_j^-\}$, $j = \overline{1, n}$,

$$\mu_j^{\pm} = \mu_j^{(1)} \pm \mu_j^{(2)}.\tag{24}$$

To prove formula (23), one should calculate the derivative of the branching points μ_j with respect to the moduli $\{t_K\} \equiv \{S_1 \ldots S_{n-1}, t_0 \ldots t_n\}$ [6]:

$$\frac{\partial\mu_\alpha}{\partial t_K} = \frac{H_K(\mu_\alpha)}{M(\mu_\alpha)\prod\limits_{\beta\neq\alpha}(\mu_\alpha-\mu_\beta)}.\tag{25}$$

The polynomials $H_I(\lambda)$ corresponding to the variables t_k, $k \geq 1$, always have the coefficient k at the highest term λ^{n-1+k} and the polynomial corresponding to t_0 starts with λ^{n-1}. Therefore, one can find the determinant:

$$\det\left\|\frac{\partial\{\mu_{\alpha_j}\}}{\partial\{S_i, S_n, t_k\}}\right\|$$
$$=\frac{\Delta(\mu_{\alpha_j})(\det\limits_{l,m}\sigma_{l,m})^{-1}}{\prod\limits_{i=1}^{2n}M(\mu_{\alpha_i})\prod\limits_{j=1}^{2n}\left(\prod\limits_{\beta\neq\alpha_j}^{2n}(\mu_{\alpha_j}-\mu_\beta)\right)}.\tag{26}$$

Indeed, consider the left-hand side of (26):

$$\det\left\|\frac{\partial\{\mu_{\alpha_j}\}}{\partial\{S_i, S_n, t_k\}}\right\|$$
$$=\frac{(\det\limits_{K,j}H_K(\mu_{\alpha_j}))}{\prod\limits_{i=1}^{2n}M(\mu_{\alpha_i})\prod\limits_{j=1}^{2n}\left(\prod\limits_{\beta\neq\alpha_j}^{2n}(\mu_{\alpha_j}-\mu_\beta)\right)}.\tag{27}$$

The change of variables $\{S_1, \ldots, S_n\} \longrightarrow \{S_1, \ldots, S_{n-1}, t_0\}$ does not change the determinant. To obtain the Vandermonde determinant on the right-hand side of (26), there should be, instead of the polynomials H_K, polynomials of degree $2n - i + 1$, where i is the line number, with unit leading coefficients. To this end, one should multiply the matrix $H_K(\mu_{\alpha_j})$ by the block diagonal matrix

$$\tilde{\sigma} = \begin{pmatrix} 1 & 0 \\ 0 & \sigma \end{pmatrix}.\tag{28}$$

This gives the factor $(\det\tilde{\sigma})^{-1} = (\det\limits_{l,m}\sigma_{l,m})^{-1}$. Lines from 1 to $n + 1$ contribute to $n!$, which can be omitted from the free energy. The Vandermonde determinant $\Delta(\mu_{\alpha_j})$ then combines with the rational factors in the denominator to produce $(-1)^{\sum_{j=1}^n\alpha_j}\Delta(\overline{\mu_{\alpha_j}})/\Delta(\mu)$, where $\Delta(\overline{\mu_{\alpha_j}})$ is the Vandermonde determinant for the supplementary set of n branching points not entering the set $\{\mu_{\alpha_j}\}_{j=1}^n$, whereas $\Delta(\mu)$ is the total Vandermonde determinant. Now, we should put $M(\mu_\alpha)$ a constant independent of α. Expanding the determinant in (23) by each line and neglecting the additive constant $\frac{1}{2}\log 2^n$, one obtains (16).

Introducing the quantities

$$\phi_I^\alpha \equiv \frac{H_I(\mu_\alpha)}{M^{1/3}(\mu_\alpha)\prod\limits_{\beta\neq\alpha}(\mu_\alpha-\mu_\beta)^{2/3}},\tag{29}$$

one can rewrite (16) in a simpler form:

$$\mathscr{F}_1 = \frac{1}{2}\log\left(\det_{I,\alpha}\phi_I^{\alpha}\right). \tag{30}$$

4. PERTURBATIVE FORMULA

We have also performed a perturbative check of (23) for the three-cut case. It is easier to make the expansion not in the moduli S_i but in the difference of the branching points μ_j^-. In order to calculate $\det\|\partial\{S_i, S_n\}/\partial\{\mu_j^-\}\|$, one should rewrite S_i and $\sigma_{i,j}$ in terms of μ_i^+, μ_j^- and expand them in μ_i^-:

$$S_l = \frac{1}{2}\mathrm{res}_{\lambda=\mu_l^+}\prod_{i=1}^{n}\sum_{k=0}^{\infty}\frac{(\mu_i^-)^{2k}c_k}{(\lambda-\mu_i^+)^{2k-1}}, \tag{31}$$

$$\sigma_{l,j} = \frac{1}{2}\mathrm{res}_{\lambda=\mu_l^+}\lambda^{j-1}\prod_{i=1}^{n}\sum_{k=0}^{\infty}\frac{(\mu_i^-)^{2k}\tilde{c}_k}{(\lambda-\mu_i^+)^{2k+1}}, \tag{32}$$

where c_k and $\tilde{c}_k$ are the Taylor coefficients for $\sqrt{1-x}$ and $1/\sqrt{1-x}$, respectively. It should be mentioned that derivatives $\partial\{S_i\}/\partial\{\mu_j^-\}$ are taken at t_k constant, while, in (31), S_k are functions of μ^+, μ^-. This problem is solved by calculating the transition matrix from $\{\mu_k^-, t_k\}$ to $\{\mu_k^-, \mu_k^+\}$ and inverting it. We have performed this calculation up to $(\mu^-)^3$ and found it to be in perfect agreement with (16) (up to the additive constant already mentioned).

This work was supported in part by the Federal Program of the Russian Ministry of Industry, Science, and Technology (grant no. 40.052.1.1.1112) and by the Russian Foundation for Basic Research (project no. 04-02-16880).

REFERENCES

1. F. Cachazo, Kenneth A. Intriligator, and C. Vafa, Nucl. Phys. B **603**, 3 (2001).
2. R. Dijkgraaf and C. Vafa, Nucl. Phys. B **644**, 3 (2002).
3. R. Dijkgraaf and C. Vafa, Nucl. Phys. B **644**, 21 (2002).
4. R. Dijkgraaf and C. Vafa, hep-th/0208048 (2002).
5. A. Klemm, M. Marino, and S. Theisen, J. High Energy Phys. **03**, 051 (2003).
6. L. Chekhov, A. Marshakov, A. Mironov, and D. Vasiliev, hep-th/0506075 (2005).
7. Yu. Makeenko, Mod. Phys. Lett. A **6**, 1901 (1991).
8. A. A. Migdal, Phys. Rep. **102**, 199 (1983).
9. G. Akemann, Nucl. Phys. B **482**, 403 (1996).
10. L. Chekhov, Theor. Math. Phys. **141**, 1640 (2004).
11. I. K. Kostov, hep-th/9907060 (1999).
12. R. Dijkgraaf, A. Sinkovics, and M. Temurhan, Adv. Theor. Math. Phys. **7**, 1155 (2004).
13. *Higher Transcendental Functions (Bateman Manuscript Project)*, Ed. by A. Erdelyi (McGraw-Hill, New York, 1955; Nauka, Moscow, 1967), Vol. 3.

JETP Letters, Vol. 82, No. 3, 2005, pp. 105–109. Translated from Pis'ma v Zhurnal Éksperimental'noĭ i Teoreticheskoĭ Fiziki, Vol. 82, No. 3, 2005, pp. 119–123.

Self-Action Dynamics of Ultrashort Electromagnetic Pulses

A. G. Litvak, V. A. Mironov, and S. A. Skobelev*

Institute of Applied Physics, Russian Academy of Sciences, Nizhni Novgorod, 603950 Russia

** e-mail: sksa@ufp.appl.sci-nnov.ru*

Received June 9, 2005; in final form, June 29, 2005

The self-action dynamics of three-dimensional wave packets whose width is on the order of the carrier frequency is studied under fairly general assumptions concerning the dispersion properties of the medium. The condition for the wave field collapse is determined. Self-action regimes in a dispersion-free medium and in media with predominance of anomalous or normal group velocity dispersions are numerically investigated. It is shown that, for extremely short pulses, nonlinearity leads not only to the self-compression of the wave field but also to a "turn-over" of the longitudinal profile. In a dispersionless medium, the formation of a shock front within the pulse leads to the nonlinear dissipation of linearly polarized radiation and to self-focusing stabilization. For circularly polarized radiation, the wave collapse is accompanied by the formation of an envelope shock wave. *© 2005 Pleiades Publishing, Inc.*

PACS numbers: 41.20.Jb, 42.65.–k

The development of optical methods for the generation of attosecond [1] and terahertz [2] pulses calls for a theoretical study of the self-action dynamics of wave fields whose spectral width is on the order of their carrier frequency. The approximation of a slowly varying envelope of the wave field is insufficient for describing the propagation of a femtosecond ionizing laser pulse in the atmosphere, which is accompanied by a considerable broadening of its spectrum [3]. One of the simplest generalizations of the three-dimensional nonlinear Schrödinger equation for pulses with durations of several periods of the field oscillations is as follows [4–6]:

$$\frac{\partial}{\partial\tau}\left(\frac{\partial u}{\partial z}+3u^2\frac{\partial u}{\partial\tau}-b\frac{\partial^3 u}{\partial\tau^3}-\gamma\frac{\partial^2 u}{\partial\tau^2}\right)+au = \Delta_\perp u. \quad (1)$$

This equation describes the reflectionless propagation of broadband radiation $u(z, \tau = t - z, \mathbf{r})$ along the z axis with a group velocity, where $\mathbf{r}$ is a vector perpendicular to the z axis. The parameters a, b, and γ determine the low-frequency and high-frequency dispersions of the medium and the dissipation of the radiation [4]. The scale invariance of this equation allows its representation in form (1). The dimensionless coordinates are expressed in terms of the respective characteristic (spatial and temporal) scales of the problem. The field $u(\mathbf{r}, \mathbf{z}, \tau)$ is dimensionless and normalized to the characteristic nonlinear field. In the absence of dispersion in the medium ($a = b = 0$), Eq. (1), in particular, describes the self-action of shear acoustic wave fields [5]. As applied to nonlinear acoustics, Eq. (1) represents a generalization of the modified Burgers equation to the case of three-dimensional wave fields. For $\gamma = 0$ and $a = 0$, Eq. (1) has the form of a generalized Kadomtsev–Petviashvili equation, which is used to describe the evolution of finite-amplitude elastic waves in magnets [6].

For the electromagnetic radiation under consideration, parameters a and b determine the group velocity dispersion of the wave field in a wide frequency range [7]. From the linear dispersion relation $k = k_z(\omega)$ (k_z is the wave number, ω is the wave frequency, and $u \sim \exp(i\omega t - ik_z z)$), for the parameters of the group velocity dispersion, we find $\partial^2 k/\partial\omega^2 = 6b\omega - 2a/\omega^3$. From this expression, one can see that, at $a = 0$ and $b > 0$, Eq. (1) describes the self-action dynamics of ultrashort pulses in a medium with a normal dispersion ($\partial^2 k/\partial\omega^2 > 0$). The other limiting case with $b = 0$ and $a > 0$ corresponds to a medium with an anomalous dispersion ($\partial^2 k/\partial\omega^2 < 0$). By choosing the central frequency of the broadband radiation, it is possible to control the role of the dispersion in the dynamics of the system. In particular, for the central frequency $\bar{\omega} = (a/3b)^{1/4}$, the group velocity dispersion proves to be zero.

Another distinctive feature of the equation under consideration is related to the nonlinear term in Eq. (1). In the framework of the slowly varying amplitude approach, this term corresponds to a cubic nonlinearity. As the pulse duration decreases, the dependence of the group velocity on amplitude (the nonlinear dispersion) becomes the governing factor. In the one-dimensional case ($\Delta_\perp = 0$), this nonlinearity determines the modification of the wave field profile and the shock front formation. Evidently, self-compression of the wave packet in the transverse direction should enhance wavebreaking effects.

In this paper, we consider the space–time evolution of non-one-dimensional packets of broadband radiation. First, we derive a number of analytical relations, which allow us to qualitatively analyze the characteristic features of the self-action dynamics of wave fields on the basis of Eq. (1). Then we present the results of the corresponding numerical study.

1. We consider the conservative case ($\gamma = 0$) and pass from Eq. (1) to the equation for the potential Φ of the field $u = \Phi_\tau$. As a result, for the localized distribution of Φ, by integrating Eq. (1), we obtain the equation

$$\frac{\partial^2\Phi}{\partial z\partial\tau} + \frac{\partial}{\partial\tau}(\Phi_\tau)^3 - b\frac{\partial^4\Phi}{\partial\tau^4} = \Delta_\perp\Phi - a\Phi, \qquad (2)$$

which is more convenient for the qualitative study of the wave packet dynamics. We write the Lagrange function density corresponding to Eq. (2):

$$L = \frac{1}{2}\Phi_z\Phi_\tau + \frac{\Phi_\tau^4}{4} + \frac{b}{2}\Phi_{\tau\tau}^2 - \frac{1}{2}(\nabla_\perp\Phi)^2 - a\frac{\Phi^2}{2}. \qquad (3)$$

This allows us to determine some integral relations that are conserved in the process of evolution of the system:

$$I = \int\Phi_\tau^2 d\tau d\mathbf{r}_\perp, \qquad (4)$$

$$H = \int\left((\nabla_\perp\Phi)^2 - b\Phi_{\tau\tau}^2 - \frac{1}{2}\Phi_\tau^4 + a\Phi^2\right)d\tau d\mathbf{r}_\perp. \qquad (5)$$

The existence of these relations is associated with the translational symmetry of the initial equation ($z \longrightarrow z + z_0$, $\tau \longrightarrow \tau + \tau_0$). They are a generalization of the well-known expressions for the “energy” (the number of quanta) and the Hamiltonian involved in the nonlinear Schrödinger equation to the case of a broadband pulse.

For the qualitative investigation of the dynamics of three-dimensional wave packets, we use the method of moments. For the subsequent consideration, the continuity equation is the initial point:

$$\begin{aligned}\frac{\partial}{\partial z}\left(\frac{\partial\Phi}{\partial\tau}\right)^2 &= -3\frac{\partial}{\partial\tau}\left(\frac{\Phi_\tau^4}{2} + b\Phi_{\tau\tau}^2\right) - \frac{\partial}{\partial\tau}(\nabla_\perp\Phi)^2 \\ &\quad + b\frac{\partial^3}{\partial\tau^3}\Phi_\tau^2 + 2\mathrm{div}_\perp(\Phi_\tau\nabla_\perp\Phi) - a\frac{\partial\Phi^2}{\partial\tau}.\end{aligned} \qquad (6)$$

This equation is obtained by multiplying Eq. (2) by $2\Phi_\tau$ and then transforming it to the divergent form. One of the most informative relations can be obtained for the characteristic transverse size of the axially symmetric wave field:

$$\overline{\rho_\perp^2} = \frac{\int r_\perp^2\Phi_\tau^2 d\tau d\mathbf{r}_\perp}{I}.$$

Multiplying Eq. (2) by $r_\perp^2$ and performing the corresponding operations, we easily arrive at the equation

$$\frac{d^2\overline{\rho_\perp^2}}{dz^2} = \frac{8H + 8\int(b\Phi_{\tau\tau}^2 - a\Phi^2)d\tau d\mathbf{r}_\perp}{I}, \qquad (7)$$

which describes the variation of the effective transverse size of the wave field in the process of the evolution of the system. In the absence of low-frequency dispersion ($a = 0$), such an equation was obtained in [6].

First of all, it should be noted that, for a dispersion-free medium ($a = b = 0$), the right-hand side of the equation is proportional to the Hamiltonian of the system, which is given by Eq. (5) [5]. In this case, one can conclude that the wave field distributions corresponding to $H < 0$ collapse in the transverse direction. The right-hand side of Eq. (7) is also negative for the initial distributions whose spectrum lies in the region of the anomalous group velocity dispersion ($b \longrightarrow 0$). As in the case of a quasi-monochromatic pulse, we also obtain a collapse. A solution of Eq. (2) exists for finite paths z_k, and, for the regularization of the singularity arising in this case, it is necessary to take into account additional mechanisms (saturation of nonlinearity, nonlinear absorption, etc.). However, such a unique conclusion cannot be made for the distributions whose spectrum is concentrated in the region of the normal group velocity dispersion ($a \longrightarrow 0$). For these distributions, it is only possible to conclude that they are self-compressed at the initial stage of the evolution of the system. In the general case ($a \neq 0$, $b \neq 0$), wider possibilities arise for nonlinearity amplification, as compared to the case of a quasi-monochromatic wave packet, and these possibilities require closer investigation. For example, one of them is related to the choice of the central frequency of radiation when the parameter of the group velocity dispersion is equal to zero ($\partial^2 k_z/\partial\omega^2 = 0$). Another possibility can be determined from Eq. (7). One can see that, for the field distributions decreasing as $\exp(-\sqrt[4]{(a/b)}\,|\tau|)$, the integral term in Eq. (7) vanishes. Thus, for the initial distributions containing a set of regions with such field variations, Hamiltonian (5) proves to be the same as that in a dispersionless medium.

2. To illustrate the features of the self-action dynamics of ultrashort pulses, we present the results of a numerical simulation based on Eq. (1) for the processes that occur in the system.

We consider the simplest case of a dispersionless medium ($a = b = 0$). Figure 1a shows the evolution of the field on the axis of the system. One can see that the main process is the steepening of the wave field profile within each of the half-periods and the formation of shock waves. Unlike the quadratic nonlinearity, in the “cubic” medium under consideration, a trapezoidal rather than saw-tooth profile is formed. The absorption at shock fronts proves to be so strong that the wave

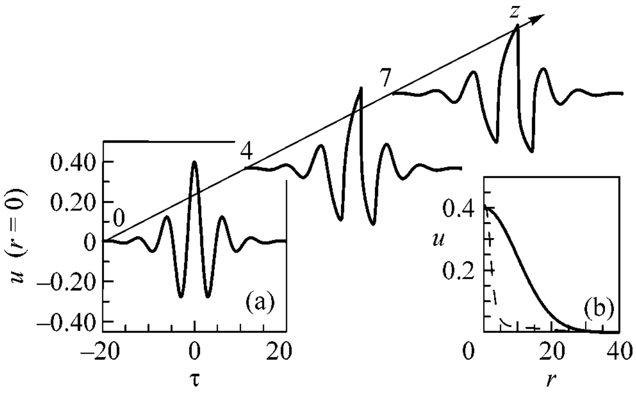

Fig. 1. Dynamics of a linearly polarized field in a dispersionless medium ($a = 0$, $b = 0$): (a) the evolution of the longitudinal structure of the wave packet ($r = 0$) and (b) the transverse distribution of the maximum-amplitude field (the solid line represents the initial distribution, and the dashed line corresponds to $z = 4$); $u = 0.4\frac{\cos(\tau)}{\cosh(0.3\tau)}\exp\left(-\frac{r^2}{200}\right)$.

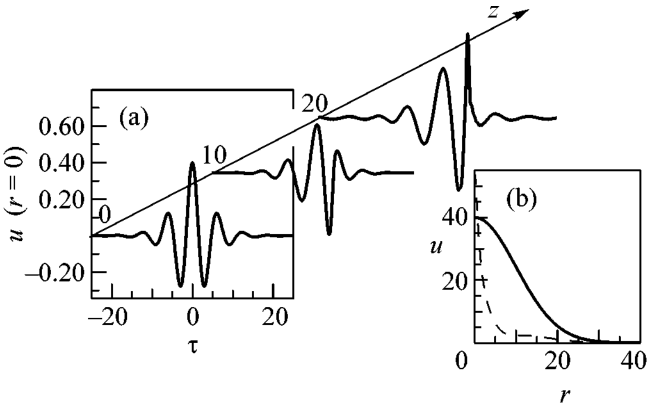

Fig. 2. Dynamics of a circularly polarized field in a dispersionless medium ($a = 0$, $b = 0$): (a) the evolution of the longitudinal structure ($r = 0$) and (b) the transverse distribution of the maximum-amplitude field (the solid line represents the initial distribution, and the dashed line corresponds to $z = 20$); $u = \frac{0.4}{\cosh(0.3\tau)}\exp\left(-\frac{r^2}{200}\right)[\cos(\tau) + i\sin(\tau)]$.

amplitude remains almost unchanged. At the same time, the width of the wave field decreases noticeably (Fig. 1b). To interpret these results, we use the fact that, in the dispersion-free medium under study, the pulse duration remains constant. This means that the processes occur locally, as in a quasi-monochromatic wave beam. In the nonlinear term, we can distinguish two parts. One of them corresponds to the cubic nonlinearity, which, in the conservative regime, leads to a self-compression of the wave packet according to the same law (7) as in the theory of self-focusing. The other determines the linear absorption associated with the wavebreaking of the profile and the formation of multiple shock fronts. Evidently, for wave beams with a characteristic transverse dimension much greater than the wavelength, the self-focusing process proves to be sufficiently slow compared to the rate of the shock wave formation at every half-period of the field [5]. The value of the nonlinear absorption in the case under study can be determined by analogy with the case of one-dimensional weak shock waves in hydrodynamics [5, 8]. Considering the additive effect of these nonlinearities, we arrive at the nonlinear Schrödinger equation in the form

$$i\frac{\partial\psi}{\partial z} + \Delta_\perp\psi + |\psi|^2\psi + i\nu|\psi|^2\psi = 0$$

with an additional term describing the nonlinear dissipation of radiation. The numerical solution of this equation, as well as the calculations of the corresponding equation in the so-called aberration-free approximation [5], leads to a noticeable transverse self-compression of the wave field under conditions of a virtually constant field amplitude at the axis of the system. Thus, the absorption of ultrashort pulses of linearly polarized radiation at internal shock waves fundamentally changes the character of the wave packet collapse: it occurs without any field amplification.

3. The formation of multiple shock fronts hinders the numerical simulation of the long-term evolution of the system. The problem is simplified in the case of circularly polarized waves $\mathbf{u} = u(\mathbf{x}_0 + i\mathbf{y}_0)$ ($\mathbf{x}_0$ and $\mathbf{y}_0$ are unit vectors along the respective axes). Generalization (1) for the wave field with a circular polarization leads to the equation

$$\frac{\partial}{\partial\tau}\left(\frac{\partial u}{\partial z} + \frac{\partial}{\partial\tau}|u|^2u - \gamma\frac{\partial^2 u}{\partial\tau^2} + \beta|u|^6u - b\frac{\partial^3 u}{\partial\tau^3}\right) = \Delta_\perp u - au. \quad (8)$$

This equation can be derived on the basis of the one-dimensional equation given in [9], which describes the self-action dynamics of a vector field in a medium with a cubic nonlinearity. For a broad wave beam, adding the term $\Delta_\perp u$, we arrive at Eq. (8). Equation (8) additionally contains a nonlinear dissipation ($\beta \neq 0$) for stabilizing the collapse. In a quasi-monochromatic field, it describes the multiphoton absorption.

Figure 2 shows the results of numerical simulation for the self-action dynamics of a circularly polarized wave field in a dispersion-free medium with the same parameters as those in Fig. 1. In this case, as one can see, no steepening of the profile occurs for the half-periods of the field and, hence, the possibility of the field dissipation at the shock fronts is absent. As a result, from Eq. (7) transformed to the case of a circularly polarized wave ($\gamma = 0$, $\beta = 0$), we find that not only does the effective width of the wave field decrease (to zero) but also the amplitude of the field increases without bound, as in the case of an ordinary collapse.

The numerical study of the self-action dynamics under initial conditions virtually identical to those used

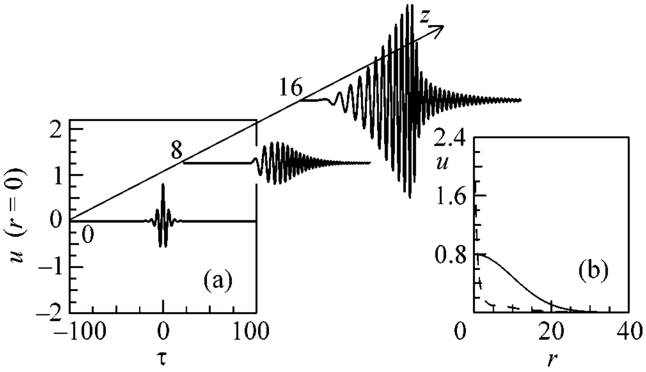

Fig. 3. Dynamics of a circularly polarized field in a medium with normal dispersion: (a) the evolution of the wave field on the axis of the system ($r = 0$) and (b) the transverse distribution of the maximum-amplitude field (the solid line represents the initial distribution, and the dashed line corresponds to $z = 16$); $a = 0$ and $b = 1$; $u = \frac{0.8}{\cosh(0.3\tau)}\exp\left(-\frac{r^2}{200}\right)[\cos(\tau) + i\sin(\tau)]$.

for linearly polarized waves confirms the above conclusion (see Fig. 2). To stabilize the singularity, we took into account the nonlinear absorption by introducing an additional term in the equation. A new result obtained in this case is the steepening of the envelope profile. This steepening is associated with the dependence of the group velocity on the wave packet amplitude. A characteristic feature is the separation of an extremely short pulse near the leading edge of the packet, the duration of this pulse being much smaller than the wavelength corresponding to the central frequency. This effect is also present in the one-dimensional problem ($\Delta_\perp = 0$). In the three-dimensional case under study, the length of the formation of such a structure is much smaller. The self-focusing of the wave field additionally leads to a considerable increase in the wave amplitude, so that the steepening of the envelope profile and the shock front formation manifest themselves for initial amplitudes much smaller than those in the one-dimensional case.

In a medium with a predominant anomalous group velocity dispersion ($b \longrightarrow 0$), the self-action dynamics of a circularly polarized wave field with parameters corresponding to the collapse realization ($H < 0$) is similar to the dynamics observed in the quasi-monochromatic case. Since the dispersion spreading of ultrashort (and extremely short) pulses proves to be noticeable, the self-compression in the transverse direction occurs with a simultaneous monotonic increase in the longitudinal dimension.

The distinctive features of the self-action dynamics are more pronounced in a medium with the predominance of the normal group velocity dispersion ($a \longrightarrow 0$). In the case of the chosen initial distribution (Fig. 3), a noticeable self-compression of the wave field occurs along the transverse axis. In the calculations, this effect was stabilized by taking into account the nonlinear (multiphoton) absorption.

One can see that here the distribution does not break in two, as in the case of a quasi-monochromatic wave packet. It is the development of the breaking instability that is believed to cause the limitation of the maximum amplitude and the stabilization of the collapse [10]. The nonlinear dispersion leads to the violation of the symmetry of the self-compression process. As a result, with an increase in the maximum amplitude, a characteristic steepening of the trailing edge of the pulse and the formation of the envelope shock wave take place. A similar situation occurs in the framework of the nonlinear Schrödinger equation with allowance for the dependence of the group velocity of the wave packet on amplitude [11]. Thus, the dispersion spreading of the packet does not prevent its transverse self-compression (collapse), which proceeds simultaneously with the formation of a sharp shock front in the longitudinal envelope.

In this paper, we briefly considered the characteristic features of the space–time evolution of electromagnetic radiation whose spectral width is on the order of the carrier frequency. On the basis of the equation for the effective width of the wave field, it is possible to separate the class of initial distributions that later undergo collapse. The numerical study has shown that this process is not as universal as in the case of quasi-monochromatic radiation. Only in a medium with a predominance of the anomalous group velocity dispersion does the situation prove to be analogous to that observed in the case of a cubic nonlinearity. In other cases, the situation is much more complicated. For example, in the case of linearly polarized radiation in a dispersion-free medium, an important role in the self-action dynamics is played by the nonlinear attenuation at shock fronts caused by the steepening of the wave profile within each of the half-periods of the field. As a result, the focusing of the wave field in the transverse direction is compensated by the absorption and occurs without any noticeable increase in amplitude.

For circularly polarized wave fields, the nonlinearity under consideration leads to both an increase in the field amplitude and the formation of an envelope shock wave; i.e., a collapse and a gradient catastrophe simultaneously take place.

We are grateful to A.A. Balakin and D.I. Kulagin for assistance in constructing the numerical code and to D.V. Kartashov for the interest in our work and for discussions. This work was supported by the Russian Foundation for Basic Research, project nos. 04-02-16420, 05-02-17517, and 05-02-17509. One of us (S.S.) is also grateful to the Foundation in Support of Domestic Science and to the Dynasty Foundation.

REFERENCES

1. P. M. Paul, E. S. Toma, P. Breger, *et al.*, Science **292**, 1689 (2001); A. Baltuska, Th. Udem, M. Uiberacher, *et al.*, Nature **421**, 611 (2003).
2. Qin Chen and X. C. Zhang, in *Ultrafast Lasers: Technology and Applications*, Ed. by M. E. Femann, A. Golvanauskas, and G. Sucha (Marcel Dekker, New York, 2003); R. A. Cheville and D. Grischkowsky, Appl. Phys. Lett. **67**, 1960 (1995).
3. A. Braun, G. Korn, X. Liu, *et al.*, Opt. Lett. **20**, 73 (1995); E. T. J. Nibbering, P. F. Curley, G. Grillion, *et al.*, Opt. Lett. **21**, 62 (1996).
4. É. M. Belenov and A. V. Nazarkin, Pis'ma Zh. Éksp. Teor. Fiz. **53**, 188 (1991) [JETP Lett. **53**, 200 (1991)]; S. A. Kozlov and S. V. Sazonov, Zh. Éksp. Teor. Fiz. **111**, 404 (1997) [JETP **84**, 221 (1997)].
5. O. V. Rudenko and O. A. Sapozhnikov, Usp. Fiz. Nauk **174**, 970 (2004) [Phys. Usp. **47**, 907 (2004)]; Zh. Éksp. Teor. Fiz. **106**, 395 (1994) [JETP **79**, 220 (1994)].
6. S. K. Turitsyn and G. E. Fal'kovich, Zh. Éksp. Teor. Fiz. **89**, 258 (1985) [Sov. Phys. JETP **62**, 146 (1985)]; V. S. L'vov, *Nonlinear Spin Waves* (Nauka, Moscow, 1987) [in Russian].
7. L. D. Landau and E. M. Lifshitz, *Course of Theoretical Physics*, Vol. 8: *Electrodynamics of Continuous Media*, 2nd ed. (Nauka, Moscow, 1982; Pergamon, Oxford, 1984).
8. L. D. Landau and E. M. Lifshitz, *Course of Theoretical Physics*, Vol. 6: *Fluid Mechanics*, 3rd ed. (Nauka, Moscow, 1986; Pergamon, New York, 1987).
9. D. V. Kartashov, A. V. Kim, and S. A. Skobelev, Pis'ma Zh. Éksp. Teor. Fiz. **78**, 722 (2003) [JETP Lett. **78**, 276 (2003)].
10. N. A. Zharova, A. G. Litvak, T. A. Petrova, *et al.*, Izv. Vyssh. Uchebn. Zaved., Radiofiz. **29**, 1137 (1986); L. Berge, Phys. Rep. **303**, 259 (1998).
11. N. A. Zharova, A. G. Litvak, and V. A. Mironov, Izv. Vyssh. Uchebn. Zaved., Radiofiz. **46**, 331 (2003).

Translated by E. Golyamina

JETP Letters, Vol. 82, No. 3, 2005, pp. 110–114. Translated from Pis'ma v Zhurnal Éksperimental'noĭ i Teoreticheskoĭ Fiziki, Vol. 82, No. 3, 2005, pp. 124–128.
Original Russian Text Copyright © 2005 by Zibrov, Novikova.

Observation of Quantum Noise in the Polarization of Laser Light in a Rubidium-Vapor Cell

A. S. Zibrov[a, b] and I. Novikova[a]

[a] *Harvard–Smithsonian Center for Astrophysics and Physics Department, Harvard University, Cambridge, Massachusetts 02138, USA*
e-mail: inovikova@cfa.harvard.edu
[b] *Lebedev Physical Institute, Russian Academy of Sciences, Leninskiĭ pr. 53, Moscow, 117924 Russia*

Received June 28, 2005

Experimental observation of quantum noise in the polarization of laser light that has passed through a dense Rb^{87} atomic vapor is reported. The step-like noise spectrum is observed. Factors responsible for the form of the observed spectrum and the absence of noise "squeezing" predicted by Matsko *et al.* [Phys. Rev. A **63**, 043814 (2001)] are discussed. © *2005 Pleiades Publishing, Inc.*

PACS numbers: 42.50.Gy, 42.65.–k

Quantum fluctuations of the electromagnetic field determine the fundamental limit of the measurement accuracy in many experiments. In view of this circumstance, of great interest is the development of various methods for generating light with nonclassical statistics that provide the reduction of quantum noise [1, 2]. When light propagates through a nonlinear medium, its statistics changes, which is determined by the strength of the nonlinear interaction and linear losses in the medium [2, 3]. For this reason, proposals of using a dense atomic vapor with induced quantum coherence to control the light statistics seem to be particularly promising.

Coherence created by means of a strong controlling field between levels of the ground states of alkali metals makes an optically dense medium transparent, which exhibits strong dispersion in this case. This effect is called electromagnetically induced transparency (EIT) [1]. The third-order susceptibility of the medium with EIT is high and nearly equal to the linear susceptibility, which leads to the effective coupling between fields involved in nonlinear processes [4].

The authors of [5] demonstrated that the quantum state of light in the presence of EIT can be projected on a collective atomic state, which provides long-term storage of information about light and its further recovery on demand. In [6], it was theoretically shown that EIT created due to coherence induced in Zeeman sublevels of the same ground state of rubidium vapor can be used to squeeze the quantum noise in the laser polarization. Those calculations showed that a squeezing of 8 dB can be reached.

The aim of this work is to analyze the possibility of polarization quantum noise squeezing using the D_1 line of rubidium. Connection between the applied field intensity and the frequency bandwidth of quantum noise deformation is investigated in this work.

The mechanism proposed in [6] for squeezing light polarization is as follows. The linear polarization of light propagating in the rubidium vapor is represented as the superposition of oppositely rotating polarizations σ^+ and σ^- (see Fig. 1a). These fields ensure the conditions for appearance of EIT, forming the λ configuration of the interaction of the fields with the Zeeman sublevels $|m_F = -1\rangle$ and $|m_F = +1\rangle$. For an idealized λ scheme, EIT does not lead to change in the phase delay between σ^+ and σ^- components. However, the real structure of the excited state of rubidium, including the existence of other hyperfine components, Doppler broadening, and losses, introduces phase delays between the polarization components of the field. Indeed, in the dressed-field states [7], the absorption spectrum of the field σ^- has two resonances $|+\rangle$ and $|-\rangle$ with the corresponding distribution of the refractive index $n(\nu)$. Let us assume that a spontaneous photon is emitted due to vacuum fluctuations at frequency $(\nu_0 + (\kappa v))$ (see Fig. 1b). An increase in the intensity induced by this photon leads to a change in the distance $2\Omega'$ between the states $|+\rangle$ and $|-\rangle$ and, therefore, to a change in the transmission of the σ^- component. The refractive index at the laser frequency changes simultaneously by Δn. Thus, correlation arises between changes in the number of photons and field phase.

Therefore, two polarization components are coupled due to the ac Stark effect. As a result, a decrease in the shot noise in the σ^- component is observed in one of the field quadratures, whereas it increases in the other quadrature.

The results of [6] are experimentally confirmed in [8], where the detection of squeezing of the quantum noise in linearly polarized laser light after passage through a cell with the D_2 rubidium vapor is reported. In the experiment, a decrease in quantum noise by 0.85 dB below the shot noise level was observed. The D_1 line of rubidium seems more promising for studying the possibility of squeezing light, because it has (i) a simpler structure of excited states that are all involved in the creation of coherence, (ii) larger EIT, and (iii) a larger effect of the nonlinear polarization rotation [9].

The experimental setup layout is shown in Fig. 1. Linearly polarized light propagates through a cylindrical Pyrex cell containing isotopically pure ^{87}Rb. The length and diameter of the cell are equal to 2.5 cm. The frequency of the external-cavity diode laser is tuned near the $F = 2 \longrightarrow F' = 1, 2$ Rb transition (wavelength of 795 nm). The power of light at the input of the cell was in the range $P = 1$–8 mW and the diameter of the beam was equal to $D = 2$ mm. Laser diodes have a large two-dimensional asymmetry of the spatial distribution of radiation. For this reason, the beam was spatially filtered by means of a telescope at whose waist a circular aperture 30 μm in diameter was placed. Such a system transmitted ~70% of incident light with an intensity distribution close to a Gaussian. Noise in the work was detected using the traditional phase-sensitive homodyne technique [10]. A two-arm interferometer included a crystal polarizer (with an extinction coefficient of 5×10^{-6}), mirrors, and a 50 : 50 nonpolarizing beamsplitter. Light $E_{\|}$ passed through the polarizer was used as the local oscillator.

In the local-oscillator channel $E_{\|}$, a half-wave plate was used, which ensured the adjustment of the same polarizations in both channels of the interferometer. After careful adjustment of the interferometer, the visibility of its fringes approached 96–98%. The high quality of fridges indicates a single-mode laser field.

Light at the outputs of the homodyne detection scheme was collected at two identical S3883 Hamamatsu silicon *p–i–n* photodiodes with a quantum efficiency of 91%. The photocurrents of these diodes after amplification by OPA657 low-noise amplifiers were subtracted by a ZFSCJ-2-2 MiniCircuits 180° combiner with the operating range from 0.01 to 20.0 MHz. The gains of the amplifiers were carefully balanced. To this end, the laser current was modulated at a frequency of about 5 MHz, which led to the appearance of a spectral component at this frequency. The amplification was balanced such that the modulation component disappeared completely after the subtraction of photocurrents. Thus, the correlated components of photocurrents were subtracted better than 35 dB.

Before measurement of the quantum noise level, the detection system was calibrated in the traditional way: the channel $E_{\perp}$ was closed and the noise level of the difference between photocurrents was then measured as a function of the incident light intensity. This dependence was linear over the entire power range under investigation. The homodyne detection noise spectrum for the closed channel $E_{\perp}$ is indicated as SQL in Fig. 2. The shutdown of light in front of one of the photodiodes reduced noise by a factor of 1.4.

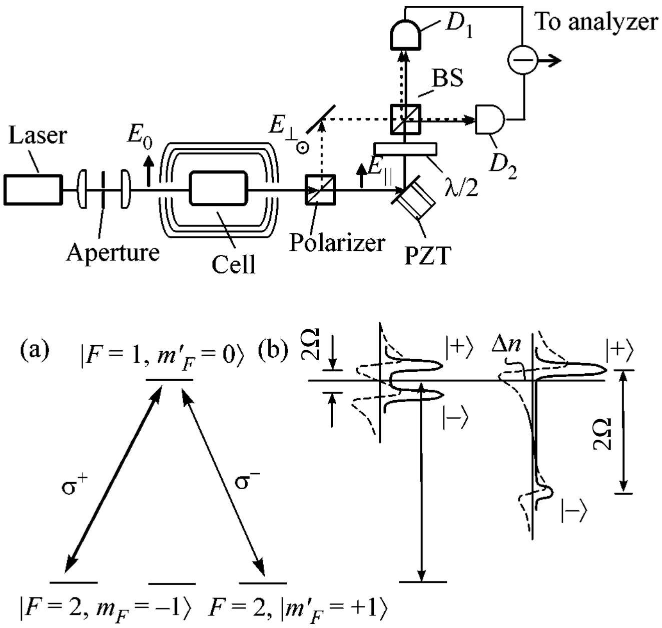

Fig. 1. Layout of the experimental setup. The local-oscillator channel is denoted as $E_{\|}$. Radiation with the orthogonal polarization propagates in the other interferometer arm $E_{\perp}$. A mirror placed on a piezodrive makes it possible to change the relative phase of the fields in the interferometer arms. To detect interference between two fields, their polarizations are tuned by means of a half-wave plate. (a) The λ scheme on Zeeman sublevels. The linear polarization of light E_0 is represented as the sum of the oppositely-rotating polarizations σ^+ and σ^-. (b) The λ scheme in the dressed-state representation. The left part is for atoms at rest, the right part is for an atom moving with velocity κv, Ω is the Rabi frequency, $\Omega' = \sqrt{\Omega^2 + (\kappa v)^2}$, and $n(\nu)$ is the refractive index.

The cell was in a three-layer magnetic screen and was heated to a temperature of about 85–95°C, which corresponds to the atomic-vapor density $N = 5 \times 10^{11}$–2×10^{12} cm^{-3}.

Noise was analyzed near the transitions $F = 2 \longrightarrow F' = 1, 2$ (the distance between them is equal to 812 MHz). Amplification of quantum noise was observed for both high-frequency and low-frequency detuning from a transition. For a detuning of about (+150 ± 60) MHz, the noise spectrum has the pronounced shape of a step with a peak (see Fig. 3). The position of the step is a linear function of the intensity and is shifted towards higher frequencies as the intensity increases (Fig. 3). When the length of the interferometer arms changed such that the field phase difference between different arms of the interferometer was equal to 180°, the observed features disappeared (see

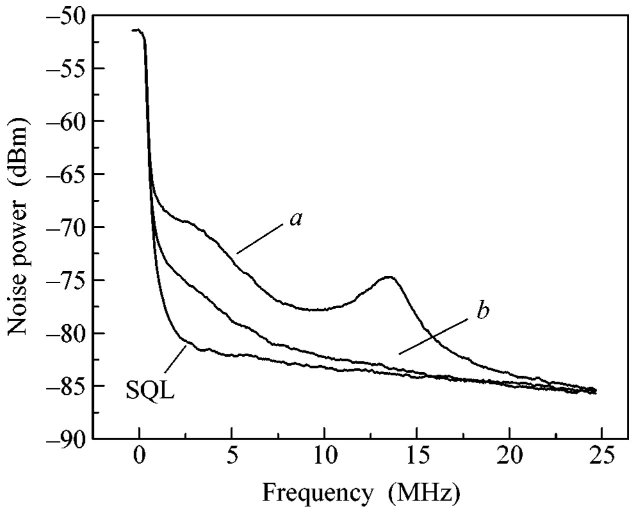

Fig. 2. Noise spectrum detected by a homodyne detector when the field phases in both arms (*a*) coincide with each other and (*b*) differ from each other by 180°. The cell temperature was equal to 95°, the laser power was 7.4 mW, the laser frequency was detuned from the transition $F = 2 \longrightarrow F' = 1$ towards higher frequencies by 150 MHz, and the beam diameter was equal to 1 mm. The noise spectrum when the $E_{\perp}$ arm is closed is denoted as SQL. The analyzer resolution was equal to 100 kHz and the video detector band was 30 Hz.

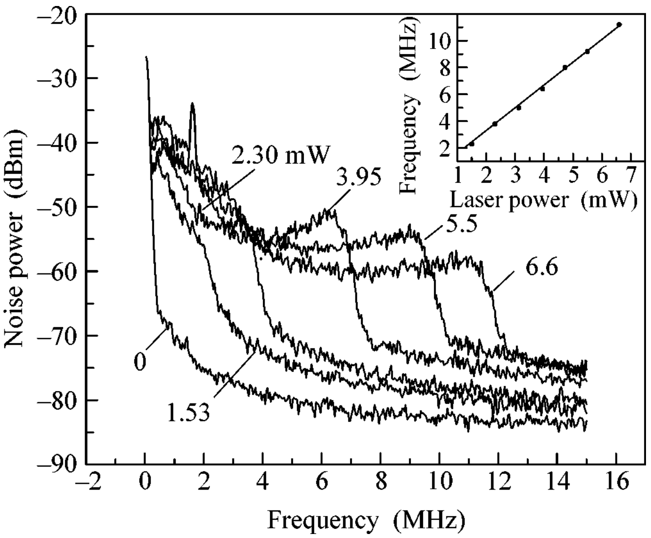

Fig. 3. Noise spectrum detected by a homodyne detector for various incident-light powers when the field phases in both arms coincide with each other. The cell temperature was equal to 95°, the laser frequency was detuned from the transition $F = 2 \longrightarrow F' = 1$ towards higher frequencies by 150 MHz, and the beam diameter was equal to 2 mm. The analyzer resolution was equal to 100 kHz and the video detector band was 1 kHz. The inset shows the position of the noise "step" peak vs. the laser power.

Fig. 2, line *b*). In this case, noise decreased by 10–20 dB. Blocking light in the $E_{\perp}$ channel reduces the detected noise to the SQL level.

The squeezing of quantum noise was not observed in the experiment. We detected a decrease in noise, but this decrease was not below the SQL noise level (see Fig. 2, line *b*). It is interesting that the noise level is minimal near the high-frequency spectrum peak whose frequency is approximately equal to the Rabi frequency (~12 MHz in Fig. 2, line *a*). The squeezing of light was observed in [8] near a frequency of about 5 MHz, whereas the Rabi frequency was equal to about 100 MHz.

DISCUSSION

First, we point to a considerable difference between the conditions of our experiment and conditions found in [6, 8]. In those works, the squeezing of light was estimated under the assumption of a high intensity of light whose Rabi frequency almost reaches the hyperfine splitting of the ground state (~6.8 GHz). For these parameters, the effect of atomic interference on the formation of the squeezing spectrum is insignificant [11]. The effect of the Doppler broadening (~0.5 GHz) on the EIT spectrum is negligible, and the four-level system of the D_1 rubidium line is virtually transformed to the two-level system where birefringence is due to an ac Stark effect. Since the frequency dependence of absorption changes faster than dispersion varies in the medium, the authors of [6] found the parameters of the system for which the quadrature squeezing of the σ^- component arises. In our experiment, atomic coherence is decisive for the creation of birefringence [12, 13]. Therefore, the EIT spectrum forms the noise spectrum. Obviously, the correlation between intensity and phase fluctuations is necessarily most pronounced at the sharp boundary of the transmission window, which is observed in a dense medium in the presence of EIT. In such a medium, all noise frequencies outside of the transparency window Γ are absorbed [5, 14, 15]. The width of the induced-transparency resonance in a dense medium is linearly related to the applied-field intensity [15]:

$$\Gamma = \frac{\Omega^2}{\sqrt{\gamma_{bc}\gamma_a}}\frac{1}{\sqrt{\eta\kappa L}}. \qquad (1)$$

Here, Ω is the Rabi frequency; γ_a is the excited-state decay rate; γ_{bc} is the coherence-relaxation rate; $\eta = 3N\lambda^3/4\pi^2$, where N is the atomic density; and $\kappa = 2\pi/\lambda$.

Let us estimate Γ using the parameters of the experiment. The parameter γ_{bc} in the experiment is determined by the time of flight of an atom moving with the thermal velocity through the laser beam and is equal to about 10^5 Hz. The relaxation time of the polarization of the excited rubidium-atom state is equal to about 5 MHz. Using the formula $\Omega = \gamma_a\sqrt{I/8}$, where I is the intensity of the controlling field (in mW/cm^2) [17], we estimate the Rabi frequency as $\Omega \simeq 25$ MHz and, hence, $\Gamma \sim 20$ MHz. It is difficult to expect a better coincidence of Γ with the frequency of the noise peak in the presence of spatial inhomogeneity, optical pumping, etc. (see, e.g., [18]).

Under conditions similar to our experiment, an efficient Raman spontaneous process occurs in the atomic vapor. As a result, new fields S and N are excited (see Fig. 4). The intensity of these fields may reach 2–5% of the incident-radiation intensity. The frequencies of the new fields differ by 6.8 GHz (the frequency of the splitting of the atomic ground state) from the applied-field frequency. In the homodyne experimental technique, noise in the new field is not detected. However, the scattering of part of the incident-field energy into the new fields disturbs the correlations between fluctuations of the number of photons and field phase.

In addition, the squeezing of light was not observed, possibly due to the considerable radiation trapping in a dense medium [9]. In a dense medium, the probability of reabsorption of spontaneous radiation is large. Since the spontaneous radiation is dephased and depolarized, it destroys the induced atomic coherence. The radiation trapping begins to affect atomic coherence effects when the vapor pressure exceeds 10^{10} cm^{-3}. According to [9], the rate of incoherent excitation of atoms from the ground state to excited states increases rapidly with density and, at 0.5×10^{12} cm^{-3}, it becomes equal to the relaxation rate of the ground states. As a result, transparency induced by atomic coherence decreases noticeably, and this increase in losses complicates the detection of light squeezing. We emphasize that in [8], where the D_2 line to which the cyclic transition $5S_{1/2}F = 2 \longrightarrow 5P_{3/2}F' = 3$ contributes is studied, the radiation trapping effect is much stronger, but the squeezing of light is observed. This fact indirectly indicates a small role of atomic coherence in the squeezing mechanism. We also note that the radiation trapping effect was disregarded in the calculations reported in [6].

We point to an additional source of noise that is always mentioned in works where semiconductor lasers are used, particularly in regard to atomic clocks and magnetometers. It is the so-called noise of the conversion of phase noise to the intensity of radiation passed through the cell (PM-to-AM conversion) [19]. Owing to the relatively low quality factor of the diode laser cavity, it has a wide phase-noise spectrum, which is transferred into transmitted intensity fluctuations after traversing a resonant absorbing medium. In this experiment, we used a diode laser with an external cavity with a very low level of AM and PM noise. For this reason, we believe that the PM-to-AM conversion cannot be responsible for the increase in the noise level observed in this experiment.

In conclusion, we summarize that the quantum noise in the polarization of laser light passing through a cell filled with atomic rubidium vapor has been studied in this work. In the dependence on the phase of the homodyne detector, an increase in quantum noise by two orders of magnitude is observed. The noise spectrum has a step-like shape. The above results are important for creating quantum magnetometers [20] and microwave frequency standards [21] based on EIT whose limiting accuracy is estimated disregarding observed noise.

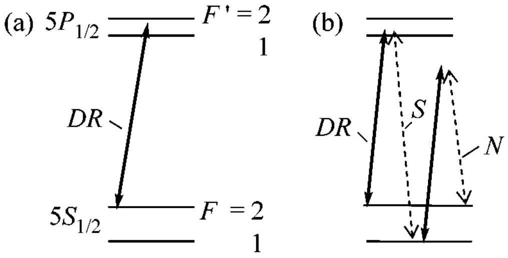

Fig. 4. (a) Scheme of the levels contributing to the D_1 Rb line, where the applied field frequency DR is also shown, and (b) Raman spontaneous scattering that initiates the generation of two new fields S and N. For details, see [16].

We are grateful to A.B. Matsko for assistance and interest in the work.

REFERENCES

1. M. O. Scully and M. S. Zubairy, *Quantum Optics* (Cambridge Univ. Press, Cambridge, UK, 1997).
2. H.-A. Bachor and T. C. Ralph, *A Guide to Experiments in Quantum Optics* (Wiley–VCH, Berlin, 2004).
3. R. E. Slusher, B. Yurke, P. Grangier, *et al.*, J. Opt. Soc. Am. B **4**, 1453 (1987); *Quantum Noise Reduction in Optical Systems*, Ed. by C. Fabre and E. Giacobino; Appl. Phys. B **55**, 189 (1992).
4. S. E. Harris, Phys. Today **50**, 36 (1997); M. D. Lukin and A. Imamoglu, Nature **413**, 273 (2001).
5. L. M. Duan, M. D. Lukin, J. I. Cirac, and P. Zoller, Nature **414**, 413 (2001); C. H. van der Wal, M. D. Eisaman, A. André, *et al.*, Science **301**, 196 (2003).
6. A. B. Matsko, I. B. Novikova, G. R. Welch, *et al.*, Phys. Rev. A **63**, 043814 (2001).
7. C. Cohen-Tannoudji, J. Dupont-Roc, and G. Grynberg, *Atom–Photon Interactions* (Wiley, New York, 1992).
8. J. Ries, B. Brezer, and A. I. Lvovsky, Phys. Rev. A **68**, 025801 (2003).
9. A. B. Matsko, I. Novikova, M. O. Scully, and G. R. Welch, Phys. Rev. Lett. **87**, 133 601 (2001).
10. L. Mandel and E. Wolf, *Optical Coherence and Quantum Optics* (Cambridge Univ. Press, Cambridge, 1995; Nauka, Moscow, 2000).
11. A. B. Matsko agreed with this opinion when discussing the problem through e-mail.
12. I. Novikova, A. B. Matsko, and G. R. Welch, J. Mod. Opt. **49**, 2565 (2002).
13. I. Novikova, A. B. Matsko, V. A. Sautenkov, *et al.*, Opt. Lett. **25**, 1651 (2000).
14. E. E. Mikhailov, V. A. Sautenkov, Y. V. Rostovtsev, *et al.*, quant-ph/0503085.

15. M. D. Lukin, M. Fleischhauer, A. S. Zibrov, *et al.*, Phys. Rev. Lett. **79**, 2959 (1997).
16. A. S. Zibrov, M. D. Lukin, and M. O. Scully, Phys. Rev. Lett. **83**, 4049 (1999).
17. T. T. Grove, V. Sanchez-Vilicana, B. C. Duncan, *et al.*, Phys. Scr. **52**, 271 (1995).
18. C. Y. Ye and A. S. Zibrov, Phys. Rev. A **65**, 023806 (2002).
19. J. C. Camparo and J. G. Coffer, Phys. Rev. A **59**, 728 (1999); J. Camparo, Phys. Rev. A **69**, 013802 (2004); S. Knappe, R. Wynands, J. Kitching, *et al.*, J. Opt. Soc. Am. B **18**, 1545 (2001).
20. C. Affolderbach, M. Stähler, S. Knappe, and R. Wynands, Appl. Phys. B **75**, 605 (2002); M. Fleischhauer, A. B. Matsko, and M. O. Scully, Phys. Rev. A **62**, 013808 (2000); A. B. Matsko, M. Fleischhauer, and M. O. Scully, Phys. Rev. Lett. **86**, 2006 (2001).
21. S. Zibrov, I. Novikova, D. F. Phillips, *et al.*, physics/0501090; Phys. Rev. A **72**, 011801(R) (2005); J. Vanier, M. W. Levine, D. Janssen, and M. J. Delaney, IEEE Trans. Instrum. Meas. **52**, 822 (2003).

Translated by R. Tyapaev

JETP Letters, Vol. 82, No. 3, 2005, pp. 115–119. Translated from Pis'ma v Zhurnal Éksperimental'noĭ i Teoreticheskoĭ Fiziki, Vol. 82, No. 3, 2005, pp. 129–133.
Original Russian Text Copyright © 2005 by Vasil'ev.

Experimental Observation of the Nonequilibrium Condensation of Electron–Hole Pairs in GaAs at Room Temperature

P. P. Vasil'ev
Lebedev Physical Institute, Russian Academy of Sciences, Leninskiĭ pr. 53, Moscow, 119991 Russia
e-mail: peter@mail1.lebedev.ru

Received April 24, 2005; in final form, June 6, 2005

The effect of the nonstationary condensation of electron–hole pairs in GaAs/AlGaAs *p–i–n* heterostructures at room temperature under the conditions of generation of superradiance pulses was demonstrated in an explicit form. It was found that a dramatic decrease in spontaneous emission from the entire conduction band and a rapid electron transition to the very bottom of the band occurred at the earliest stages of the development of a superradiance pulse. The condensation of electrons at the band bottom resulted in the formation of a nonequilibrium coherent cooperative state, the recombination of which was observed previously as high-power femtosecond superradiance pulses. *© 2005 Pleiades Publishing, Inc.*

PACS numbers: 42.50.Fx, 71.35.Lk

The Bose condensation of excitons in semiconductors is one of the most interesting areas in the modern physics of condensed states. It is well known [1, 2] that electrons and holes, being fermions, in semiconductors can form bound states whose properties are characterized by Bose–Einstein statistics. The Bose condensation of excitons was observed at low temperatures (<10 K) in semiconductors, for example, Cu_2O and quantum-well GaAs/AlGaAs structures [3–5]. Under high-density conditions, an ensemble of collectively paired electrons and holes (composite bosons) is similar to the system of Cooper pairs in a superconductor and it is often referred to as an electron–hole BCS-like state [2].

As noted previously [6], the order parameter of an excitonic condensate is identical to its optical polarization. Consequently, it can be evaluated in the course of comparatively simple optical measurements. Moreover, it was theoretically demonstrated that the kinetics of dephasing and coherence losses of a condensate depends on its density and differs essentially from the dephasing of electron–hole pairs divorced from each other. In particular, the phase relaxation time of a condensate increased proportionally to the square of its density [6]. By this is meant that, although the number of collisions increased with density, coherence was not destroyed on collisions.

Previously [7–10], the regime of cooperative recombination was experimentally studied in a highly nonequilibrium system of electrons and holes with a high density ($>3 \times 10^{18}$ cm^{-3}) in bulk GaAs/AlGaAs *p–i–n* heterostructures at room temperature. It was found that all of the properties of emission as high-power femtosecond optical pulses can be explained by the collective pairing and condensation of electrons and holes with the formation of a short-lived coherent electron–hole BCS-like state. The average lifetime of this BCS-like state was found to be equal to about 300 fs.

Indirect evidence for the possible condensation is considered below. First, the record high radiation power emitted from a narrow spectral range at an ultrashort duration cannot be explained by the standard Fermi distribution of electrons and holes in bands with the square-root dependence of the density of states [10]. Second, an approximation of the shape of a generation spectral line allowed us to find the energy distribution of particles in a coherent cooperative state and to evaluate the parameter Δ (about 2 meV) and the Fermi energy [7]. The Fermi energies (5–7 meV) were found to be lower than the Fermi energy of electrons in GaAs at the given densities by more than one order of magnitude. Third, the coherence of the interaction of an optical field with a semiconducting medium [11] suggests the occurrence of a macroscopically great number of spatially distributed electron–hole pairs in a bound state with a common phase. Finally, anomalously large fluctuations in both amplitude and time also indirectly evidenced the establishment of an ordered state in the system of electron–hole pairs [12].

The facts of condensation at room temperature, the stability of a condensate, and the occurrence of coherence in the *e–h* ensemble at times longer than the time of intraband phase relaxation by more than one order of magnitude were the most difficult to understand and explain. Previously [10], a possible explanation of these facts was proposed. It was found that the two main prerequisites to the *e–h* condensation at room temperature are the following: (1) the presence of a resonance optical field with the quantum energy corresponding to an interband transition from the very bot-

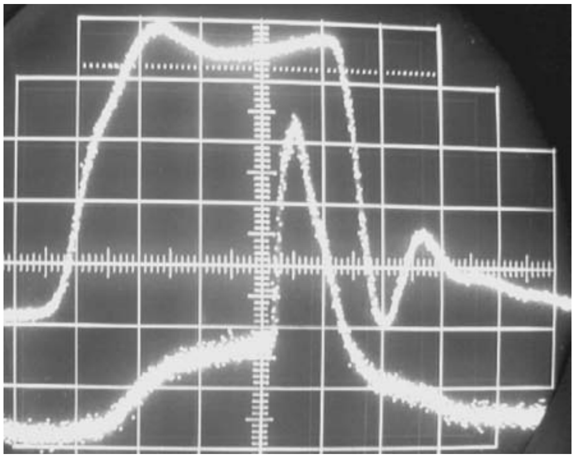

Fig. 1. Oscillograms of (upper line) current pulses and cooperative emission. Horizontal scale: 1 ns per point. Vertical scale: 150 mA per point (only for current pulses).

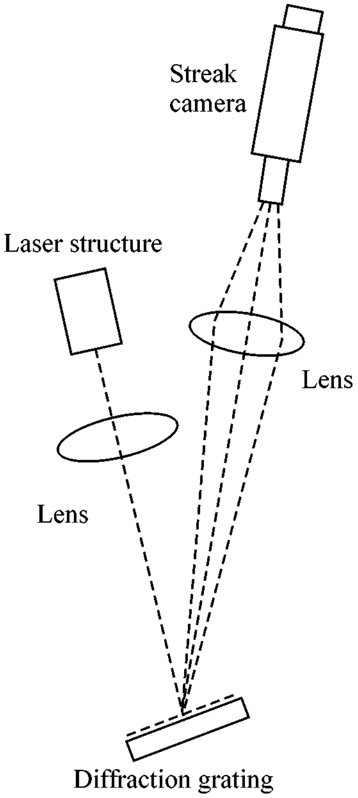

Fig. 2. Schematic diagram of the experiment.

tom of bands and (2) a high concentration of *e–h* pairs. Because of the Pauli principle, this high concentration of *e–h* pairs leads to the occupation of practically all of the energy levels in a broad band above the bottom of one of the bands (for example, the conduction band). The paradox is that a very high density of *e–h* pairs is required for the stability of a condensate and for the suppression of ultrafast relaxation.

In this work, the fact of the nonstationary condensation of electrons to the bottom of the conduction band is supported in an explicit form. All the measurements were performed at room temperature. The three-section semiconductor *p–i–n* heterostructures based on bulk GaAs, which were described previously [7–10], were used. A special feature of these structures is the presence of light-amplifying and light-absorbing regions and a low-Q resonator formed by crystal faces. Nanosecond current pulses with an amplitude of 500–800 mA were supplied to the amplifying section of a heterostructure.

Figure 1 shows a typical pulse of pumping current. A dc bias with a constant amplitude was applied to the absorption section. Either a total amplification or absorption in the structure could be readily obtained by changing pumping in the amplifier and reverse bias in the absorber. For example, in the absence of a dc bias, lasing was readily excited in the structures at pumping current amplitudes of about 100 mA. At the same time, the absorption edge of the *p–i–n* structure could be strongly shifted to the long-wavelength region of the spectrum due to the Franz–Keldysh effect by applying a high dc bias and the total optical amplification could be dramatically decreased over the entire frequency range. In this case, lasing was suppressed and an amplified spontaneous emission mode was observed. The emitted radiation had the form of nanosecond pulses with a peak power of hundreds of microwatts.

However, if the injection of carriers in the amplifier is strongly increased at the same dc bias, amplification at the very edge of the spectrum on the long-wavelength side exceeds absorption because of the occupation of bands by carriers and the corresponding decrease in the energy gap width. As a result, photons with an energy that corresponds to an interband transition from the very bottom of bands can freely propagate in the structure to facilitate the establishment of coherency in the ensemble of electron–hole pairs. As noted previously [7, 8], cooperative emission pulses can be generated in this case. Figure 1 shows the time position of a pulse of cooperative emission. The emission was detected using a *p–i–n* photodiode with a resolution of about 400 ps and an S7-13 sampling oscilloscope with a transmission band of 18 GHz. The typical peak power of cooperative emission pulses was higher than the power of spontaneous emission and lasing by 4–5 orders of magnitude.

Figure 2 shows a schematic diagram of the experiment. Emission from a semiconductor structure was collimated with a microlens and directed to a diffraction grating with 600 grooves per millimeter. The diffracted radiation was focused on the entrance slit of a temporal streak camera using a lens with a focal distance of 18 cm. The maximum time resolution of the camera was about 1.5 ps. As a result, the temporal and frequency (wavelength) sweeps of the emission could be simultaneously observed on the camera screen. This procedure is widely used for studying the spectral dynamics of semiconductor lasers that generate ultrashort pulses [13]. The image obtained on the camera screen was read by a CCD camera, whose video signal was supplied to the special video display board of a personal computer and then converted into a two-dimensional digital image, which corresponded to the time-resolved spectrum of the initial optical signal. The linearity of the camera with respect to intensity was checked with special light filters. The temporal sweep was calibrated using the delay of a femtosecond pulse in a quartz plate with a known thickness. The sweep scale on the other coordinate (wavelength) was determined using an MDR-23 monochromator with a resolution of 0.1 nm or better.

The entire spectrum of the dynamic regimes of semiconductor structures was studied in the experiments. As distinct from previous publications [7–11], the aim of this work was to study the behavior of spontaneous emission close to superradiance pulses in terms of time and frequency. Evidently, the intensity of spontaneous emission at a given point in time and at a given wavelength is proportional to the number of electrons that occupy the corresponding energy level in a band at this point in time. Therefore, a conclusion on the intraband electron distribution and its changes in time can be drawn based on a study of the intensity distribution of spontaneous emission with time and wavelength. Various temporal sweeps and attenuator filters under various conditions should be used because of the limited dynamic range of the streak camera, as well as because of a very great difference between the peak powers and time parameters of spontaneous and cooperative emissions. Therefore, it was impossible to obtain a regular shape and duration of superradiance pulses and spontaneous-emission pulses in the same shot.

Figure 3 shows the time sweeps of an optical spectrum in (a) laser and (b) superradiance modes. The duration of the entire time sweep was somewhat greater than 2 ns (see below). In both of the shots, the incoming radiation intensity was chosen in such a way as to detect adequately spontaneous emission, which is much weaker than both laser and cooperative emissions. Therefore, the shots were taken with a great overexposure, and their spectral width and duration were strongly distorted.

Lasing began at a photon energy of 1.430 eV (Fig. 3a). It is very important that spontaneous emission can be clearly seen before and, most importantly, at the onset of lasing and after this point in time. The intensity of spontaneous emission on both sides of the lasing line remained practically constant. Upon the termination of a pumping-current pulse, lasing terminated and residual electron–hole pairs spontaneously annihilated with a characteristic interband-recombination time of 1–2 ns.

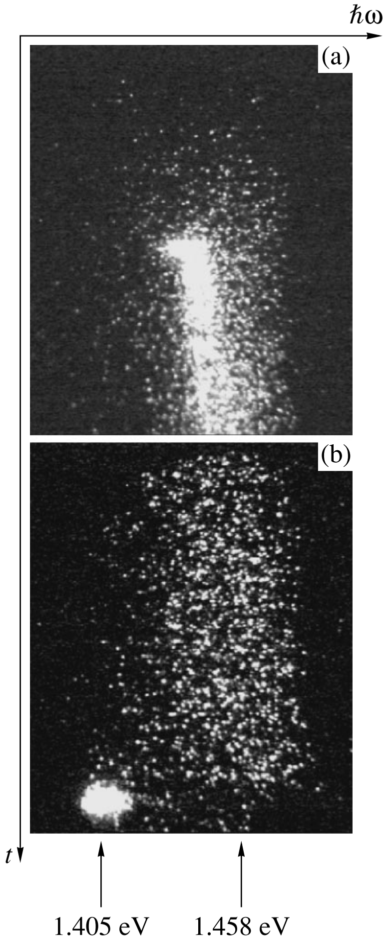

Fig. 3. Temporal sweeps of the optical spectra of (a) laser and (b) cooperative emission pulses.

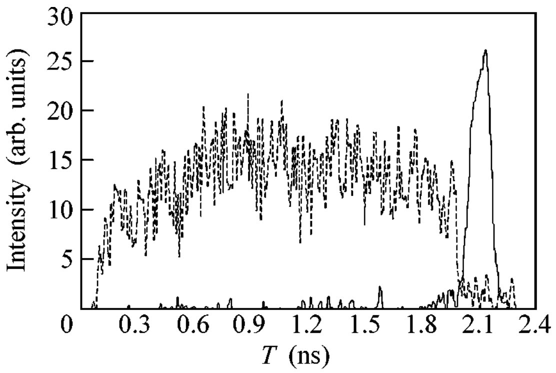

Fig. 4. Time dependence of the intensity of (dashed line) spontaneous emission and (solid line) cooperative emission.

A much different behavior was observed in the superradiance mode (Fig. 3b). The radiation pulse began with ordinary spontaneous emission with a very broad spectrum centered at a photon energy of 1.458 eV. Next, at the end of the pumping-current pulse, the intensity of spontaneous emission at all of the frequencies began to decrease dramatically. At the same time, the development of a cooperative emission pulse began. The entire spectrum of cooperative emission occurred in the range that corresponds to the very edge of a renormalized band gap [7] at an energy of about 1.405 eV. The causes for the strong shift of the spectrum to the long-wavelength region were considered in detail elsewhere [7, 10]. Here, note that, in both laser and superradiance modes, the band gap is narrowed because of the high concentration of carriers as a consequence of correlation effects in a dense *e–h* plasma. A significant difference consists in that the lasing line is shifted by a value of about kT from the band edge inward toward the short-wavelength part. In contrast to this, as mentioned above, the entire spectrum of cooperative emission occurred at the very bottom of the renormalized band.

Figure 4 shows the time dependence of the integrated intensity of the spontaneous emission of electrons from all of the energy levels within a conduction band. It can be clearly seen that the intensity of spontaneous emission dramatically decreased in a time interval of about 2 ns. The duration of this stage was about 100 ps. The intraband thermalization time was no longer than 1 ps, and it was unresolved by the camera.

Simultaneously with this, the intensity of cooperative emission began to increase dramatically. This decrease in the intensity of spontaneous emission can be explained by electron transitions from the depth of a conduction band, collective pairing with holes, and accumulation in the excitonic part of the spectrum at the band bottom. The stability mechanism of a coherent cooperative state at room temperature and the conditions of its formation were described in detail elsewhere [10].

This effect was regularly observed in various ranges of pumping currents and dc bias in the absorber of a semiconductor structure and in various semiconductor structures. Note that the superradiance pulse should be as close as possible to the end of the current pulse in order to observe clearly a “time gap” in emission, as shown in Figs. 3 and 4. In this case, the drop in the current pulse should be sharp; that is, the pulse drop duration should be shorter than the time of interband recombination (<2–3 ns). In this case, the current pulse does not pump additional electrons into the conduction band. If these conditions were not fulfilled, a time gap was also observed; however, its onset was slightly diffused by the spontaneous emission of excess electrons. Note again that the density of injected electrons decreased in an ordinary regime with the time of spontaneous interband recombination longer than the duration of the time gap by an order of magnitude. That is, the decrease in the intensity of spontaneous emission from a band cannot be due to ordinary spontaneous degradation.

Let us consider possible causes for the dramatic decrease observed in the intensity of spontaneous emission. Note that this effect was not observed in either ordinary luminescence (spontaneous emission) or laser mode. It is well known [14] that the rate of spontaneous emission is directly proportional to the product of the probability of an interband transition, the densities of states in the valence and conduction bands, and the probability of occupation of the corresponding energy levels in the bands with electrons and holes. The probability of an interband transition depends on the parameters of a given material, such as the transition matrix element, the electron mass, and the spin–orbital splitting energy. It seems improbable that both these values and the densities of states in bands would suddenly begin to decrease at the end of a pumping pulse. Therefore, the sharp decrease observed in the rate of spontaneous emission means that the occupation probability of levels in the bands (the third term) begins to decrease sharply. In turn, this implies that electrons left the band. In my opinion, the simultaneous rapid increase in the intensity of emission from the band bottom suggests the transition of electrons from the depth of the band to levels at the very bottom, that is, the condensation of electrons in phase space.

Thus, in this work, it was demonstrated in an explicit form how the intensity of spontaneous emission from the entire conduction band decreased dramatically at the earliest step in the development of a superradiance pulse. This decrease in spontaneous emission can be explained by a sharp decrease in the number of electrons within a band, electron pairing, and condensation in the excitonic region of the spectrum at the band bottom. At the same time, the condensation of electron–hole pairs, the formation of a coherent BCS-like state, and the radiative recombination of this state can explain all of the spectral, dynamic, and power characteristics of cooperative emission, which were described previously [7–11]. Although the mechanism of condensation and formation of a BCS-like state was exemplified by the three-section (amplifier/absorber/amplifier) GaAs/AlGaAs heterostructure, it is likely that this is a general mechanism and it can also be used to obtain a condensed *e–h* state in other semiconductor structures.

I am grateful to H. Kan, H. Ohta, and T. Hiruma (Hamamatsu Photonics) for their support of this work and for providing the samples of semiconductor structures and to I.V. Smetanin, V.S. Zuev, and Yu.M. Popov for numerous discussions.

REFERENCES

1. L. V. Keldysh and Yu. V. Kopaev, Fiz. Tverd. Tela (Leningrad) **6**, 2791 (1964) [Sov. Phys. Solid State **6**, 2219 (1964)].

2. *Bose–Einstein Condensation*, Ed. by A. Griffin, D. W. Snoke, and S. Stringari (Cambridge Univ. Press, Cambridge, 1995).
3. D. Snoke, J. P. Wolfe, and A. Mysyrowicz, Phys. Rev. Lett. **64**, 2543 (1990).
4. L. V. Butov, A. L. Ivanov, A. Imamoglu, *et al.*, Phys. Rev. Lett. **86**, 5608 (2001).
5. A. V. Larionov and V. B. Timofeev, Pis'ma Zh. Éksp. Teor. Fiz. **73**, 342 (2001) [JETP Lett. **73**, 301 (2001)].
6. O. M. Schmitt, D. B. Tran Thoai, P. Gartner, *et al.*, Eur. Phys. J. B **16**, 217 (2000).
7. P. P. Vasil'ev, H. Kan, H. Ohta, *et al.*, Zh. Éksp. Teor. Fiz. **120**, 1486 (2001) [JETP **93**, 1288 (2001)].
8. P. P. Vasil'ev, H. Kan, H. Ohta, and T. Hiruma, Phys. Rev. B **64**, 195 209 (2001).
9. P. P. Vasil'ev, H. Kan, H. Ohta, *et al.*, JETP **96**, 310 (2003).
10. P. P. Vasil'ev, Phys. Status Solidi B **241**, 1251 (2004).
11. P. P. Vasil'ev, Usp. Fiz. Nauk **171**, 679 (2001) [Phys. Usp. **44**, 645 (2001)].
12. L. V. Butov, A. Zrenner, G. Abstreiter, *et al.*, Phys. Rev. Lett. **73**, 304 (1994).
13. P. Vasil'ev, *Ultrafast Diode Lasers: Fundamentals and Applications* (Artech House, Norwood, MA, 1995).
14. P. G. Eliseev, *Introduction to the Physics of Injection Lasers* (Nauka, Moscow, 1983) [in Russian].

Translated by V. Makhlyarchuk

JETP Letters, Vol. 82, No. 3, 2005, pp. 120–123. From Pis'ma v Zhurnal Éksperimental'noĭ i Teoreticheskoĭ Fiziki, Vol. 82, No. 3, 2005, pp. 134–137.
Original English Text Copyright © 2005 by Tapia, Canto, Murrieta, de Coss.

Electronic Structure of FCC Carbon[¶]

A. Tapia[a], G. Canto[b], G. Murrieta[a, *], and R. de Coss[a]
[a] *Departamento de Física Aplicada, CINVESTAV—Mérida, 97310 Mérida, Yucatán, México*
e-mail: decoss@mda.cinvestav.mx
[b] *Centro de Ciencias de la Materia Condensada, UNAM, A.P. 2681, Ensenada B.C., México*

Received June 16, 2005

We report first-principles calculations of the electronic structure for carbon in the fcc structure with the experimentally observed lattice parameter. The calculated orbital population shows that the chemical bond in fcc carbon is close to the s^2p^2 bonding with a small s–p hybridization. We find that, in contrast to graphite and diamond, fcc carbon exhibits metallic behavior with an electronic density of states at the Fermi level of 0.5 states/(eV atom). © *2005 Pleiades Publishing, Inc.*

PACS numbers: 71.18.+y, 71.20.Gj, 72.15.Eb

New crystalline phases of a given material are interesting because they correspond to a different bonding arrangement, and new properties can be expected. The face-centered-cubic (fcc) crystal structure does not appear on the usual pressure–temperature phase diagram of carbon [1]. However, the observation of fcc carbon (fcc-C) in nanoparticles and thin films has been reported [2–7]. Palatnik *et al.* [2] were the first to report the observation of the fcc phase of carbon, which was obtained from low-temperature annealing of an amorphous carbon film with simultaneous bombardment of argon ions. After that process, single-crystal inclusions ~100 Å in size with a lattice constant of 3.57 Å and metallic character were observed [2, 3]. Carbon with the fcc crystal structure has also been observed at the core of carbon particles produced by plasma-chemical synthesis [4]. More recently, it was shown that a thin film of fcc carbon is formed on a diamond surface as a result of treatment in a hydrogen plasma [5–7]. The crystal lattice parameter of fcc carbon in thin films was determined by high-resolution transmission electron microscopy to be 3.563 Å [6, 7]. These reports on the existence of carbon thin films and nanoparticles with the fcc structure stimulated us to study the electronic properties of fcc carbon.

The electronic density of states (DOS) of fcc-C has been studied theoretically by means of the empirical tight-binding method [5]. The tight-binding calculation for the DOS indicates that metallic behavior can be expected for fcc carbon. However, the value of the DOS at the Fermi level, as well as an analysis of the electronic structure, has not been given [5]. Thus, first-principles calculations appear to be essential to evaluate the electronic properties of fcc-C, since, to the best of our knowledge, accurate calculations of the electronic structure for fcc-C have not been reported previously.

In this letter, we report a study of the electronic structure of carbon in the fcc structure performed by means of first-principles calculations. We present results for the charge density, band structure, Fermi surface, and density of states. From analysis of the chemical bond and the electronic band structure, we find that fcc-C has a chemical bond very close to an s^2p^2 bonding and exhibits metallic behavior. The DOS at the Fermi level is 0.5 states/(eV atom), and the main contribution comes from p states.

The calculations were performed within the generalized gradient approximation (GGA) to the density functional theory (DFT). The electronic structure of carbon with the fcc structure was determined self-consistently using the pseudopotential LCAO method [8, 9] as implemented in the SIESTA code [8–10]. The carbon pseudopotential was generated according to the procedure of Troullier and Martins [11] from the atomic configuration [He] $2s^22p^2$. The core radii for the s and p orbitals were 1.5 a.u. and 1.25 a.u. for the d and f orbitals. For the expansion of the wave functions, we employed a double-ζ plus polarization basis [10]. The basis for the s and p orbitals was slightly excited (270 meV) in order to limit the range of the pseudoatomic basis orbitals [12]. For the exchange-correlation potential, we used the GGA as parametrized by Perdew, Burke, and Ernzerhof [13]. In order to obtain the potential energy, we used a grid in real space, which was obtained using a mesh cutoff of 250 Ry. Integrals in k space were performed in a finite, uniform grid of the Brillouin zone. The fineness of this grid was controlled by a k-grid cutoff, a real space radius which plays a role equivalent to the plane wave cutoff of the real-space grid [14]. For the present calculation, the k-grid cutoff

---

[¶] The text was submitted by the authors in English.

[*] Present address: Facultad de Matemáticas, Universidad Autónoma de Yucatán, A.P. 172, Cordemex 97310 Mérida, Yucatán, México.

0021-3640/05/8203-0120$26.00 © 2005 Pleiades Publishing, Inc.

was 130 Å, generating 562482 *k* points in the first Brillouin zone. Self-consistency was assumed when the difference between the two density matrix belonging to successive iterations was less than 10^{-4}. The calculation was performed at the experimental lattice parameter for fcc carbon as obtained from high-resolution electron microscopy ($a = 3.563$ Å) [5].

In Fig. 1, we show the calculated valence charge density at the (001) plane of fcc-C, where the steps in the charge density plot correspond to 0.02 electrons/Å^3. We can see that the charge distribution is strongly spherical around the core and mostly homogeneous in the interstitial region, which are features characteristic of a metallic bonding. The electronic configuration of carbon is [He] $2s^22p^2$; therefore, the valence band consists of *s*–*p*-like bands and is relatively simple. The calculated band structure is presented in Fig. 2, where the origin in energy is at the Fermi level (E_F). The first band covering the energy range from –14 to –6 eV below the Fermi level shows a minimum at the Γ point. This band has a strong *s* character and exhibits parabolic behavior around Γ. A second set of bands consists of three bands with a *p* character. It is interesting to note that the *p* bands are separated from the *s* band by an energy gap. The *s*–*p* gap extends from –5.1 to –5.9 eV below the Fermi level. Two *p* bands cross the Fermi level, indicating that fcc carbon is a metal. This result is in qualitative agreement with the observations of electrical conductivity in fcc-C reported by Palatnik *et al.* [2] and Jarkov *et al.* [15].

The Fermi surface properties are of special importance in metal physics, since they are related to the transport coefficients and to the optical properties. In order to gain insight on the transport properties of fcc-C, we have analyzed the Fermi surface. In Fig. 3, we show the surface of constant energy resulting from the two bands crossing the Fermi level in Fig. 2. The Fermi surface was generated using the XCrysDen analysis package [14]. The first Fermi surface (Fig. 3a) corresponding to the band centered at Γ (see Fig. 2) is a closed surface with hole character. In contrast, the second Fermi surface (see Fig. 3b), which corresponds to the band centered at the edges of the first Brillouin zone, forms a multiply connected surface. Hence, the Fermi surface of fcc-C is highly anisotropic, and both kind of charge carriers, “holes” and “electrons,” are present. Therefore, rather complex galvanometric properties are expected for fcc-C, since the charge-carrier orbits on the Fermi surface are not all of a single carrier type.

The calculated electronic density of states (DOS) is shown in Fig. 4, where the origin in energy is at E_F. The top panel corresponds to the total DOS; the middle and lower panels correspond to the *s* and *p* partial contributions, respectively. As was mentioned above, fcc-C exhibits metallic behavior. In particular, we found that the density of states at the Fermi level is 0.5 1/(eV atom) and that the main contribution comes from the *p* states (89%). The lower energy states correspond mainly to *s* states and are separated from the high-energy *p* states by a gap of 0.8 eV. The *s* states have only a small overlap with the *p* states, indicating a small *s*–*p* hybridization. The orbital population by symmetry can be obtained by integrating the partial *s*-DOS and *p*-DOS up to the Fermi level. From this procedure, we find that the number of electrons in the *s* and *p* orbitals is 1.98 and 2.02, respectively. There exists a very small charge transfer of 0.02 electrons from the *s* to the *p* orbitals. Thus, the chemical bond in fcc-C is close to the s^2p^2 bonding.

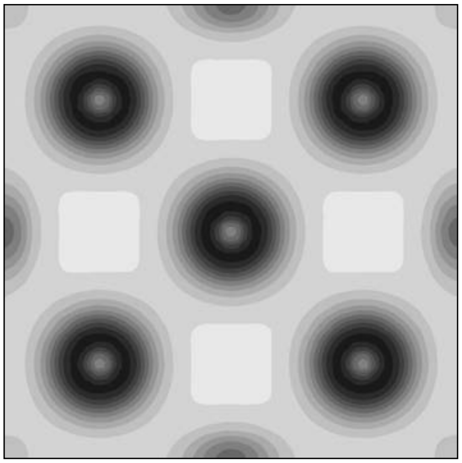

Fig. 1. Charge density map for fcc carbon projected in the (001) plane.

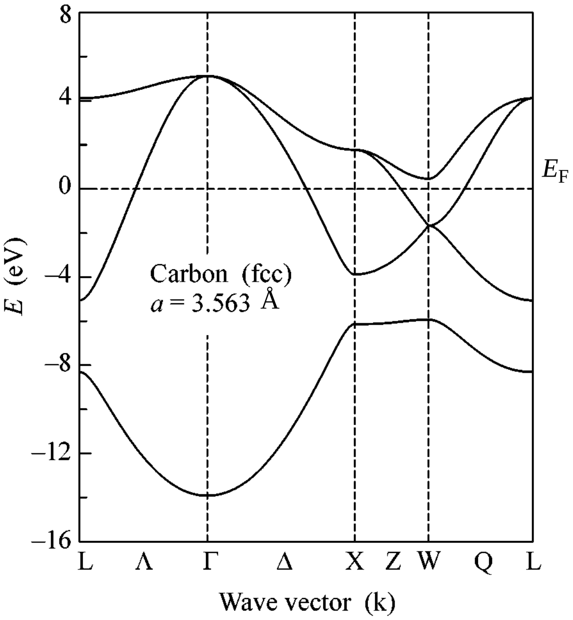

Fig. 2. Electronic band structure for fcc carbon at the experimental lattice parameter ($a = 3.563$ Å).

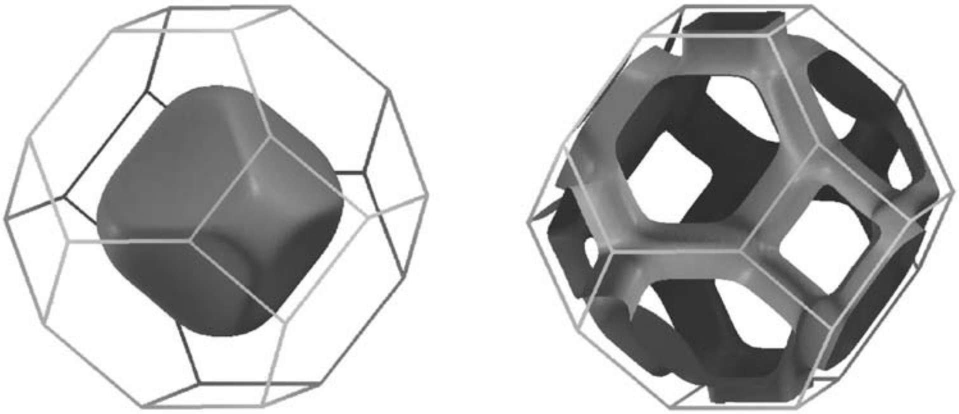

(a) (b)

Fig. 3. Fermi surface for fcc-C, corresponding to the band centered at Γ (a) and to the band centered at the first Brillouin edges (b).

From the results presented above, we can see that the electronic structure of fcc-C is different from the well-known electronic properties of graphite, diamond, and amorphous carbon [17]. Nevertheless, the electronic structure of fcc-C shows a similarity with that of lead (Pb) [18, 19], which is a tetravalent metal-like carbon with an fcc ground state. It is interesting to note that, in both systems, there is an *s*–*p* gap below the Fermi level; however, in Pb, the gap is 3.5 eV [19, 20], which is much larger than for fcc-C (0.8 eV). A small *s*–*p* hybridization is also a feature common between fcc-C and Pb, but, in contrast to fcc-C, the charge transfer in Pb is from the *p* to the *s* orbitals (0.18 electrons) [20]. The Fermi surface for fcc-C has a shape and complexity similar to that of Pb [21]. However, further investigation is necessary to determine the transport properties of fcc carbon, including the superconducting properties, as was pointed out by Palatnik *et al.* [2].

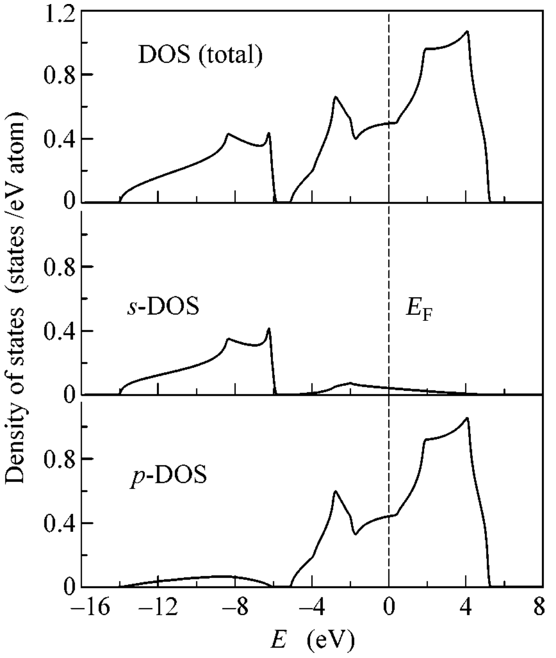

Fig. 4. Density of states for fcc carbon at the experimental lattice parameter (a = 3.563 Å).

In summary, we have calculated the electronic structure of fcc carbon using a first-principles pseudopotential LCAO method. We find that the electronic structure of fcc carbon is clearly different from those of graphite and diamond. The results show that fcc-C has a chemical bond very close to the s^2p^2 bonding and is a metal with a DOS at E_F of 0.5 states/(eV atom). The metallic behavior obtained from the present calculations for fcc-C is in agreement with the experimental observation of high electrical conductivity in thin films of carbon with the fcc structure. The Fermi surface of carbon in the fcc structure has a similar complexity as Pb(fcc). Thus, metallic fcc carbon is expected to have unique electronic properties.

The authors would like to thank G. Oskam and Aarón Aguayo for a critical reading of the manuscript. A.T. and G.M. gratefully acknowledge a student fellowship from Consejo Nacional de Ciencia y Tecnología (CONACYT, México) and CINVESTAV. This research was supported by CONACYT-México (grant nos. 34501-E and 44831).

REFERENCES

1. D. A. Young, *Phase Diagrams of the Elements* (Univ. of California Press, California, 1991).
2. L. S. Palatnik, M. B. Guseva, V. G. Babaev, *et al.*, Sov. Phys. JETP **60**, 520 (1984).
3. N. F. Savchenko, M. B. Guseva, V. G. Babaev, and L. S. Palatnik, Phys. Chem. Mech. Surf. **4**, 1816 (1986).
4. S. M. Jarkov, Y. N. Titarenko, and G. N. Churilov, Carbon **36**, 595 (1998).

5. I. Konyashin, A. Zern, J. Mayer, *et al.*, Diamond Relat. Mater. **10**, 99 (2001).
6. I. Konyashin, V. Babaev, M. Guseva, *et al.*, Vacuum **66**, 175 (2002).
7. M. Fatow, I. Konyashin, V. Babaev, *et al.*, Vacuum **68**, 75 (2003).
8. P. Ordejón, E. Artacho, and J. M. Soler, Phys. Rev. B **53**, 10 441 (1996).
9. P. Ordejón, Phys. Status Solidi B **217**, 335 (2000).
10. J. M. Soler, E. Artacho, J. D. Gale, *et al.*, J. Phys.: Condens. Matter **14**, 2745 (2002).
11. N. Troullier and J. L. Martins, Phys. Rev. B **43**, 1993 (1991).
12. O. F. Sankey and D. J. Niklewski, Phys. Rev. B **40**, 3979 (1989).
13. J. Perdew, K. Burke, and M. Ernzerhof, Phys. Rev. Lett. **77**, 3865 (1996).
14. J. Moreno and J. M. Soler, Phys. Rev. B **45**, 13 891 (1992).
15. S. M. Jarkov, V. S. Zhigalov, and G. I. Frolov, in *Proceedings of Conference on Ultrafine Powders, Materials and Nanostructures* (Krasnoyarsk, Russia, 1996), p. 29.
16. A. Kokalj, J. Mol. Graph. Model. **17**, 176 (1999); http://www-k3.ijs.si/kokalj/xc/XCrySDen
17. G. Galli, R. Martin, R. Car, and M. Parrinelo, Phys. Rev. B **42**, 7470 (1990).
18. A. D. Zdetsis, E. N. Economou, and D. A. Papaconstantopoulos, J. Phys. F: Met. Phys. **10**, 1149 (1980).
19. K. Horn, B. Rihl, A. Zartner, *et al.*, Phys. Rev. B **30**, 1711 (1984).
20. D. A. Papaconstantopoulos, *Handbook of the Band Structure of Elemental Solids* (Plenum, New York, 1986), p. 221.
21. T. S. Choy, J. Naset, J. Chen, *et al.*, http://www.phys.ufl.edu/fermisurface/

JETP Letters, Vol. 82, No. 3, 2005, pp. 124–128. Translated from Pis'ma v Zhurnal Éksperimental'noĭ i Teoreticheskoĭ Fiziki, Vol. 82, No. 3, 2005, pp. 138–143.
Original Russian Text Copyright © 2005 by Lebedev, Kukushkin, Parakhonskiĭ, Kirpichev, Volkov, von Klitzing.

Fluctuations of the Intersubband Splitting Energy and the Potential Well Shape of Two-Dimensional Electrons in the Quantum Hall Effect Regime

M. V. Lebedev[a], I. V. Kukushkin[a], A. L. Parakhonskiĭ[a], V. E. Kirpichev[a], O. V. Volkov[a], and K. von Klitzing[b]

[a] *Institute of Solid-State Physics, Russian Academy of Sciences, Chernogolovka, Moscow region, 142432 Russia*
[b] *Max-Planck-Institut für Festkörperforschung, 70569 Stuttgart, Germany*

Received May 3, 2005; in final form, June 20, 2005

Recombination radiation and inelastic light scattering spectra of 2D electrons are studied simultaneously in structures with a single GaAs quantum well in the quantum Hall effect regime. It is found that the intensity of intersubband inelastic light scattering (the SDE mode) at the filling factor $\nu = 2$ exhibits fluctuations in phase with fluctuations of the photoluminescence intensity of 2D electrons of the ground subband. It is shown that, simultaneously with fluctuations of the scattered light and recombination radiation intensities, the spectral positions of these lines change stepwise by 0.3–0.5 meV. The jumps found in the spectral positions of lines are observed only in narrow intervals of magnetic fields corresponding to the quantum Hall effect and are presumably associated with zero-point fluctuations (Casimir–Lifshits force). © *2005 Pleiades Publishing, Inc.*

PACS numbers: 73.43.–f

1. In our recent works, giant fluctuations of the recombination radiation intensity of two-dimensional (2D) electrons in the quantum Hall effect (QHE) regime have been detected in heterostructures with single [1, 2] and double [3] quantum wells. These results pointed to qualitative changes in the properties of the electron system in a very narrow interval of magnetic fields corresponding to integer filling of Landau levels; however, quantitative measurements characterizing these measurements have not been reported to date. In this work, we have studied the inelastic light scattering spectra of 2D electrons in structures with a single GaAs quantum well and found that the intensity of intersubband inelastic light scattering at the filling factor $\nu = 2$ also exhibits giant fluctuations; in this case, simultaneously with fluctuations of the scattered light intensity, a stepwise change by 0.3–0.5 meV is observed in the Raman shift. The stepwise variation in the spectral positions of intersubband inelastic light scattering lines unambiguously points to sharp changes in the quantum well shape in the quantum Hall effect regime.

As was shown in our first work devoted to studying anomalous intensity fluctuations, in which transport and optical measurements were performed simultaneously, sharp jumps in optical spectra occur only at minima of the diagonal resistance, that is, at integer values of the Landau level filling factor. Figure 1 demonstrates the magnetic-field dependence of the noise amplitude (the dispersion to mean intensity ratio) in the vicinity of the filling factor $\nu = 2$. It is seen that anomalous fluctuations of the 2D-electron radiation intensity are observed in an extremely narrow range of magnetic fields corresponding to filling factor values $1.996 < \nu < 2.004$. The inset in the figure shows time dependences of the 2D-electron radiation intensity measured at the radiation line maximum for two, very close magnetic field values one of which corresponds to the exactly integer filling factor $\nu = 2$ and the other only insignificantly (by 1%) differs ($\nu = 1.98$). It is seen that even such a small change in the filling factor leads to a dras-

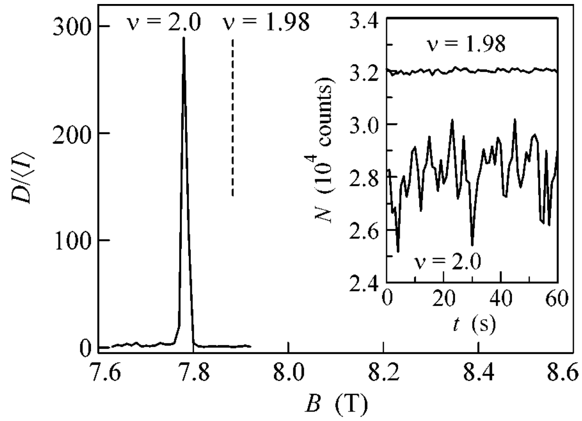

Fig. 1. Magnetic-field dependence of the dispersion to mean intensity ratio for the photoluminescence of the ground size-quantization subband. The inset shows time dependences of the intensity measured for two magnetic field values (7.78 T ($\nu = 2$) and 7.88 T ($\nu = 1.98$)). The magnitude of fluctuations is anomalously high in the vicinity of the filling factor $\nu = 2$.

tic change in the fluctuation characteristics of the radiation intensity: while the radiation intensity noise outside the QHE regime corresponds to Poisson behavior, the noise amplitude increases by several orders of magnitude at integer filling factors. In this case, the dispersion to mean intensity ratio $D/\langle I\rangle$ at $\nu = 2$ reaches 300, which is more than two orders of magnitude higher than the ratio measured at $\nu = 1.98$ (see Fig. 1). Note that the giant fluctuation peak width in the quantum Hall effect regime in various samples can comprise from 0.01 to 0.0001 of the filling factor.

One might try to explain this effect in the following way. A 2D layer and a delta layer represent plane capacitor plates with the capacitance C. A positive charge $+q$ in the delta layer induces a charge $-q$ near the 2D layer. The 2D layer in the QHE regime is an insulator, and its conductivity is determined by electron hops between localized states and is exponentially small:

$$\sigma_{xx} \sim \exp(-\Delta E/T), \tag{1}$$

where ΔE is a gap, which equals half the cyclotron energy at $\nu = 2$. A capacitor attains an equilibrium in the time C/σ_{xx}. The recharging process of such a capacitor is discrete and is determined by temperature-dependent hopping conductivity. Each charge jump at the capacitor plates means a change in the electric field energy and can be a source of noise. The 2D electron temperature, which determines the conductivity of the electron system, must serve as the most important factor in the framework of this model. Significant variations in the magnetic-field dependence of noise, its intensity, and time characteristics should be expected as the temperature decreases, because the conductivity of the electron system exponentially depends on temperature. However, this is not so. In our experiments, it was stated that noise appears stepwise with decreasing temperature whose amplitude (D/N) remains unchanged after a threshold in a wide temperature range. Figure 2 demonstrates temperature dependences of the noise amplitude measured for various filling factors. The temperature threshold for $\nu = 2$ ($B = 7.3$ T) is observed at $T = 1.75$ K, the threshold equals $T = 0.5$ K for $\nu = 1$ ($B = 10.5$ T), and the threshold temperature turns out to be 0.1 K for the fractional filling $\nu = 1/3$. It should be emphasized that the variation of the noise amplitude has a threshold character in temperature and indicates that a certain threshold resistance (about 10^{15} Ω) must be reached for fluctuations to be observed after which the noise amplitude remains unchanged. The smaller the gap in the energy spectrum, the lower the temperature required to reach the threshold resistance. Note that a decrease in temperature does not lead to a shift of the noise peak in a magnetic field and the spectral and time characteristics of noise do not change. Thus, it should be inferred that only the transition to a state with an anomalously low conductivity is important for the occurrence of noise.

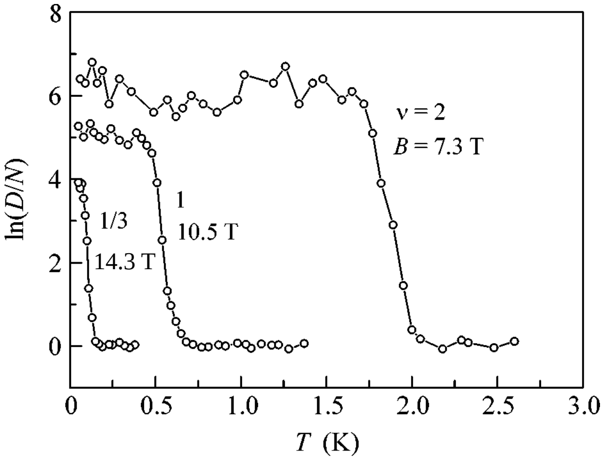

Fig. 2. Temperature dependence of the normalized dispersion of 2D-gas photoluminescence intensity noise at various Landau level filling factors.

The occurrence of a new coherent macroscopic state of the electron system possessing a common wave function can serve as the second of the possible explanations. Such a scenario was considered in our previous papers devoted to a study of giant fluctuations [2, 3]. However, in the framework of this approach, it is not seen how the potential well shape can vary and, therefore, it cannot explain the fluctuations that we observed in the spectral positions of Raman scattering lines.

The additional contribution of the so-called Casimir force, which originates from vacuum fluctuations of the electromagnetic field, to the interlayer interaction is the third hypothetical possibility. Under quantum Hall effect conditions, small electron-density fluctuations can give rise to giant fluctuations of the conductivity of the 2D-electron system (with an amplitude of several orders of magnitude) and lead to fluctuation metal–insulator transitions. The energy of zero-point oscillations of the electromagnetic field in the space restricted by the delta layer and the quantum well depends on the metal–insulator transition in the 2D gas. Its change generates a change in the potential well shape and in the intersubband splitting energy. It turns out that the measured amplitude of energy jumps in the intersubband energy agrees well with the estimate of the size-quantization energy ΔE obtained from the change in the effective electric field and the Casimir force upon the metal–insulator transition in the quantum Hall effect regime.

Recall that the Casimir force arises from vacuum fluctuations of the electromagnetic field. According to the result obtained by Casimir in 1948 [4, 5], an attractive force arises between two parallel metallic planes, which is proportional to the area of the planes and is inversely proportional to the fourth degree of the distance between them. This force becomes dominating at distances less than 100 nm and, apparently, it is this force that determines the workability of micromechan-

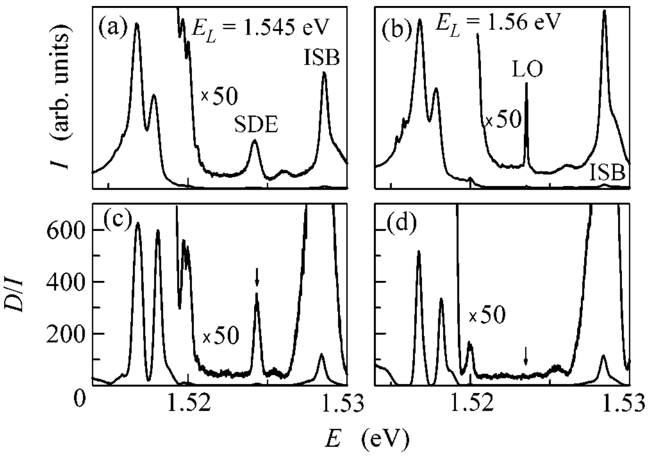

Fig. 3. Photoluminescence and inelastic light scattering spectra measured in the regime of giant fluctuations under quantum Hall effect conditions at the filling factor $\nu = 2$ for various pump photon energies E_L: (a) 1.545 and (b) 1.560 eV. In the first case (a) an intersubband SDE mode of 2D electrons is observed in the spectrum, and scattering by the bulk LO phonon is observed in the second case (b). Figure 2c, 2d shows the spectral dependences of the dispersion to mean intensity ratio measured at various excitation energies. It is seen that both the photoluminescence lines and the SDE line of inelastic light scattering exhibit giant fluctuations in the quantum Hall effect regime at $\nu = 2$. At the same time, the LO line exhibits no noticeable fluctuations.

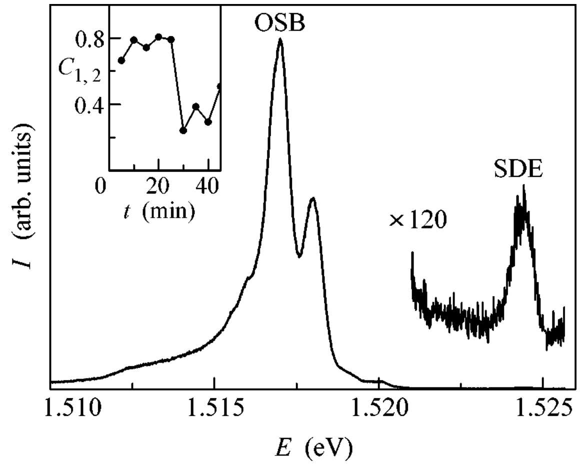

Fig. 4. Photoluminescence spectrum and the intersubband inelastic light scattering line (SDE mode) measured in the regime of giant fluctuations under quantum Hall effect conditions at the filling factor $\nu = 2$. The inset shows the time variation of the correlation coefficient $C_{1,2}$ between the intensities of the inelastic scattering line and the photoluminescence line from the upper spin sublevel of the ground size-quantization subband (0SB).

ical devices, as is manifested in the anomalously large static friction force detected in these mechanisms [6].

The measurement of the Casimir force is connected with great experimental difficulties, and experiments that reliably confirm its occurrence have been performed only quite recently [7, 8].

The classical geometry with parallel metallic planes has been used for the determination of the Casimir force only in rare experiments. This is connected with the fact that it is extremely difficult to provide the parallelism of the planes especially because of their irregularity and roughness; it is also difficult to distinguish electrostatic attraction from Casimir attraction. Moreover, one cannot but note that all the measurements of the Casimir force have usually been performed at room temperature. However, the theoretical result was obtained for the case of low temperatures and the contribution from thermal fluctuations at room temperature can be significant especially when the distance between the planes increases. We believe that single and double quantum wells can be a promising object for studying the properties of the Casimir force. Two-dimensional layers separated by a distance of 10–100 nm can be grown by molecular beam epitaxy so that these layers are parallel to each other with a high degree of accuracy. The properties of such layers can be studied at low temperatures by optical and transport methods.

2. Samples with a single GaAs quantum well 250 Å thick were studied. The electron concentration and mobility in the well were approximately 4×10^{11} cm^{-2} and 2×10^{6} cm^{2} V^{-1} s^{-1}, respectively. The structures were excited by light from a laser light emitting device (LED) with a photon energy of 1.653 eV and from Ti–Sp laser with a tunable wavelength. The spectral instrument was a Monospec spectrometer with a spectral resolution of 0.03 meV. The photoluminescence and inelastic light scattering signals were detected by a charge-coupled device (CCD) detector. A sample was placed in a helium cryostat inside a superconducting solenoid. A two-waveguide design was used in this work: the first waveguide was intended for the supply of LED and Ti–Sp laser radiation, and the second waveguide was used for collecting the luminescence inelastic scattering signals. The spectra were processed mathematically simultaneously with their recording, as described in detail in [2]. To measure the intensity fluctuation amplitude, a series of spectra were recorded on the CCD detector and the mean radiation intensity $\langle I \rangle$, the dispersion $D = \langle I^2 \rangle - \langle I \rangle^2$, and the dispersion to mean intensity ratio $D/\langle I \rangle$ were then determined from this series for each wavelength.

3. Studying the inelastic light scattering spectra in the QHE regime (in particular, in the vicinity of $\nu = 2$), we found that the signal intensity of intersubband Raman scattering in the quantum well (spin density excitation, the SDE mode [9, 10], Fig. 3a) exhibits giant intensity fluctuations (Fig. 3c) similar to luminescence intensity fluctuations. At the same time, if fluctuations of the light scattering intensity are studied in the quantum Hall effect regime on a bulk longitudinal optical (LO) phonon, the $D/\langle I \rangle$ ratio in this case turns out to be equal to unity (see Fig. 3d), which indicates the two-dimensional nature of anomalous fluctuations of the SDE mode of inelastic light scattering. Figure 4 demonstrates the photoluminescence spectrum of the ground subband (0SB) electrons and the inelastic scattering line (SDE) measured in the regime of giant fluctuations under quantum Hall effect conditions ($\nu = 2$). It proved that fluctuations of the SDE mode intensity are observed simultaneously and in phase with fluctuations of the photoluminescence intensity and the recombination and inelastic light scattering processes proceed consistently over a long period of time. The inset in Fig. 4 shows the time dependence of the correlation coefficient $C_{1,2} = \langle \Delta I_1 \Delta I_2 \rangle/(D_1 D_2)^{1/2}$ calculated between the SDE line and the photoluminescence line corresponding to recombination from the upper spin sublevel of the ground subband (0SB). In our previous works, we also analyzed the correlation coefficient to reveal the correlated (in-phase) character of intensity fluctuations of 2D-electron radiative recombination either between the spectral lines from the upper and lower spin sublevels of the ground subband or between the lines from the ground and first excited size-quantization subbands. In this work, an analogous method was used for the SDE and 0SB lines. In the inset in Fig. 3, it is seen that intensity fluctuations of these lines have a positive correlation coefficient and its maximum value is close to unity. In addition to fluctuations in the inelastic light scattering intensity, we found that the SDE line in the vicinity of the filling factor $\nu = 2$ changes stepwise its spectral position. Figure 5 demonstrates intersubband inelastic light scattering spectra (the SDE mode) measured at different instants of time at the factor $\nu = 2$. It is seen in the figure that the SDE line exhibits telegraph noise with the amplitude of spectral fluctuations $\Delta E = 0.3$–0.5 meV. The inset in Fig. 5 demonstrates time dependences of the spectral position of the SDE line and the photoluminescence line from the upper spin sublevel of the ground size-quantization subband (0SB). It is evident that the spectral shift of both lines occurs simultaneously and is close for both lines in its value. This effect is observed in an extremely narrow range of magnetic fields corresponding to the QHE regime ($1.999 < \nu < 2.001$) and indicates that a sharp change in the well shape occurs in the vicinity of the factor $\nu = 2$. Analyzing the obtained results, we may suggest the following explanation of the phenomena described above. Under the strict fulfillment of the integer QHE condition, small electron-density fluctuations give rise to giant fluctuations of the conductivity of the two-dimensional electron system and to fluctuation metal–insulator transitions in this system. The interaction between the quantum well and the delta layer of donors determines the effective electric field, which is in its turn responsible for the potential well shape and the size-quantization energy of 2D electrons. In addition to the Coulomb attraction, the Casimir force also makes a contribution to the interlayer interaction. Because metal–insulator transitions under QHE conditions by themselves are fluctuations in nature, the Casimir force also fluctuates and generates fluctuation changes (jumps) in the subband splitting energy and the well shape. Note that the two-dimensional electron gas and the delta layer of donors are in essence two parallel layers separated by a dielectric layer, while the conductivity of these layers depends on the magnetic field. This system reminds a classical Casimir scheme comprising two parallel planes in a vacuum between which the Casimir force dominates at small distances. As is known, an attractive force (the Casimir force [4, 5]) arises between such planes as a result of the occurrence of zero-point fluctuations of the electromagnetic field:

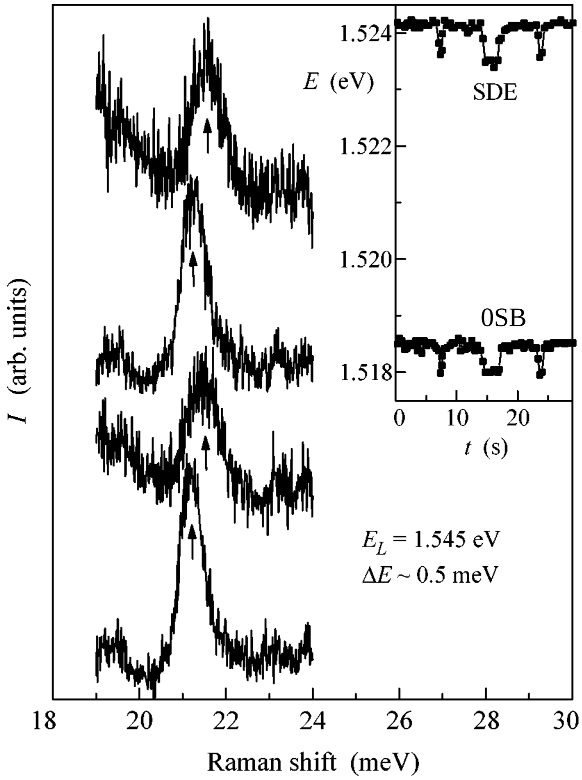

Fig. 5. Spectra of the intersubband SDE mode measured at different instants of time at all the parameters fixed and $\nu = 2$. The SDE line in the quantum Hall effect regime exhibits time instability and manifests a fluctuation spectral shift $\Delta E \approx 0.5$ meV. The inset shows time dependences of the spectral position of the SDE line and the photoluminescence line from the upper spin sublevel of the ground size-quantization subband (0SB).

$$F = \pi^2 \hbar c / 240 l^4, \qquad (2)$$

where F is the force per unit area and l is the distance between the planes. In the vicinity of an integer filling factor, the conductivity of a two-dimensional electron gas changes by five–seven orders of magnitude, which must lead to a significant change in the interaction force between the planes [11]. If it is considered that the change (due to the metal–insulator transition in the QHE regime) in the Casimir force acting on an electron is equivalent to the change in the effective electric field, then the change in energy per electron can be estimated by the equation

$$\Delta E = Fd/N_s, \tag{3}$$

where d is the quantum well width and N_s is the concentration of 2D electrons.

In Eq. (2), we used the fact that the intersubband splitting E_{01} is proportional to the electric field $\mathcal{E}$ in the well [12] and that the change in the intersubband energy ΔE_{01} is determined by the change in the electric field $\Delta\mathcal{E}$ and can be written for an estimation as

$$\Delta E_{01} \sim \Delta\mathcal{E}ed. \tag{4}$$

Because, in our case, $l \cong 600$–700 Å, $d \cong 250$ Å, and $N_s \cong 4 \times 10^{11}$ cm^{-2}, we obtain that $\Delta E = 2$–4 meV. This agrees well in order of magnitude with the experimental value. It is clear that such a simplified estimate cannot serve as evidence for the validity of the above suggestion. However, this estimate provides a characteristic scale of possible interaction and indicates that the effect of the Casimir force is not small and must be properly taken into account. In addition, as follows from [11], in the case of a metal–insulator transition, a coefficient close to 1/3 appears in Eq. (1), because of which the estimate for the Casimir force becomes quite close to the measured value of ΔE. Hence, the amplitude of intersubband energy fluctuations obtained in our experiments agrees with the estimate of the change in the size-quantization energy due to the change in the effective electric field and the Casimir force upon the metal–insulator transition under QHE conditions.

4. Thus, from the simultaneous study of giant fluctuations in the intensities and positions of luminescence lines of 2D electrons of the ground subband (0SB) and lines of electron intersubband inelastic light scattering, it was found that these lines in the vicinity of the factor $\nu = 2$ (in a fixed magnetic field) exhibit a similar spectral shift and their intensities correlate with each other. The stepwise change in the spectral positions of the lines can be a consequence of the sharp change in the quantum well shape due to the threshold metal–insulator transition in the QHE regime and to a fluctuation of the Casimir force. In the end, this allows these changes in the strength of interaction between the layers to be detected by the variation of the well shape and the intersubband splitting energy.

REFERENCES

1. O. V. Volkov, I. V. Kukushkin, M. V. Lebedev, *et al.*, Pis'ma Zh. Éksp. Teor. Fiz. **71**, 558 (2000) [JETP Lett. **71**, 383 (2000)].
2. M. V. Lebedev, I. V. Kukushkin, and O. V. Volkov, Pis'ma Zh. Éksp. Teor. Fiz. **77**, 345 (2003) [JETP Lett. **77**, 295 (2003)].
3. M. V. Lebedev, O. V. Volkov, A. L. Parakhonskiĭ, *et al.*, Pis'ma Zh. Éksp. Teor. Fiz. **80**, 363 (2004) [JETP Lett. **80**, 317 (2004)].
4. H. B. G. Casimir, Proc. K. Ned. Akad. Wet. **51**, 793 (1948).
5. H. B. G. Casimir and D. Polder, Phys. Rev. **73**, 360 (1948).
6. E. Buks and M. L. Roukes, Phys. Rev. B **63**, 033402 (2001).
7. S. K. Lamoreaux, Phys. Rev. Lett. **78**, 5 (1997).
8. G. Bressi *et al.*, Phys. Rev. Lett. **88**, 041 804 (2002).
9. A. Pinczuk, B. S. Dennis, D. Heiman, *et al.*, Phys. Rev. Lett. **68**, 3623 (1992).
10. L. V. Kulik, I. V. Kukushkin, V. E. Kirpichev, *et al.*, Phys. Rev. Lett. **86**, 1837 (2001).
11. E. M. Lifshitz, Zh. Éksp. Teor. Fiz. **29**, 94 (1955) [Sov. Phys. JETP **2**, 73 (1955)].
12. S. Ernst, A. R. Goni, K. Syassen, and K. Eberl, Phys. Rev. Lett. **72**, 4029 (1994).

Translated by A. Bagatur'yants

JETP Letters, Vol. 82, No. 3, 2005, pp. 129–133. Translated from Pis'ma v Zhurnal Éksperimental'noĭ i Teoreticheskoĭ Fiziki, Vol. 82, No. 3, 2005, pp. 144–148.
Original Russian Text Copyright © 2005 by Mitsen, Ivanenko.

Mechanism of Carrier Generation and the Origin of the Pseudogap and 60 K Phases in YBCO

K. V. Mitsen and O. M. Ivanenko
Lebedev Physical Institute, Russian Academy of Sciences, Moscow, 119991 Russia
e-mail: mitsen@sci.lebedev.ru

Received May 16, 2005; in final form, June 20, 2005

The mechanism of hole carrier generation is considered in the framework of a model assuming the formation of negative U centers (NUCs) in HTSC materials under doping. The calculated dependences of carrier concentration on the doping level and temperature are in quantitative agreement with experiment. An explanation is proposed for the pseudogap and 60 K phases in $YBa_2Cu_3O_{6+\delta}$. It is assumed that a pseudogap is of superconducting origin and arises at temperature $T^* > T_{c\infty} > T_c$ in small nonpercolating clusters as a result of strong fluctuations in the occupancy of NUCs ($T_{c\infty}$ and T_c are the superconducting transition temperatures of an infinitely large and finite NUC clusters, respectively). The $T^*(\delta)$ and $T_c(\delta)$ dependences calculated for $YBa_2Cu_3O_{6+\delta}$ correlate with experimental dependences. In accordance with the model, the region between $T^*(\delta)$ and $T_c(\delta)$ is the range of fluctuations in which finite nonpercolation clusters fluctuate between the superconducting and normal states due to NUC occupancy fluctuations. *© 2005 Pleiades Publishing, Inc.*

PACS numbers: 74.20.Mn, 74.40.+k

INTRODUCTION

Previously [1–3], we proposed a mechanism of formation of diatomic negative U centers (NUCs) in HTSC materials and proved that many anomalous properties of high-T_c superconductors may result from the interaction of electrons from the oxygen band with these NUCs [2]. This interaction leads to strong renormalization of the effective electron–electron interaction when scattering processes with intermediate virtual bound states are taken into account [4–13]. In addition, NUCs play the role of pair acceptors leading to generation of hole carriers in the CuO_2 plane. It follows from the model that it is these carriers that, in contrast to localized doped charges, ensure conduction in the normal state. Here, using $YBa_2Cu_3O_{6+\delta}$ as an example, we will prove that the proposed model [1–3] makes it possible to explain from a unified point of view the dependence of hole carrier concentration on doping level δ and temperature, as well as the dependence of the superconducting transition temperature T_c and temperature T^* of emergence of a pseudogap on the doping level.

1. Formation of NUCs and generation of hole carriers. According to [1–3], an NUC is formed in $YBa_2Cu_3O_{6+\delta}$ at a certain given pair of Cu ions in the CuO_2 plane in the presence of three occupied oxygen positions in succession above (under) this pair of ions in a CuO_3 chain (Fig. 1a). The total concentration of such oxygen "triads" for a random distribution of oxygen ions in the chains is equal to δ^3 (when recalculated per unit cell of $YBa_2Cu_3O_{6+\delta}$).

An isolated triad of oxygen ions forms two NUCs in a chain (one NUC in each of the two CuO_2 planes; Fig. 1a). However, in a sequence with a number of oxygen ions $N_O > 3$ in a chain, only every second triad may form individual NUCs (having no common Cu ion in common) in each of the CuO_2 planes (Fig. 1b). Hence, we can also assume that, for $N_O > 3$, each triad forms an NUC, but only in one CuO_2 plane (Fig. 1b).

We will assume that several NUCs lying on the same straight line in the CuO_2 plane belong to the same one-dimensional (1D) cluster if the copper ions at which NUCs are formed form a continuous 1D cluster of lattice sites in a given CuO_2 plane. Accordingly, oxygen ions in chains, which constitute the given 1D NUC

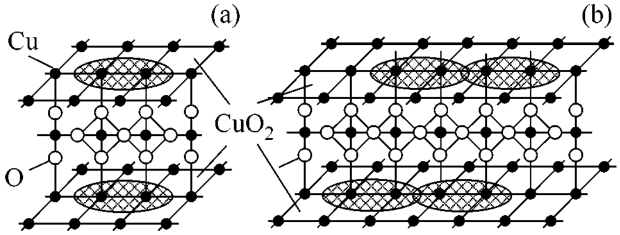

Fig. 1. (a) Formation of (hatched) NUC in $YBa_2Cu_3O_{6+\delta}$ at a certain given pair of Cu ions in the CuO_2 plane in the presence of three successively filled oxygen positions in a CuO_3 chain above (below) this pair of ions, and (b) formation of NUC clusters in CuO_2 planes by a sequence of oxygen ions in chains.

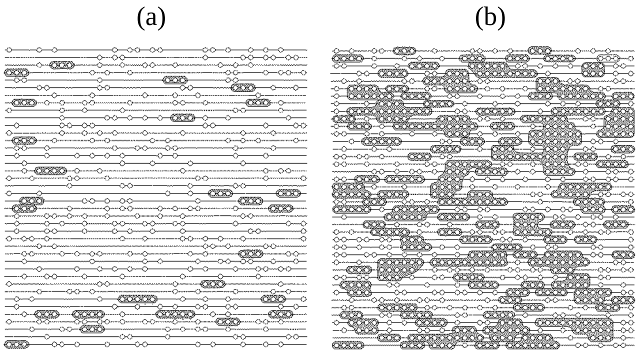

Fig. 2. Clusters of oxygen ions in chains forming finite NUC clusters for a random distribution with δ = (a) 0.3 and (b) 0.6. Light symbols correspond to oxygen ions in chains, and clusters of oxygen ions with $N_O \geq 3$ are hatched.

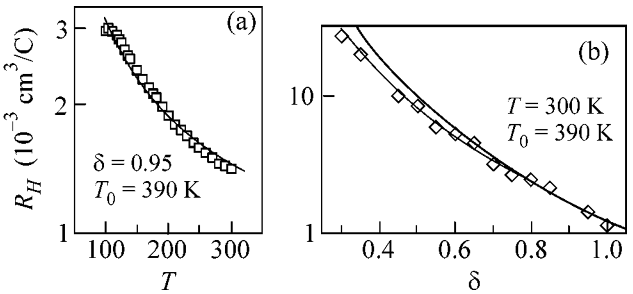

Fig. 3. Hall constant in a monodomain $YBa_2Cu_3O_{6+\delta}$ single crystal vs. (a) temperature and (b) doping level: (a) open squares correspond to $R_H(T)$ for $\delta = 0.95$ [14]; (b) open diamonds are $R_H(\delta)$ at T = 300 K [14]. The thick curves in both panels show dependence (3) for T_0 = 390 K and $T_{c\infty}$ = 92 K. The thin curve describes the $R_H(\delta)$ dependence obtained with the inclusion of the additional contribution from isolated “triads” of oxygen ions in chains.

cluster, form a continuous oxygen 1D cluster in the plane of the chains.

Thus, each 1D NUC cluster in a CuO_2 plane corresponds to a continuous generating cluster of oxygen ions in a CuO_3 chain. We assume that continuous sequences of oxygen ions corresponding to neighboring chains form a single two-dimensional (2D) NUC cluster if these sequences “overlap” over three or more oxygen ions in neighboring chains (i.e., NUC percolation takes place). This corresponds to the formation of continuous 2D NUC clusters in CuO_2 planes. NUC percolation sets in for a certain critical oxygen concentration $\delta = \delta_c$, which can be determined for a random distribution of oxygen ions in the chains using the Monte Carlo technique. Figure 2 shows the patterns of random distribution of oxygen ions in the chains for $\delta = 0.3$ and $\delta = 0.6$, which were obtained using this method for a 40×40 mesh.

The total (for both CuO_2 planes) number of NUCs in clusters per unit cell of $YBa_2Cu_3O_{6+\delta}$ for a random distribution of oxygen ions is $N_U = \delta^3 + N_3(\delta)$, where $N_3(\delta)$ is the number of isolated triads of oxygen ions in the chains, which is a function of δ: $N_3(\delta) = \delta^3(1-\delta)^2$. Accordingly, we can write

$$N_U(\delta) = \delta^3\{1 + (1-\delta)^2\}. \qquad (1)$$

In other words, $N_U(\delta) \longrightarrow \delta^3$ for $\delta \longrightarrow 1$, when the major part of NUCs belongs to large clusters (see Fig. 2). It follows from relation (1) that $N_U(\delta) \approx \delta^3$ with an error less than 10% even for $\delta > 0.7$. For $\delta < \delta_c$, NUCs form finite clusters of various sizes. In each cluster, the NUC occupation numbers η and, hence, the concentration of holes generated in a CuO_2 plane per NUC are functions of temperature and are given by [1, 2]

$$\eta = 2T/(T + T_0), \qquad (2)$$

where T_0 is a temperature-independent constant, which can be determined from Hall measurements. It follows from Eq. (1) that, for $\delta > 0.7$, the volume NUC concentration $P = N_U/V_{UC} = \delta^3/V_{UC}$, where $V_{UC} = 173$ Å^3 is the unit cell volume in $YBa_2Cu_3O_{6+\delta}$. Accordingly, the volume concentration n of hole carriers generated in CuO_2 planes during filling of NUCs with electrons is $n = \eta P = \eta\delta^3/V_{UC} = 2(\delta^3/V_{UC})T/(T + T_0)$, while the Hall constant is given by

$$R_H(\delta, T) = 1/ne = (1/2e)(V_{UC}/\delta^3)(T + T_0)/T, \qquad (3)$$

where e is the elementary charge. Figure 3a shows the temperature dependence of the Hall constant in a $YBa_2Cu_3O_{6.95}$ single crystal from [14], in which the contributions to the Hall constant from CuO_2 planes and chains can be separated using monodomain $YBa_2Cu_3O_{6+\delta}$ single crystals without twins for various values of δ. It can be seen from Fig. 3 that these data can be described to a high degree of accuracy using Eq. (3) with $T_0 \approx 390$ K.

Figure 3b shows the experimental dependence $R_H(\delta)$ for T = 300 K, which was also obtained in [14]. It can be seen that experimental data are successfully described by dependence (3) with T_0 = 390 K in the range $0.7 < \delta < 1$. In accordance with the above arguments, the contribution from isolated triads becomes significant for $\delta < 0.7$ and decisive for small values of δ. Consequently, we must use relation (1) for N_U for describing the behavior of $R_H(\delta)$ in the entire range of variation of δ. Experiments (Fig. 3b) completely confirm this conclusion. It should be noted that the theoretical curves in Fig. 3 do not contain fitting scale parameters. The only fitting parameter, T_0, which only describes the temperature dependence $R_H(T)$, makes it possible to accurately calculate the absolute values of R_H in the entire range of variation of δ and T. The fact that the hole concentration increases with doping level δ in proportion to δ^3 may serve as a sound argument in favor of the existence of diatomic NUCs of this type in $YBa_2Cu_3O_{6+\delta}$ and confirms the proposed mechanism of hole carrier generation in HTSC materials.

2. Fluctuations and origin of the “pseudogap” phase. In our previous publications [1, 2], we proposed that the pseudogap observed in various experiments is nothing but the superconducting gap, formed at a temperature $T > T_c$ as a result of large fluctuations of the number of particles due to electron transitions between the pair level of NUCs and the oxygen band. As a matter of fact, in contrast to traditional superconductors with the electron–phonon interaction, in which the superconducting gap disappears due to thermal excitations above the Fermi surface (which decreases the number of states to which electron pairs can be scattered), the mechanism leading to suppression of the gap in our case is filling of NUCs with real electrons. Consequently, a fluctuation-induced decrease in the population of the pair electron level facilitates the enhancement of the superconducting interaction and may lead to fluctuational “triggering” of superconductivity at $T^* > T > T_{c\infty}$ (here, $T_{c\infty}$ is the equilibrium value of T_c for an infinite NUC cluster). At the same time, a fluctuation-induced increase in the population of the pair level will suppress the superconducting interaction and will lead to fluctuational “suppression” of superconductivity at $T_c < T < T_{c\infty}$. Large fluctuations in the NUC occupancy, which correspond to a considerable deviation of T^* and T_c from $T_{c\infty}$, are possible in underdoped samples, in which a considerable fraction of NUCs belong to finite clusters. With decreasing doping level, the average size of finite clusters decreases and relative fluctuations in NUC population in these clusters increase (i.e., the value of T^* increases and T_c decreases). At the same time, strong fluctuations are ruled out in an overdoped sample, which can be treated as a single infinitely large conducting cluster. Proceeding from the model proposed here, we can determine the dependences of T^* and T_c on doping level δ for the specific compound $YBa_2Cu_3O_{6+\delta}$. We assume that for $\delta < \delta_c$, when NUCs form finite clusters of various sizes, the sample is a Josephson medium, in which superconductivity in the entire volume is attained due to Josephson coupling between superconducting clusters. The size S of a NUC cluster in the CuO_2 plane is determined by the number of Cu ions in this cluster. The minimal size $S_{\min}$ of a cluster in which the superconductivity of the given type is possible should be set at $S_{\min} = 3$, since superconducting transport in a smaller cluster with $S = 2$ is ruled out.

Let us consider a cluster in a CuO_2 plane, which combines a certain number of NUCs and includes $S \geq 3$ copper ions. Then, in accordance with relation (2), the number of electrons per NUC in a given cluster at temperature T is $N = TS/(T + T_0)$. As a result of fluctuations, the number of electrons per NUC in the given cluster may change by $\pm\sqrt{N} = \pm(TS/(T + T_0))^{1/2}$. The condition for fluctuational triggering (suppression) of superconductivity in the given cluster at temperature $T^*(T_c)$ can be written as $N(T) \pm \sqrt{N(T)} = N_c$, where $N_c = T_{c\infty}S/(T_{c\infty} + T_0)$ is the number of electrons per NUC at the superconducting transition temperature of an infinitely large cluster. Thus, we can write

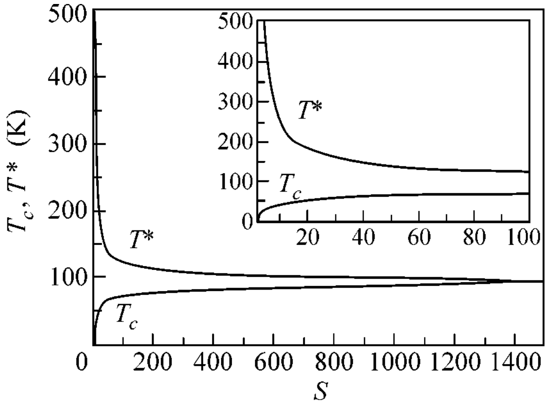

Fig. 4. Temperatures T^* and T_c vs. the cluster size S in the interval $3 < S < 1500$. The inset shows the same dependence in the interval $3 < S < 100$. The 60-K plateau on the $T_c(\delta)$ curve, on which T_c varies from 50 to 70 K, corresponds to an order-of-magnitude change in S (from ~10 to ~100).

$$\begin{aligned} TS/(T + T_0) &\pm (TS/(T + T_0))^{1/2} \\ &= T_{c\infty}S/(T_{c\infty} + T_0), \end{aligned} \tag{4}$$

where the minus and plus signs correspond to $T = T^*$ and $T = T_c$, respectively. Solving Eq. (4) and setting $T_0 = 390$ K and $T_{c\infty} = 92$ K, we obtain T^* and T_c as functions of S (Fig. 4). It can be seen from Fig. 4 that the influence of fluctuations on T_c decreases with increasing cluster size and becomes negligibly small for NUC clusters containing more than 1500 Cu ions, which corresponds to a size of ~150 Å. The so-called 60-K plateau on the $T_c(\delta)$ curve, where T_c varies from 50 to 70 K in the range $0.6 < \delta < 0.8$ corresponds to an order-of-magnitude change in S (from ~10 to ~100). It should be noted that there exists a minimal value of S, for which a cluster at $T \longrightarrow 0$ may remain superconducting all the time in the presence of fluctuations in the NUC occupancy. Since the NUC occupancy at $T = T_{c\infty}$ is $\eta \approx 2/5$, any fluctuation increasing the number of electrons at NUCs by two for a cluster with $S < 5$ will lead to degradation of the superconducting state.

To determine the $T^*(\delta)$ and $T_c(\delta)$ dependences, we must know the NUC percolation threshold as well as the statistics of finite NUC clusters depending on δ. The percolation threshold in NUC clusters for a random distribution of oxygen atoms in chains, as well as the statistics of finite clusters, can be determined using the

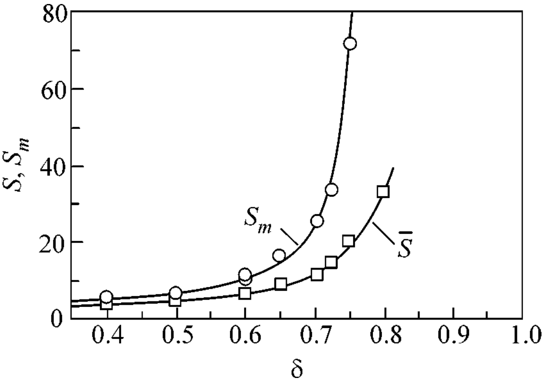

Fig. 5. Mean size S_m of finite NUC clusters and $\bar{S}$ for $YBa_2Cu_3O_{6+\delta}$ vs. the doping level. The open circles and squares are the results of the determination of S_m and $\bar{S}$, respectively, using the Monte Carlo method for a 40 × 40 mesh. The curves are plotted approximately.

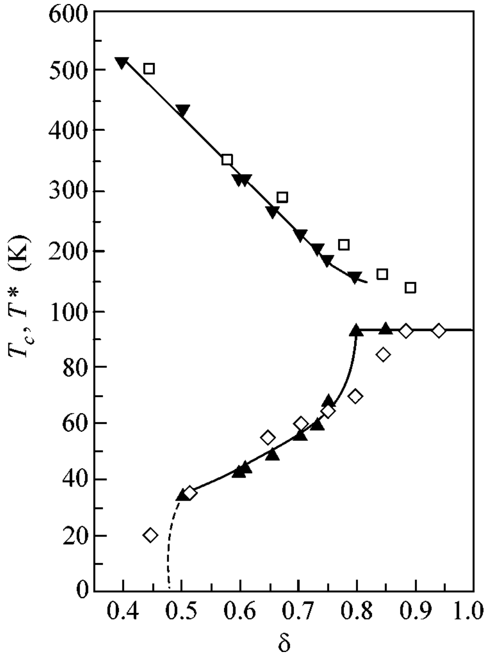

Fig. 6. Temperatures (▼) T^* and (▲) T_c calculated for $YBa_2Cu_3O_{6+\delta}$ vs. the oxygen concentration δ. The squares correspond to the measurements of T^* for single crystals [18], where T^* was determined from the deviation of the temperature dependence $R_{ab}(T)$ of resistance from linearity. The diamonds are the magnetic measurements of T_c for $YBa_2Cu_3O_{6+\delta}$ single crystals [16]. The solid curves are plotted approximately. The dashed part of the $T_c(\delta)$ curve for $\delta < 0.5$ corresponds to the region, where the mean size of the NUC cluster is $\bar{S} < 5$ and fluctuations effectively suppress superconductivity.

Monte Carlo method. In accordance with the proposed mechanism of NUC formation, we assume that (i) each 1D cluster of oxygen ions in a chain, which consists of $N_O \geq 4$ oxygen ions, forms 1D NUC clusters in each CuO_2 plane with a mean size of $S = N_O - 1$ (i.e., containing $N_O - 1$ Cu ions) and (ii) the size of a 2D NUC cluster in a CuO_2 plane is equal to the sum of the sizes of 1D NUC clusters forming it. The value obtained by this method is $\delta_c = 0.80 \pm 0.02$. This means that we should have $T_c = T_{c\infty}$ for $\delta > \delta_c$. However, in experiment T_c reaches the plateau for $x > 0.85$ [15, 16]. We believe that the elevation of the percolation threshold may be due either to the presence of copper vacancies in chains or to repulsion of oxygen atoms from neighboring chains [17], which prevents the grouping of 1D clusters. These factors may lead to elevation of the percolation threshold in NUC clusters as compared to the value expected under the assumption concerning random distribution of oxygen over positions in the chains.

To simplify the derivation of dependences $T^*(\delta)$ and $T_c(\delta)$, we assume that all finite clusters are of the same size equal to a certain mean size of a cluster. The concept of the mean cluster size S_m is used in the percolation theory and is defined as the weighted mean $S_m = \Sigma n_i S_i^2 / \Sigma n_i S_i$. According to the definition, the main contribution to S_m comes from large clusters. It is the quantity $S_m(\delta)$ defined in this way that should be substituted into relation (4) for determining the dependence $T_c(\delta)$ since for T_c we must take the superconducting transition temperature of large clusters with a higher value of T_c, which shunt small clusters and ensuring the main contribution to the conductivity and diamagnetic response. At the same time, to find $T^*(\delta)$, we should rather use the ordinary mean $\bar{S} = \Sigma n_i S_i / \Sigma n_i$, since the contribution to fluctuational “triggering” of superconductivity comes from finite (nonpercolation) clusters. Figure 5 shows our results in determining S_m and $\bar{S}$ for a 40 × 40 mesh by the Monte Carlo method. It can be seen that the value of S_m tends to infinity as we approach the percolation threshold, while the value of $\bar{S}$ remains finite for $\delta \geq \delta_c$ also.

Substituting the obtained values of $S_m(\delta)$ and $\bar{S}(\delta)$ into quadratic equation (4), we obtain dependences $T_c(\delta)$ and $T^*(\delta)$ as solutions to this equation for $YBa_2Cu_3O_{6+\delta}$. Both solutions are shown in Fig. 6 by dark (upright and inverted) triangles. Solid curves are plotted approximately. It follows from the model that the region between these curves is the fluctuation region, in which finite nonpercolation clusters fluctuate between the superconducting and normal states due to fluctuations of the NUC occupancy. The dashed part of the $T_c(\delta)$ for $\delta < 0.5$ corresponds to the region in which the mean NUC cluster size is $\bar{S} < 5$. It was noted above that fluctuations will effectively suppress superconductivity in these clusters. Figure 6 also shows for comparison the results of experiments in which the $T^*(\delta)$ and $T_c(\delta)$ dependences were determined for $YBa_2Cu_3O_{6+\delta}$ single crystals. Light squares represent the results obtained in [18], where the temperature T^* of the emergence of a pseudogap was determined from the deviation of the temperature dependence $R_{ab}(T)$ of resistance from linearity. Light rhombi show the superconducting transition temperature measured for $YBa_2Cu_3O_{6+\delta}$ in [16] using the magnetic method. A comparison of the calculated dependences $T_c(\delta)$ and $T^*(\delta)$ with experimental dependences shows that the agreement is satisfactory in spite of the conditional nature of their determination.

CONCLUSIONS

Thus, our results can be regarded as sound arguments in favor of the HTSC model based on the mechanism of formation of NUCs in this class of compound, which was proposed in [1–3].

We are grateful to S.G. Ovchinnikov for fruitful discussion of the results. This study was supported by the Russian Foundation for Basic Research (project no. 05-02-16706).

REFERENCES

1. K. V. Mitsen and O. M. Ivanenko, Zh. Éksp. Teor. Fiz. **118**, 666 (2000) [JETP **91**, 579 (2000)].
2. K. V. Mitsen and O. M. Ivanenko, Usp. Fiz. Nauk **174**, 545 (2004) [Phys. Usp. **47**, 493 (2004)].
3. K. V. Mitsen and O. M. Ivanenko, JETP **100**, 1082 (2005).
4. E. Simanek, Solid State Commun. **32**, 731 (1979).
5. C. S. Ting, D. N. Talwar, and K. L. Ngai, Phys. Rev. Lett. **45**, 1213 (1980).
6. H.-B. Schuttler, M. Jarrell, and D. J. Scalapino, Phys. Rev. Lett. **58**, 1147 (1987).
7. J. Yu, S. Massida, A. J. Freeman, *et al.*, Phys. Lett. A **122**, 203 (1987).
8. B. A. Volkov and V. V. Tugushev, Pis'ma Zh. Éksp. Teor. Fiz. **46**, 193 (1987) [JETP Lett. **46**, 245 (1987)].
9. G. M. Éliashberg, Pis'ma Zh. Éksp. Teor. Fiz. **46** (Suppl.), 94 (1987) [JETP Lett. **46**, S81 (1987)].
10. I. O. Kulik, Fiz. Nizk. Temp. **13**, 879 (1987) [Sov. J. Low Temp. Phys. **13**, 505 (1987)].
11. P. I. Arseev, Zh. Éksp. Teor. Fiz. **101**, 1246 (1992) [Sov. Phys. JETP **74**, 667 (1992)].
12. J. Ranninger and A. Romano, Phys. Rev. B **66**, 094508 (2002).
13. M. Francois, A. Junod, K. Yvon, *et al.*, Solid State Commun. **66**, 1117 (1988).
14. K. Segawa and Y. Ando, Phys. Rev. B **69**, 104521 (2004).
15. A. J. Jacobson, J. M. Newsam, D. C. Johnston, *et al.*, Phys. Rev. B **39**, 254 (1989).
16. K. Segawa and Y. Ando, Phys. Rev. Lett. **86**, 4907 (2001).
17. R. McCormack, D. de Fontaine, and G. Ceder, Phys. Rev. B **45**, 12 976 (1992).
18. T. Ito, K. Takenaka, and S. Uchida, Phys. Rev. Lett. **70**, 3995 (1993).

Translated by N. Wadhwa

JETP Letters, Vol. 82, No. 3, 2005, pp. 134–138. Translated from Pis'ma v Zhurnal Éksperimental'noĭ i Teoreticheskoĭ Fiziki, Vol. 82, No. 3, 2005, pp. 149–153.
Original Russian Text Copyright © 2005 by Lisin, Shegeda, Zharikov, Lis, Subbotin.

Observation of the Quasidiffusive Propagation of Phonons in Mg_2SiO_4:Ho^{3+} Using Time-Resolved Photo–Phonon Spectroscopy

V. N. Lisin[a], A. M. Shegeda[a], E. V. Zharikov[b], D. A. Lis[b], and K. A. Subbotin[b]

[a] *Zavoĭskiĭ Physicotechnical Institute, Kazan Scientific Center, Russian Academy of Sciences,*
Sibirskiĭ trakt 10/7, Kazan, 420029 Russia
e-mail: vlisin@kfti.knc.ru
[b] *Prokhorov General Physics Institute, Russian Academy of Sciences, Moscow, 119991 Russia*

Received June 21, 2005

The energy flux of phonons produced due to the nonradiative laser-induced transitions of Ho^{3+} impurity ions in forsterite from the $^5F_5$ states has been measured using a superconductor bolometer at a temperature of 2 K. The dependence of the flux on the laser wavelength, the time elapsed after the action of a laser pulse, and the phonon propagation path length is analyzed. It is found that the excitation of Ho^{3+} to some states leads to the diffusive propagation of emitted phonons in the spontaneous frequency decay mode (quasidiffusive mode of propagation): the time of arrival of a phonon pulse is almost a linear function of the path length, but it is several times longer than the longest ballistic time of flight (for transverse phonons). The diffusion coefficient and the nonradiative relaxation time are determined from the best fit to the experiment. © *2005 Pleiades Publishing, Inc.*

PACS numbers: 67.57.Lm, 76.60.–k

It was shown previously [1–3] that the phonon excitation spectra recorded by a bolometer coincide with the absorption spectra of individual ions as well as pairs of nearest neighbors. The time evolution of the phonon excitation spectra carries information on the mechanisms of energy transfer and makes it possible to detect new types of centers. However, the quantitative determination of nonradiative transition time based on this method was not considered and the propagation of emitted phonon was not analyzed. This study is devoted to analysis of information contained in the time dependence of signals on the bolometer for various excitation frequencies and for various distances between an optically excited volume and the bolometer.

The experimental geometry is shown in Fig. 1. A frequency-tuned pulsed dye (oxazine-17) laser was used for optical excitation of Ho^{3+} ions. The pulse duration was 10 ns, the repetition rate was 12.5 Hz, the spectral half-width was 0.1 Å, and the wavelength tuning range was 6300–6700 Å. The sample was a synthetic forsterite crystal grown by the Czochralski method. The doping impurity concentration in the melt was 4.6 wt % Ho_2O_3, 0.16 wt % Na_2O, and 0.19 wt % Al_2O_3. According to our estimates, the actual concentration of holmium in the crystal did not exceed 0.05 wt %. The space symmetry group of forsterite was *Pbnm*. A linearly polarized focused laser beam (beam radius was 0.1 mm) passed through the sample along the *b* axis of the crystal. The electric vector of the light wave was directed parallel to the *a* or *c* axis. The sample thickness along the direction of laser pulse propagation was 7 mm. Phonon pulses produced as a result of passage of laser radiation through the sample were detected by a superconducting In bolometer, which was deposited on the lateral face of the sample. The bolometer shape was a meander 1.3 × 1.3 mm in cross section. The samples

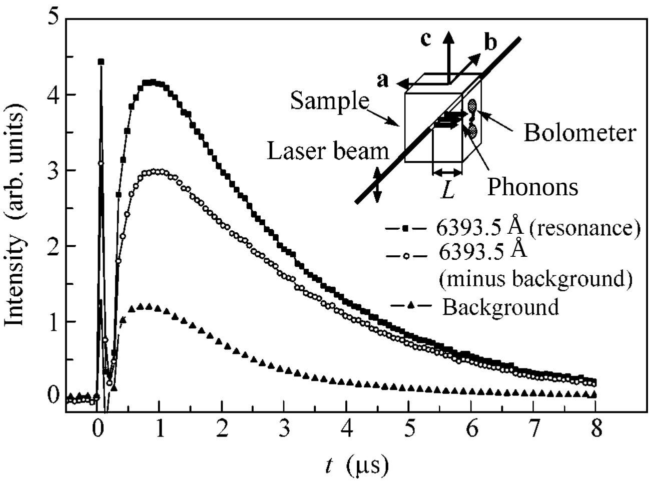

Fig. 1. Typical signal at the bolometer vs. the delay time after the action of a laser pulse on a Mg_2SiO_4:Ho^{3+} sample in the case of resonant and nonresonant excitation (distance *L* between the laser beam and the bolometer is 1 mm). The inset shows the experimental geometry: **a**, **b**, and **c** are the directions of crystallographic axes in forsterite and *L* is the distance between the laser beam and the bolometer.

were in liquid helium at a temperature of 2 K. The working point of the bolometer was set on the lower part of the linear segment of the superconducting transition by applying an external magnetic field. The entire measuring process (signal detection, accumulation, and processing, as well as the measurement of the laser wavelength) was automated. The measuring technique is described in detail in [1–3].

In the case when the sample is excited by a laser pulse, the bolometer detects phonon pulses with a certain time delay depending on the distance between the optically excited region and the bolometer. Figure 1 shows typical signals at the bolometer as a function of time *t* elapsed after the action of a laser pulse. It should be noted that phonons are also produced in the case of nonresonant excitation (background signal), when the laser frequency does not fall in the absorption bands of optical transitions of Ho^{3+} ions. The mechanism of phonon generation by a nonresonant light pulse is not considered here. Since the transmission coefficient for a laser pulse through the sample (Fig. 2) is close to unity (the minimal value is 0.7), the difference between the signal at the bolometer at a given frequency and that measured at the nearest nonresonant frequency represents quite correctly the flux density of phonons emitted by Ho^{3+} ion.

Figure 2 shows the signals at the bolometer as a function of the laser wavelength (phonon excitation spectra) for a fixed (2.5 μs) time delay after the action of a laser pulse. The same figure shows the polarized transmission spectrum of the crystal in the range of transitions to the energy levels of $^5F_5$ of Ho^{3+} ions. The absorption spectrum strongly depends on the orientation of the electric field of the laser relative to the crystallographic axes. The phonon excitation spectra precisely match the absorption spectra of Ho^{3+} ions. In contrast to the Al_2O_3:Cr^{3+} sample [1], the ballistic mode of phonon propagation is not observed in the case of excitation at any absorption line of a Mg_2SiO_4:Ho^{3+} sample. However, for excitation at some lines (e.g., with $\lambda = 6393.5$ Å; see Fig. 3), time t_A corresponding to the emergence at the bolometer of the maximal flux of phonons emitted by Ho^{3+} ions was a nearly linear function of distance *L* from the optically excited region to the bolometer (Fig. 4) as in the absence of diffusion. The "velocity" $L/t_A \approx 0.4$ mm/μs in this case was much smaller than the transverse velocity of sound (v_t = 5 mm/μs) [5], and the shape of the signal was the same as in the case of diffusive propagation. Thus, all distinguishing features of a quasidiffusive mode of phonon propagation are present [6]. Further, we will interpret our experimental data on the basis of the given model (namely, the Kazakovtsev–Levinson scaling model [6, 7]).

Let us briefly recall the basic concepts and conditions for the existence of the quasidiffusive mode of phonon propagation [6, 7]. The model is based on the concept of evolution of the phonon distribution as alternation of generations. Among all decays $\omega \longrightarrow \omega' + \omega''$, event with ω' and ω'' of the same order of magnitude are predominant. Roughly speaking, phonons decay into phonons with half-energy. The initial phonons with energy ω_0 (zeroth generation) decay in time $\tau_N(\omega_0)$ into phonons with $\omega_1 = \omega_0/2$ (first generation); after time $\tau_N(\omega_1)$, phonons ω_1 decay into phonons with ω_2 =

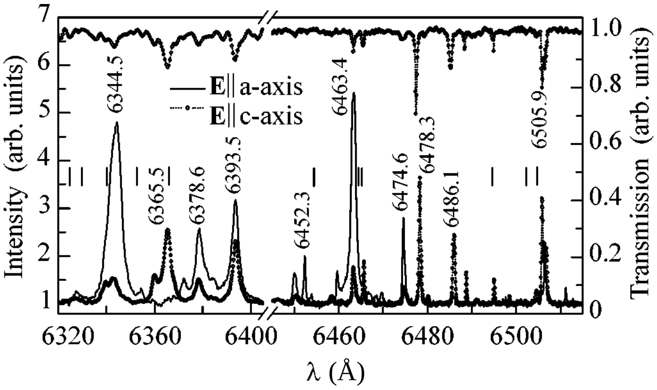

Fig. 2. Phonon excitation spectra in the region of the $^5F_5$ term of the holmium ion for two directions of the electric field of the light wave emitted by a laser relative to the crystallographic axes of forsterite: **E** || **a** and **E** || **c**. The distance *L* between the laser beam and the bolometer is 1.0 mm. The measured transmission spectrum for the **E** || **c** orientation of the electric field of the laser beam is shown in the upper part. The vertical lines show the positions of energy levels belonging to the $^5F_5$ term of the Ho^{3+} ion in forsterite, calculated by Malkin [4]. In the wavelength range missing in the figure, both absorption lines and phonon excitation lines are absent.

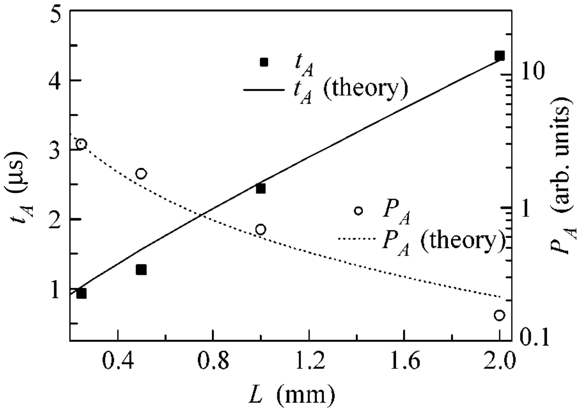

Fig. 3. Time t_A of the appearance of the maximum of the phonon flux emitted by holmium ions at the bolometer and its amplitude vs. the distance in the case of excitation of the 6393.5-Å absorption line. The lines are calculated theoretically.

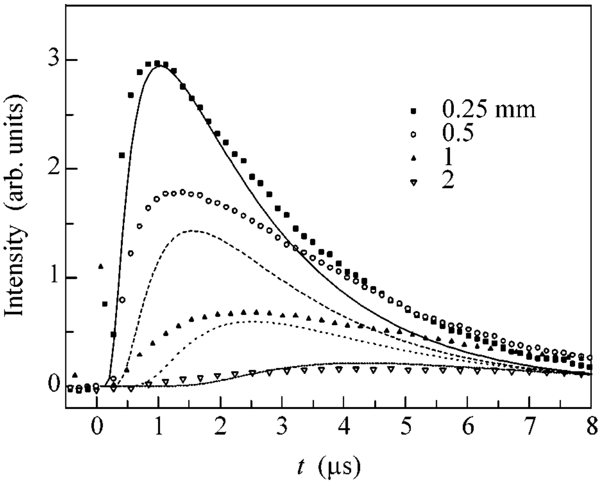

Fig. 4. Bolometer signals vs. the delay time after laser excitation at the 6393.5-Å line at various distances between the laser beam and bolometer. The curves are calculated theoretically using formula (9).

$\omega_1/2 = \omega_0/2^2$ (second generation), and so on. The lifetime of a generation increases rapidly upon a change in generations since

$$\tau_N(\omega) = (A_N\omega^5)^{-1}, \tag{1}$$

where A_N is a parameter determined by the scattering mechanism. Generation ω appears at time $t = \tau_N(\omega_0) + \tau_N(\omega_1) + \ldots + \tau_N(2\omega) \approx \tau_N(2\omega)$ and its lifetime is $\tau_N(\omega) \gg \tau_N(2\omega)$. Phonons with frequency ω exist only during times

$$t \approx \tau_N(\omega). \tag{2}$$

The condition for the existence of the quasidiffusive mode reflects the fact that at least one generation changes over ballistic time of flight $t_B = r/v$, where r is the distance from the point source and v is the velocity, and that phonons of the initial generation propagate diffusely,

$$\tau_i(\omega_0) \ll \tau_N(\omega_0) \ll t_B, \tag{3}$$

where $\tau_i(\omega)$ is the mean free path in the case of elastic scattering of phonons from impurities:

$$\tau_i(\omega) = (A_i\omega^4)^{-1}. \tag{4}$$

Here, A_i is the elastic scattering parameter.

In the description of the experiment, we take into account the fact that relation (2) can also be interpreted as follows [6]: it determines the characteristic frequency of phonons surviving by instant *t*,

$$\omega = (A_N\tau_N)^{-1/5} = (A_N t)^{-1/5}, \tag{5}$$

and, hence, the diffusion coefficient for these phonons:

$$D \simeq \frac{v^2}{3}\tau_i(\omega) = \frac{v^2}{3}(A_i\omega^4)^{-1} = \frac{v^2}{3}\frac{A_N^{4/5}}{A_i}t^{4/5}. \tag{6}$$

During their lifetime, phonons of generation ω propagate in space diffusely over distances on the order of $l(\omega) = (D(\omega)\tau_N(\omega))^{1/2}$. This distance also increases rapidly with a change of generations, as can be seen from relations (1) and (6). Consequently, distance r from a point source, traversed by phonons during time t, is on the order of the diffusion length of the last generation, $r \propto (Dt)^{1/2} \propto t^{9/10}$. Consequently, time t_A of the phonon arrival at a detector located at distance r from the point source depends on r almost linearly: $t_A \propto r^{10/9}$.

The solution of the kinetic equation cannot be obtained even under considerably simplifying assumptions [6]. For this reason, describing the observed signal at the bolometer, we will assume that the diffusion coefficient is constant and take into account its dependence on diffusion time (6) in the final expression. For simplicity, we will use the solution to the diffusion equation for an infinitely large sample with a source. The source is specified by the energy of phonons emitted per unit volume per unit time at instant t_1 after the action of a laser pulse at point (x_1, y_1, z_1) of the optically excited region:

$$\varepsilon\frac{\exp(-t_1/\tau)}{\tau}\exp\left(-\frac{x_1^2+y_1^2}{\pi R^2}\right). \tag{7}$$

Here, τ is the nonradiative relaxation time, R is the beam radius ($R = 0.1$ mm), and ε is a parameter having the dimensions of energy density. It is proportional to the light wave intensity, the laser pulse duration, the light absorption coefficient, and the energy of emitted phonons. Defining the phonon source (7), we assumed that the time dependence of the rate of nonradiative transitions is nonexponential and that the light absorption coefficient is small enough to disregard the dependence on z in (7). We assumed that the laser pulse duration is on the order of 10 ns, which is much smaller than the characteristic times in the given problem. Hence, we can assume that laser excitation occurred at instant $t_1 = 0$. In writing expression (7), we specified the *Z*, *Y*, and *X* axes along the direction of laser beam propagation, along the normal to the surface, and along the bolometer, respectively. Line ($y = L$, $x = 0$) divides the bolometer into two equal parts of width b, where L is the distance from the center of the light beam to the bolometer plane and $2b$ is the bolometer width. The signal at the bolometer is proportional to phonon energy flux density averaged over the area of the bolometer. We can easily show that the energy flux density at point

(x, z) of the bolometer at instant t for phonons emitted in the optically excited volume at time t_1 is

$$p = -D\partial_y E|_{y=L} = \frac{2\varepsilon S_0 DL}{\pi(4D(t-t_1)+R^2)^2} \times \exp\left(-\frac{L^2+x^2}{4D(t-t_1)+R^2}-\frac{t_1}{\tau}\right)\frac{dt_1}{\tau}. \quad (8)$$

Here, $S_0 = \pi R^2$ is the cross-sectional area of the light beam. To derive the final expression describing the signal at the bolometer, it remains for us to integrate expression (8) with respect to t_1 and average over x. Bearing in mind that the time dependence of diffusion coefficient D is described by formula (6) in the quasidiffusive mode of phonon propagation, we pass to integration with respect to diffusion time $t_2 = t - t_1$ instead of integration with respect to emission time, which leads to the following expression for the signal at the bolometer:

$$P = \int_0^t \frac{dt_2}{\tau}\int_0^b \frac{dx}{b}\frac{2\varepsilon S_0 DL}{\pi(4Dt_2+R^2)^2} \times \exp\left(-\frac{L^2+x^2}{4Dt_2+R^2}-\frac{t-t_2}{\tau}\right). \quad (9)$$

We now assume that the diffusion coefficient in the integrand is a function of time and this dependence is given by relation (6). Let us determine from Eq. (9) the maximal value of the signal at the bolometer for a given distance L in terms of P_A and the time of emergence of the peak in terms of t_A using the relations

$$P_A = \max(P(t)), \quad P(t_A) = P_A. \quad (10)$$

Solid curves in Fig. 3 show the dependences of t_A and P_A on L. The best agreement with experiment is attained at the following values of parameters:

$$\tau = 1.8~\mu\text{s}, \quad \frac{v^2}{3}\frac{A_N^{4/5}}{A_i} = 0.12~\text{mm}^2/\mu\text{s}^{9/5}. \quad (11)$$

Solid curves in Fig. 4 show the theoretical dependence (9) (taking into account parameters (11)) of the flux of phonons emitted by holmium ions and detected by the bolometer on the time delay t for various distances L from the optically excited region to the bolometer. It can be seen that the theoretical curves correctly describe the experimental data. Substituting the experimentally obtained values of t_A into formula (6) and taking into account parameters (11), we obtain the following values of diffusion coefficient $D(t_A)$ (in mm^2/μs) and of L (in mm): 1.14, 1.46, 2.46, and 3.91 and 0.25, 0.5, 1, and 2, respectively. It should be noted that these values of the diffusion coefficient coincide in order of magnitude with empirical values of $D = 1.2$ and 2.4 for $L = 1$ and 2 (in the same units), which were obtained in [8] for an Al_2O_3:V sample. In [8], the quasidiffusive mode of phonon propagation was directly observed in experiments for the first time.

Let us estimate the values of scattering parameters A_i and A_N and then verify the validity of conditions (3) of the existence of quasidiffusive mode of phonon propagation; after this, we will compare the calculated ratio of the parameters with the experimentally obtained value (11).

The Ho^{3+} impurity ions differ from Mg^{2+} substitutional ions in the mass, charge, and ionic radius. Let us estimate the value of A_i from below, taking into account phonon scattering from impurities only due to the difference in the masses of the Ho^{3+} and Mg^{2+} ions and disregarding scattering due to the difference in the force constants and ionic volumes and due to the fact that Ho^{3+} ions may form dimer centers in forsterite [9]. Using the expression for the isotopic scattering rate derived in [10] and refined in [11], we can easily find that

$$A_i \ge \frac{\mho}{4\pi v^3}\frac{mc(1-c)(A_x-A_y)^2}{(m((1-c)A_x+cA_y)+A_z)^2}, \quad (12)$$

where $v^{-3} = (v_l^{-3} + v_t^{-3})/3$, $\mho$ is the unit cell volume, and v_l and v_t are the longitudinal and transverse velocities of sound, respectively; X and Y denote the substitutional atoms and impurity atoms, and A_x is the atomic weight of element X in a crystal with a formula unit $(X_{1-c}Y_c)_m Z$. In our case, $c \le 5 \times 10^{-4}$, $A_{Mg}/A_{Ho} = 7.4 \times 10^{-5}$. Assuming that [5] $v_l = 8.589 \times 10^5$, $v_t = 5.018 \times 10^5$, and $\mho = 290 \times 10^{-24}$ (in CGS units), we obtain $\tau_i^{-1} \ge 0.8 \times 10^{-44}\omega^4$ for $c = 3 \times 10^{-5}$. We take into account the fact that the absorption line $\lambda = 6393.5$ Å is separated from the nearest lower line on the energy scale by 136.6 cm^{-1} (see Fig. 2). Consequently, the frequency of the emitted zeroth-generation phonons is $\nu_0 = \omega_0/2\pi \ge 136.7$ cm^{-1} and $\tau_i \le 2.8 \times 10^{-4}$ μs.

The most accurate expression for the phonon spontaneous decay rate τ_N^{-1}, which is suitable for quantitative comparison, is given in [12]. However, third-order elastic constants for forsterite are unknown; for this reason, we express A_N in terms of the Grüneisen constant using the results obtained in [13]:

$$A_N \le \frac{\hbar\gamma^2}{144\pi\rho v_l^2 v_t^3}. \quad (13)$$

Here, ρ is the crystal density and γ is the Grüneisen constant. The inequality sign takes into account the fact that estimate (13) of the inelastic scattering constant based on the Grüneisen constant leads [12] to an exaggerated value of the phonon spontaneous decay rate. Setting $\rho = 3.221$ g/cm^3 [5] and $\gamma = \gamma_{LA} = 1.22$ [14], we obtain $\tau_N^{-1} \leq 1.1 \times 10^{-59}\omega^5$. For values of $\nu = \omega/2\pi$ = 136.7 cm^{-1} = 4.1 THz, we have $\tau_N \geq 8.3 \times 10^{-3}$ μs. It follows that the left-hand side of inequality (3) is satisfied with a large margin, which is [15] a necessary condition for the applicability of the Kazakovtsev–Levinson scaling model [6, 7] of the quasidiffusive mode of phonon propagation.

The minimal ballistic time of flight $t_B \simeq 0.25\ \text{mm}/v_l$ = 0.29 μs is much longer than the time of inelastic scattering of phonons; consequently, the right-hand side of the inequality also holds. This is facilitated by the high value of energy of emitted phonons, which exceeds the anharmonic decay rate. It becomes clear why emitted phonons propagate in the quasidiffusive mode when the given line (λ = 6393.5 Å) is excited.

Finally, the value of quantity $(v^2/3)A_N^{4/5}/A_i$ = $(v^2/3)\tau_i/\tau_N^{4/5} \leq 0.14\ \text{mm}^2/\mu\text{s}^{9/5}$ calculated for the above values of parameters does not contradict the experimental values (11).

Thus, the time-resolved photo-phonon spectroscopy is not only a very sensitive method for detecting optical transition frequencies but also provides additional information on phonon propagation and nonradiative relaxation times.

We are grateful to S.A. Basun for fruitful discussions, V.F. Tarasov for his interest in this research, and N.K. Solovarov for valuable remarks after reading the manuscript. This study was supported by the Division of Physical Sciences, Russian Academy of Sciences (programs “Optical Spectroscopy and Frequency Standards” and “Coherent Acoustic Fields and Signals”); the International Science and Technology Center (grant no. 2121); and the Russian Foundation for Basic Research (project no. 03-02-16374).

REFERENCES

1. A. M. Shegeda and V. N. Lisin, Pis’ma Zh. Éksp. Teor. Fiz. **78**, 1247 (2003) [JETP Lett. **78**, 730 (2003)]; cond-mat/0309180 (2003).
2. A. M. Shegeda and V. N. Lisin, *2002 Yearbook of Zavoĭskiĭ Physicotechnical Institute* (FiztekhPress, Kazan, 2003), p. 111 [in Russian].
3. A. M. Shegeda and V. N. Lisin, *2003 Yearbook of Zavoĭskiĭ Physicotechnical Institute* (FiztekhPress, Kazan, 2004), p. 103 [in Russian].
4. A. M. Shegeda, V. N. Lisin, B. Z. Malkin, *et al.*, in *Abstract and Program of XII Feofilov Symposium on Spectroscopy of Crystals Activated by Rare Earth and Transition Metal Ions* (Ural State Technical Univ., Yekaterinburg, 2004).
5. A. M. Hofmjeister, Am. Mineral. **86**, 1188 (2001).
6. D. V. Kazakovtsev and I. B. Levinson, Pis’ma Zh. Éksp. Teor. Fiz. **27**, 194 (1978) [JETP Lett. **27**, 181 (1978)].
7. D. V. Kazakovtsev and Y. B. Levinson, Phys. Status Solidi B **96**, 117 (1979).
8. W. E. Bron, Y. B. Levinson, and J. M. O’Connor, Phys. Rev. Lett. **49**, 209 (1982).
9. A. V. Gaĭster, E. V. Zharikov, A. A. Konovalov, *et al.*, Pis’ma Zh. Éksp. Teor. Fiz. **77**, 753 (2003) [JETP Lett. **77**, 625 (2003)].
10. Shin-ichiro Tamura, Phys. Rev. B **30**, 610 (1984).
11. D. V. Kazakovtsev and Y. B. Levinson, Phys. Status Solidi B **136**, 425 (1986).
12. Shin-ichiro Tamura, Phys. Rev. B **31**, 2574 (1985).
13. R. Baumgartner, M. Engelhardt, and K. F. Renk, Phys. Rev. Lett. **47**, 1403 (1981).
14. Anne M. Hofmjeister and Ho-kwang Mao, Proc. Natl. Acad. Sci. USA **99**, 559 (2002).
15. H. J. Maris, Phys. Rev. B **41**, 9736 (1990).

Translated by N. Wadhwa

JETP Letters, Vol. 82, No. 3, 2005, pp. 139–144. Translated from Pis'ma v Zhurnal Éksperimental'noĭ i Teoreticheskoĭ Fiziki, Vol. 82, No. 3, 2005, pp. 154–160.
Original Russian Text Copyright © 2005 by Verkhovskiĭ, Arkhipov, Zuev, Piskunov, Mikhalev, Korolev, Svyatov, Pogudin, Ogloblichev, Buzlukov.

Features of the Magnetic State of *f* Electrons in the Stabilized δ Phase of the $Pu_{0.95}Ga_{0.05}$ Alloy

S. V. Verkhovskiĭ[a], V. E. Arkhipov[a], Yu. N. Zuev[b], Yu. V. Piskunov[a],
K. N. Mikhalev[a], A. V. Korolev[a], I. L. Svyatov[b], A. V. Pogudin[a],
V. V. Ogloblichev[a], and A. L. Buzlukov[a]

[a] *Institute of Metal Physics, Ural Division, Russian Academy of Sciences, Yekaterinburg, 620041 Russia*
e-mail: verkhovskii@imp.uran.ru
[b] *Russian Federal Nuclear Center Institute of Technical Physics, Snezhinsk, Russia*

Received June 27, 2005

For the $Pu_{0.95}Ga_{0.05}$ alloy belonging to the stabilized δ phase of the Pu–Ga system, the ^{69}Ga NMR spectra are measured in the temperature interval 10–650 K and the static magnetic susceptibility χ is measured in the interval T = 20–350 K. In the region $T > T^*$ = 235 K, the temperature-dependent magnetic part of the shift $K(T)$ of the Ga NMR line reproduces the $\chi(T)$ dependence and follows the Curie–Weiss law $K(T) \sim (T + \Theta)^{-1}$ with Θ = 280(40) K, which is typical of incoherent spin fluctuations of localized *f* electrons in concentrated nonmagnetic Kondo systems. The estimate of the effective magnetic moment $\mu_{\text{eff, }5f}(g_e = 2) = 0.15(5)\mu_B$ per Pu atom testifies to a strong suppression of the spin magnetism in the alloy, where the configuration of the *f* shell of a Pu ion is close to atomic-like f^6. The difference between the $K(T)$ and $\chi(T)$ dependences observed for the alloy in the temperature range $T < T^*$ is analyzed in terms of the two-fluid description of Kondo lattices developed by Pines *et al.* [15, 16] in application to the coherent state of a heavy-fermion liquid. Possible causes for the anomalous increase in long-wave contributions in the spatial dispersion of the localized spin susceptibility component of *f* electrons χ_{ff} at temperatures below 50 K are discussed. © *2005 Pleiades Publishing, Inc.*

PACS numbers: 71.27.1a, 75.30.Cr, 75.40.Gb, 76.60.2k

The electronic properties of plutonium and Pu-based alloys had been studied for years because of the specific role of these materials in modern technologies and in the fundamental physics of actinides. In the actinide series, Pu lies between Np, which is characterized by a pronounced band character of 5*f* electrons, and Am characterized by a long-range magnetic order [1, 2]. The rich phase diagram of plutonium [3] with six sequential polymorphic transformations and the unique transport and magnetic properties of this material are largely caused by the changes in the degree of localization of 5*f* electrons in different structure states of Pu.

Today, the problem attracting considerable interest is concerned with the ground state of the 5*f* electron system in δ-Pu and stabilized δ phase alloys (the fcc structure). The large electron contribution to specific heat [4], the high resistivity $\rho(T)$, and its nonmonotonic temperature dependence with a maximum below 200 K [5] are the characteristic macroproperties of δ-Pu that make this material close to heavy-fermion systems with a strong localization of *f* electrons [6].

The temperature dependence of magnetic susceptibility $\chi(T)$ of the stabilized δ phase ($Pu_{0.94}Ga_{0.06}$, $Pu_{0.94}Al_{0.06}$ alloys [5]) is also nonmonotonic. At high temperatures, $\chi(T)$ follows the modified Curie–Weiss law, which, according to [5], testifies to the localization of *f* electrons with an effective magnetic moment $\mu_{\text{eff}} = 1.2\mu_B$ in the alloy. On cooling, $\chi(T)$ passes through a weakly pronounced maximum in the same temperature range 100–150 K as that observed for the maximum of $\rho(T)$. The presence of the maximum in $\chi(T)$ was explained by the effect of Kondo compensation of the magnetic moments of localized *f* electrons by the charge carriers in the low-temperature region. According to the estimates given in [5], the weak $\chi(T)$ dependence is determined by the fact that the dominant contribution to the magnetic susceptibility of δ-Pu is made by the temperature-independent Van Vleck paramagnetism of the partially filled 5*f* band of plutonium. This interpretation of the nature of the $\chi(T)$ dependence and the corresponding high estimates of the static magnetism of *f* electrons in Pu was recently reconsidered [7] in view of the fact that such weak variations of magnetic susceptibility with temperature, namely, $\{\chi(150\text{ K}) - \chi(600\text{ K})\} \sim 0.05\chi(150\text{ K})$, may also be caused by other factors. One of them is the temperature dependence of the Pauli contribution of electron states in the conduction band of δ-Pu, because, according to electron photoemission data [8], the spectral density of states $g(E)$ has a narrow peak of width ~700 K near E_F. However, it should be noted that the single-particle nature of this $g(E)$ anomaly is not confirmed by theoretical calculations of the band structure of δ-Pu [9].

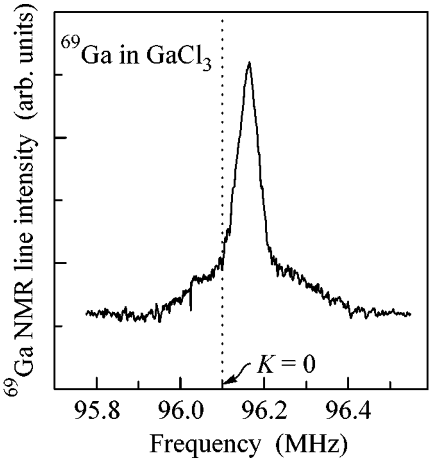

Fig. 1. ^{69}Ga NMR spectrum obtained for the $Pu_{0.95}Ga_{0.05}$ alloy at $T = 20$ K.

Additional difficulties in analyzing the weak temperature dependence of χ may be caused by the low-temperature magnetic instability that accompanies the radiation aging of δ-Pu [10] and that is possibly related to the quantum instability of the electron configuration of Pu in the ground state of the δ phase. For δ-Pu, a delicate balance between the spin–orbit and exchange interactions takes place for the electrons of the *f* shell of the actinide and, hence, small variations (~15%) of the exchange integral determine the magnetic or nonmagnetic realization of the ground state of *f* electrons in the alloy [9].

In connection with this, local neutron scattering and NMR techniques are preferable for studying the emergence of the electron instability and its development with temperature in the stabilized δ-phase plutonium alloys. From ^{27}Al [11] and ^{69,71}Ga [11–13] NMR studies, it was found that the NMR line shift (K) and the nuclear spin–lattice relaxation rate are determined by the local magnetic fields that arise at the NMR probe nucleus due to the spin polarization transferred from the *f* electron shells of the neighboring actinide atoms. Thus, the temperature variation of the gallium NMR line shift K reflects the evolution of the spin contributions of different origin to the magnetic susceptibility. In particular, for the $Pu_{0.95}Ga_{0.05}$ alloy, the temperature dependence of the gallium line shift $^{69}K(T)$ was found to be nonmonotonic with a maximum at $T \sim 150$ K [13]. Its temperature-reversible behavior testifies that, as the temperature decreases, the electron spectrum of the δ phase develops an instability, which is accompanied by a decrease in the spin contributions to the susceptibility of the alloy at $T < 150$ K. However, the NMR data obtained in the limited temperature interval 5–350 K were insufficient to study the state of the electronic system in the high-temperature region.

In this paper, we present the results of measuring the temperature dependence of the ^{69}Ga NMR line shift in a wide temperature range of the δ phase state of the $Pu_{0.95}Ga_{0.05}$ alloy. These measurements allow us to estimate the contribution of the spin magnetism of *f* electrons to the static magnetic susceptibility of the alloy and to clarify the situation with their localization in the high-temperature region of existence of δ-Pu. We also present a combined analysis of the NMR and static susceptibility data obtained from bulk samples with identical thermal histories. The difference between the temperature dependences of the Knight shift $^{69}K_s(T)$ and magnetic susceptibility $\chi(T)$ is discussed in terms of the two-fluid description of heavy-fermion systems proposed in [14] for the region of the emergence and development of the coherent state and developed for NMR applications in [15].

The samples had the form of isolated plates (15 × 2.5 × 0.2 mm) for NMR experiments and a parallelepiped (8 × 2.5 × 2.5 mm) for magnetic susceptibility measurements. They were cut out from a $Pu_{0.95}Ga_{0.05}$ alloy ingot. The surfaces of the samples were mechanically polished and then chemically etched to remove the surface impurities and the oxide layer caused by the mechanical treatment. The samples were then homogenized in argon at 450°C for several hours. After cooling, they were placed in glass containers filled with spectroscopically pure argon and sealed. The static susceptibility was measured by an MPMS-XL-5 SQUID magnetometer (Quantum Design) in the temperature interval $T = 20$–350 K in magnetic field $H = 10$ kOe.

The ^{69}Ga NMR spectra ($I = 3/2$) were measured for the interval $T = 20$–650 K in a magnetic field of 94 kOe by a pulsed phase-coherent NMR spectrometer with a quadrature system of signal detection. The spin echo signal was recorded. The spectral intensity of the NMR signal corresponding to the central transition ($m_I = -1/2 \longleftrightarrow +1/2$) was obtained as a result of the subsequent complex Fourier transformation of the second half of the echo signal. In measuring the ^{69}Ga NMR spectrum (Fig. 1) that included all $2I$ transitions and far exceeded the bandwidth of frequencies excited by the radio pulse, we used the summation of the Fourier signal data array gathered over different equally spaced frequencies of the spectrometer. The line shifts for the alloy sample were determined with respect to the position of the peak of the ^{69}Ga NMR line in GaCl$_3$.

In the measurements carried out below 40 K, we took into account the effects of radio-frequency and radiation-stimulated heating of the alloy sample, which was placed in the sealed container and had a limited thermal contact with the thermostat of the cryostat. To take into account these effects, we measured the magnetization of gallium nuclei in thermodynamic equilibrium. This magnetization follows the Curie law in the temperature interval of interest: $M_0 \sim T^{-1}$, where T is the true temperature of the sample. By changing the number of radio pulses of a fixed duration, we varied the power multiplicity of the source of radio-frequency heating. This allowed us to estimate the thermal effect of the source of the radiation-stimulated sample heating. The data presented below for the temperature dependence of the NMR line shift $^{69}K(T)$ correspond to the true temperature of the sample plates with a relative error $\Delta T/T \leq 0.02$.

The temperature dependence of the static magnetic susceptibility of the $Pu_{0.95}Ga_{0.05}$ (□) alloy is shown in Fig. 2a. At room temperature, its value is 4.7×10^{-4} cm^3/mol, which is approximately 10% smaller than the value $\chi(300\ K) = 5.3 \times 10^{-4}$ cm^3/mol reported in [5] for the $Pu_{0.94}Ga_{0.06}$ δ-phase alloy of a close composition. The difference in the absolute values of the susceptibilities of alloys is insignificant and mainly determined by the error in the determination of the mass of the sample ($\Delta m/m \sim 0.05$ in our case). The difference in the temperature dependences of the susceptibilities of alloys is more significant below 200 K. Unlike the $\chi(T)$ curve observed for $Pu_{0.94}Ga_{0.06}$ with a maximum within 100–150 K [5] (see Fig. 2 in [5]), the $Pu_{0.95}Ga_{0.05}$ alloy under study exhibits a monotonic increase in χ with a tendency to a maximum in the low-temperature region $T < 50$ K. To verify that the measured $\chi(T)$ dependence is governed by the bulk properties of the alloy, a similar temperature dependence of magnetic susceptibility was obtained as a result of additional measurements on the same sample with its linear dimensions being reduced by one third by electrochemical etching.

The ^{69}Ga NMR spectrum (Fig. 1) consists of a single central line (the $m_I = -1/2 \longleftrightarrow +1/2$ transition) rising above a base formed by satellite lines ($m_I = \pm 1/2 \longleftrightarrow \pm 3/2$). Such a spectrum is typical of a powder of imperfect cubic crystals [16] with local cubic symmetry distortions in the charge environment of the resonant Ga nucleus, which possesses an electric quadrupole moment. The temperature dependence of the shift $^{69}K(T)$ that is presented in Fig. 2b completely reproduces the data previously obtained for the temperature range below room temperature [13], provided that the previous data array is additionally displaced by 150 ppm with allowance for the results of the more definite procedure of determining the zero shift by the NMR signal from the reference sample in the given experiment.

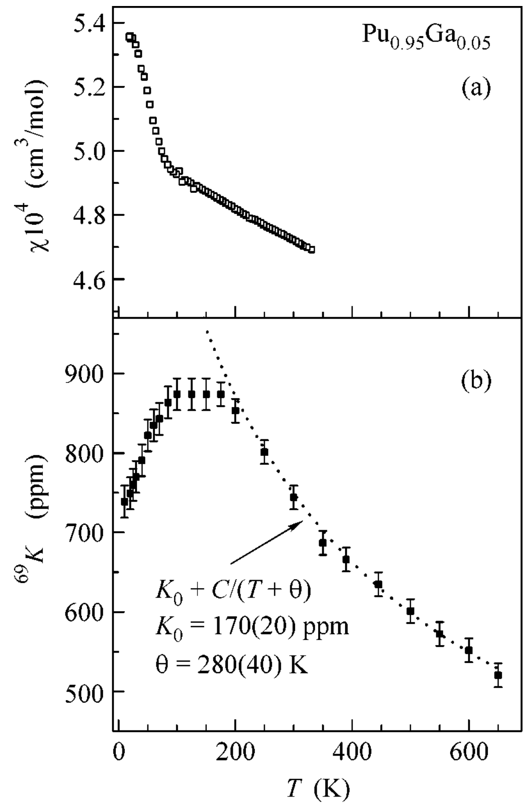

Fig. 2. Temperature dependences of (a) the static magnetic susceptibility χ and (b) the ^{69}Ga NMR line shift ^{69}K for $Pu_{0.95}Ga_{0.05}$.

For the region $T > 200$ K, the behavior of the line shift in the δ-Pu alloy is adequately described by a dependence in the form of the Curie–Weiss law $K(T) = K_0 + C/(T + \Theta)$ with the parameters $K_0 = 170(20)$ ppm and $\Theta = 280(20)$ K (the dotted line in Fig. 2b). A similar temperature dependence is observed for the NMR line shift of nonmagnetic ions in heavy-fermion systems above the region where the coherent state of the heavy-fermion fluid is formed and where the state of the electron system of f ions is adequately described in the framework of the model of a gas consisting of noninteracting Kondo centers with a local spin susceptibility $\chi_{s,ff}(T) \sim (T + \Theta)^{-1}$. In the case of the stabilized δ-Pu alloy showing an electron system state close to heavy-fermion one, the isotropic Ga NMR line shift should be mainly determined by the Knight shift $^{69}K_s$ due to the hyperfine interactions of the nuclear spin I with its electron environment. The contact Fermi interaction with the electrons of the conduction band $\gamma\hbar A\mathbf{I}\mathbf{S}^c$ forms a temperature-independent contribution $K_{s,0}$.[1] The effect of the uniform spin polarization of conduction electrons by indirect electron–nucleus interactions $\gamma\hbar\mathbf{I}(r_i) \cdot \mathbf{B} \cdot \mathbf{S}^f(r_j)$ with stronger localized spins of f electrons is taken into account in the form of an additive contribution K_f to the total Knight shift:

$$^{69}K_s(T) = K_{s,0} + K_f(T) = A\chi_{s,c} + B\chi_{s,5f}(T)/N_A, \quad (1)$$

where the constant B is assumed to be isotropic and has a physical meaning of the effective hyperfine field produced at the Ga nucleus by the $5f$ electrons of the 12

---

[1] Note that a scalar form is characteristic of not only the contact contribution to the shift but also of the core polarization contribution K_{cp}, which determines the isotropic part of the shift of transition metal atoms with the orbital composition of electron states characterized by $l \neq 0$ near E_F. However, for the nontransition element Ga, the dominant contribution should be that of the contact interaction of the nucleus with the electrons of the conduction band in the orbital state $l = 0$.

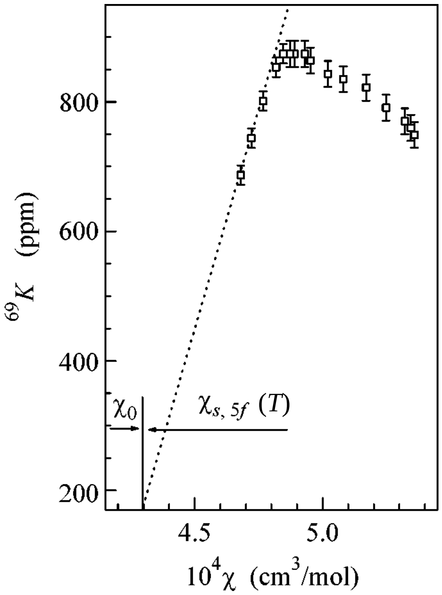

Fig. 3. Parametric dependence $^{69}K(\chi)$ and the results of separating the contributions to the spin susceptibility of the $Pu_{0.95}Ga_{0.05}$ alloy. The dotted line shows the linear approximation of the ^{69}K increase in the region $T = 200$–350 K.

nearest Pu atoms in the fcc structure of δ-Pu, N_A is the Avogadro number, and $\chi_{s,5f} = N_A\chi_{ff}$ is the molar spin susceptibility of 5*f* electrons of Pu in the alloy.

Thus, for the high-temperature region, one should expect that the Knight shift is $^{69}K(T) \sim \chi_{s,5f}(T)$. Indeed, the linear shift increase portion observed in the parametric dependence $K(\chi)$ (Fig. 3) testifies in favor of the applicability of Eq. (1) to describing the spin magnetism of 5*f* electrons of the alloy above 200 K. The extrapolation to $T \longrightarrow \infty$ of the linear portion of $K(\chi)$ allows us to separate the temperature-dependent contribution $\chi_{s,5f}$, whose value ~0.08(1)χ corresponds to the effective spin magnetic moment of the *f* shell of a Pu atom in the alloy: $\mu_{\text{eff},5f}(g_e = 2) = 0.15(5)\mu_B$. From the estimate obtained for $\chi_{s,5f}$, it follows that, in the region $T > 200$ K, the dominant contribution to χ is determined by the orbital state of *f* electrons in the alloy. The anomalously small estimate of $\mu_{\text{eff},5f}$ suggests that the configuration of the *f* shell of Pu in the δ phase is close to atomic-like configuration $f^6(S = 0;\ L = 0)$ [9] and that the Van Vleck orbital contribution determines the static magnetism of δ-Pu.

In the temperature range below $T^* \sim 200$ K, the similarity of the temperature dependences $K(T)$ and $\chi(T)$ fails. Such a difference in the low-temperature region is observed for heavy-fermion compounds. It is often ascribed to the splitting (Δ_{CF}) of the multiplet structure of *f* ion levels, which leads to a change in the populations of lower multiplets at $T \sim \Delta_{CF} < T^*$ and to a corresponding variation of H_f at the formation of the coherent state.

In [14], it was shown that, for heavy-fermion systems, the energy scale T^* is of a multiparticle character and is determined by the intensity of interaction between Kondo centers. According to the proposed two-fluid description of concentrated Kondo lattices, at temperatures $T < T^*$, the system of localized *f* electrons ($\mathbf{S}^f(r_i)$) and conduction electrons ($\mathbf{S}^c(r_i)$) with a total spin $S = \Sigma_i\mathbf{S}^f(r_i) + \Sigma_i \cdot \mathbf{S}^c(r_i)$ acquires an additional spin component associated with the coherent behavior of *f* electrons. The development of the coherent state of the heavy-fermion liquid with temperature is characterized by the spin correlation function $\langle\mathbf{S}^f(r_i)\mathbf{S}^c(r_i)\rangle$. Below T^*, the expression for the spin susceptibility of *f* electrons $\chi_{s,5f}(T)$ contains both the contribution of isolated Kondo centers $\chi_{ff}(T) = (1/N)\Sigma_{i,j} \cdot \langle\mathbf{S}^f(r_i)\mathbf{S}^f(r_j)\rangle$ and the heavy-fermion contribution from the polarization of the conduction-electron spin system that is correlated by the spin component of *f* electrons $\chi_{cf}(T) = (1/N)\Sigma_{i,j} \cdot \langle\mathbf{S}^f(r_i)\mathbf{S}^c(r_j)\rangle$:

$$\chi_{s,5f}(T) = \chi_{ff}(T) + 2\chi_{cf}(T). \tag{2}$$

In this case, expression (1) for the isotropic Knight shift $^{69}K_s$ is complemented by the contribution $K_{cf} \sim \chi_{cf}$:

$$\begin{aligned} {}^{69}K_s(T) &= K_{s,0} + K_{cf}(T) + K_f(T) \\ &= K_{s,0} + A\chi_{cf}(T) + B\chi_{cf}(T) + \chi_{ff}(T) \\ &= K_{s,0} + (A+B)\chi_{cf}(T) + B\chi_{ff}(T). \end{aligned} \tag{3}$$

This expression takes into account the significant changes in the mechanism of the spin polarization transfer from *f* electrons to Ga nuclei [15]. The contribution of the contact interaction to the Knight shift is mainly determined by the spectral weight of the heavy-fermion component: $A\langle\mathbf{S}^c\rangle_{q=0} \approx \chi_{cf}H_0$. With the decrease in the spectral weight of the localized *f* component at $q = 0$, the corresponding contribution of the indirect interaction also varies: $B\langle\mathbf{S}^f\rangle_{q=0} = (\chi_{cf} + \chi_{ff})H_0$. The constants *A* and *B* determine the intensity of the contact and indirect hyperfine interactions of the Ga nucleus, respectively, with heavy-fermion delocalized and localized spin components of the *f*-electron system of the alloy.

A combined analysis of the data on the Knight shift $^{69}K(T)$ and the static magnetic susceptibility $\chi_{s,5f}(T)$ with the use of Eqs. (2) and (3) allows us to trace the temperature variation of the heavy-fermion contribution to the Knight shift K_{cf}:

$$\begin{aligned} K_{cf}(T) &= {}^{69}K(T) - B\chi_{s,5f}(T) - K_{s,0} \\ &= (A-B)\chi_{cf}(T). \end{aligned} \tag{4}$$

As the temperature decreases, the heavy-fermion component of the shift (Fig. 4a) increases in its absolute value with a tendency to flatten out at $K_{cf} \sim -800$ ppm below 30 K. The two-fluid model predicts that, below T^*, the behavior of the heavy-fermion component of spin susceptibility follows the universal dependence $\chi_{cf}(T) \sim (1 - T/T^*)\log(T/T^*)$, where the factor $(1 - T/T^*)$ determines the fraction of the heavy-fermion component of f electrons. The corresponding dependence for the heavy-fermion contribution to the shift has the form $K_{cf}(T) = K_{cf}(0)\{(1 - T/T^*)\log(T/T^*)\}$ and is shown in Fig. 4 by the dotted line. With the parameter values $K_{cf}(0) = -950(80)$ ppm and $T^* = 235(40)$ K, the curve completely reproduces, over a wide temperature range, the results obtained by analyzing $K_{cf}(T)$ with the use of experimental data on the Knight shift and the static magnetic susceptibility presented in Fig. 1.

For $T < T^*$, the contribution to the total shift of the local spin component $K_{ff}(T)$ can be determined using Eqs. (3) and (4) with a known value of the ratio between the hyperfine constants B/A. The results of the reconstruction of the $K_{ff}(T)$ dependence are presented in Fig. 4b for $B/A = 0.11$. The indirect interaction constant $B = 66(6)$ kOe/μ_B is determined by the slope of the linearly ascending portion of the parametric dependence $K(\chi)$ shown in Fig. 3. As the estimate of the constant A, we used the value of the effective hyperfine field produced at the nucleus by an unpaired 4s electron: $A(4s) = 580$ kOe/μ_B [13, 16]. The dotted line in Fig. 4b corresponds to the temperature dependence of the contribution made to the shift by the local spin f component $B\chi_{ff}(T) \sim (T + T^*)^{-1}$ with $T^* = 235$ K. One can see that, up to $T \sim 50$ K, the increase in $K_f(T) \sim (T + 235\text{ K})^{-1}$ occurs in good agreement with the behavior expected according to [14, 15] for the spin susceptibility $\chi_{ff}(T)$ in the region of the formation of the coherent heavy-fermion state.

Earlier, in the pioneering study [15], a behavior of $K_{cf}(T)$ analogous to that shown in Fig. 4a for the $Pu_{0.95}Ga_{0.05}$ alloy was revealed for a great number of 4f(5f) compounds with heavy fermions. Thus, the previous statement [13] concerning the instability of the electron spectrum of the δ phase in the low-frequency region can be formulated in more detail. In the system of interacting f electrons of Pu in the δ-phase $Pu_{0.95}Ga_{0.05}$ alloy, a coherent state of the heavy-fermion liquid is formed below T^*. This is accompanied by the increase in the spectral weight of long-wave low-energy spin fluctuations of f electrons in the alloy, which describe the delocalized (Fermi-liquid) behavior of f electrons in the alloy, at the expense of the decrease in the weight of short-wave fluctuations of the almost localized f-electron state at high temperatures.

As the temperature decreases further, the behaviors of the local K_{ff} and Fermi liquid K_{cf} contributions to the shift deviate from the dependences predicted by the two-fluid model. The tendency of $K_{cf}(T)$ to flatten out below 30 K may testify to the termination of the formation of the heavy-fermion spin component of f electrons. However, the final conclusion about the behavior of K_{cf} in the low-temperature region depends on the understanding of the origin of the additional increase exhibited by the uniform contribution $\chi_{ff}(q = 0)$ of the local spin component of f electrons in comparison with the behavior predicted by the two-fluid model: $K_{ff}(T)\chi_{ff}(q = 0;\ T) \sim (T + T^*)^{-1}$ (the dotted line in Fig. 4b). In connection with this, the study of the static magnetism of α-Pu caused by the radiation self-action of the material at low temperatures [10] seems to be very important. The results presented above testify to the significant role of the quantum instability effects in the degree of localization of the f electrons of Pu in the alloy in the presence of such a delicate energy balance between the localized and delocalized states in the low-temperature region.

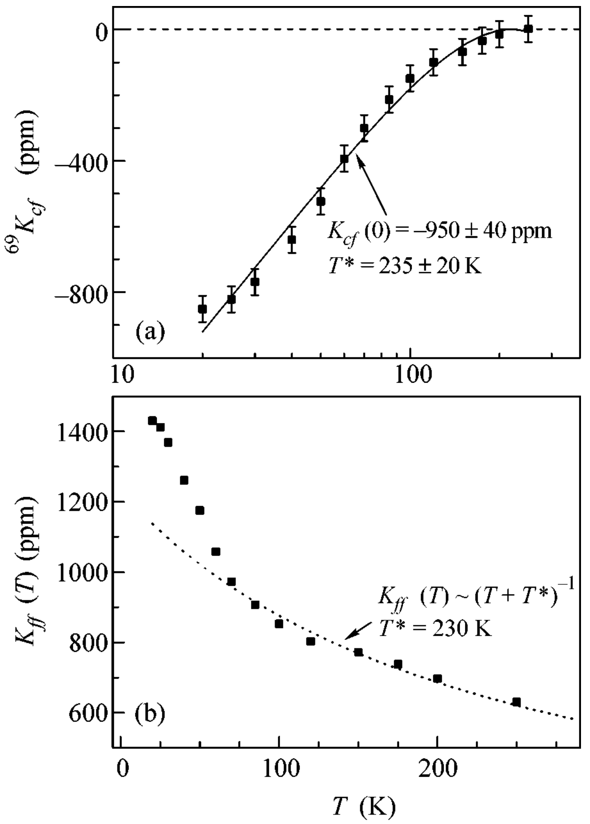

Fig. 4. (a) Temperature dependence of the heavy-fermion component of the Knight shift $K_{cf}(T)$ in $Pu_{0.95}Ga_{0.05}$. The dotted line represents the approximation of the $K_{cf}(T)$ data by the expression $K_{cf}(T) = K_{cf}(0)\{(1 - T/T^*)\log(T/T^*)\}$ with $K_{cf}(0) = -950(80)$ ppm and $T^* = 235(20)$ K. (b) Temperature dependence obtained for the incoherent spin component of the Knight shift $K_{ff}(T)$ in $Pu_{0.95}Ga_{0.05}$ by using Eqs. (2)–(4) at $B/A = 0.11$. The dotted line represents the dependence $K_{ff}(T) \sim (T + T^*)^{-1}$ at $T^* = 235$ K that is predicted by the two-fluid model of a concentrated Kondo system [14, 15]. The solid curve represents $K_{cf} = K_{cf}(0)\{(1 - T/T^*)\log(T^*/T)\}$.

In closing, we summarize the results. The combined analysis of the data on the static magnetic susceptibility and the ^{69}Ga Knight shift in a wide temperature range where the stabilized δ phase exists allowed us to determine the following features of the magnetic state of the f electron system in the $Pu_{0.95}Ga_{0.05}$ alloy:

(i) in the temperature range above $T^* = 235(40)$ K, the behavior of the spin susceptibility is typical of incoherent spin fluctuations of localized f electrons in a concentrated nonmagnetic Kondo system;

(ii) the estimate of the effective magnetic moment $\nu_{\mathrm{eff},\,5f}(g_e = 2) = 0.15(5)\mu_B$/Pu at. points to a substantial suppression of the spin magnetism contribution to the magnetic susceptibility of the alloy, which suggests that the configuration of the f shell of Pu is close to the atomic-like configuration f^6;

(iii) the behavior of $K(T)$ and $\chi(T)$ in the alloy in the temperature interval $30 < T < T^*$ can be adequately described in the framework of the two-fluid model developed by Pines *et al.* [15, 16] for Kondo lattices in the region corresponding to the formation of the coherent state of a heavy-fermion liquid. However, the final conclusion concerning the behavior of K_{cf} in the low-temperature region will depend on the understanding of the mechanisms responsible for the additional increase in the uniform contribution $\chi_{ff}(q = 0)$ of the local spin component of f electrons.

For a closer investigation of the low-temperature magnetism of f electrons of Pu, it is necessary to carry out additional studies of the spatial and frequency dispersions of spin susceptibility in the alloy.

REFERENCES

1. *Actinides—Chemistry and Physical Properties*, Ed. by L. Manes (Springer, Berlin, 1985), Struct. Bonding (Berlin), Vols. 59/60.
2. *Challenges in Plutonium Science*, Ed. by N. Cooper (Los Alamos National Laboratory, Los Alamos, 2000), Los Alamos Sci., Vol. 26; *Plutonium: Fundamentals Problems* (RFYaTs–VNIIÉF, Sarov, 2003).
3. S. S. Hecker and L. F. Timofeeva, Los Alamos Sci. **26**, 244 (2000).
4. J. C. Lashley *et al.*, Phys. Rev. Lett. **91**, 205 901 (2003).
5. S. Meot-Reymond and J. M. Fournier, J. Alloys Compd. **232**, 119 (1996).
6. V. V. Moshchalkov and N. B. Brandt, Usp. Fiz. Nauk **149**, 585 (1986) [Sov. Phys. Usp. **29**, 725 (1986)].
7. J. C. Lashley, A. Lawson, R. J. McQuenney, and G. H. Lander, cond-mat/0410634.
8. A. J. Arko, J. J. Joyce, L. Morales, *et al.*, Phys. Rev. B **62**, 1773 (2000).
9. A. O. Shorikov, A. V. Lukoyanov, M. A. Korotin, and V. I. Anisimov, Phys. Rev. B **72**, 024458 (2005).
10. M. Fluss, in *Abstracts of MAR05 Meeting* (APS, 2005).
11. F. Y. Fradin and M. B. Brodskii, Int. J. Magn. **1**, 89 (1970).
12. N. J. Curro and L. Morales, cond-mat/0205354.
13. Yu. Piskunov, K. Mikhalev, A. Gerashenko, *et al.*, Phys. Rev. B **71**, 174 410 (2005).
14. S. Nakatsuji, D. Pines, and Z. Fisk, Phys. Rev. Lett. **92**, 016 401 (2004).
15. N. J. Curro, B.-L. Young, J. Schmalian, and D. Pines, Phys. Rev. B **70**, 235 117 (2004).
16. G. C. Carter *et al.*, in *Progress in Material Science*, Ed. by B. Chalmers, J. W. Christian, and T. B. Massalski (Pergamon, Oxford, 1977), Vol. 20, Part 1, p. 33.
17. G. R. Stewart, Rev. Mod. Phys. **56**, 755 (1984).

Translated by E. Golyamina

JETP Letters, Vol. 82, No. 3, 2005, pp. 145–149. Translated from Pis'ma v Zhurnal Éksperimental'noĭ i Teoreticheskoĭ Fiziki, Vol. 82, No. 3, 2005, pp. 161–165.
Original Russian Text Copyright © 2005 by Safonov, Kharitonov, Lukashevich.

Flow of 2D Atomic Hydrogen over the Surface of Liquid ^{4}He

A. I. Safonov, A. A. Kharitonov, and I. I. Lukashevich
Russian Research Centre Kurchatov Institute, pl. Kurchatova 1, Moscow, 123182 Russia
e-mail: safonov@isssph.kiae.ru

Received June 27, 2005

Experimental evidence has been obtained for the hydrodynamic flow of a 2D gas of hydrogen atoms adsorbed on the surface of liquid helium. The observed flow manifestations are consistent with the concepts of the quantum hydrodynamics of the helium surface. This circumstance allows both investigation of the interaction of 2D hydrogen with ripplons and surface ^{3}He quasiparticles and possible future observation of the superfluidity of the 2D Bose gas of hydrogen atoms. The experimental results on thermal compression make it possible to estimate the characteristic times of the transfer of longitudinal momentum between the subsystems of hydrogen and ^{3}He atoms bound to the surface (τ_{H3}), as well as from ripplons to the substrate (τ_R). The value $\tau_{H3} \sim 4 \times 10^{-8}$ s agrees with a value calculated using the mean-field parameter U_{30} for the interaction of hydrogen atoms with the ground surface state of ^{3}He. At the same time, τ_R is more than an order of magnitude shorter than the value obtained in experiments by Mantz *et al.* Phys. Rev. Lett. **44**, 66 (1980) [Erratum: Phys. Rev. Lett. **44**, 1094 (1980)]. This discrepancy can be attributed to the dependence of the ripplon momentum relaxation rate on the substrate roughness scale. *© 2005 Pleiades Publishing, Inc.*

PACS numbers: 05.30.Jp, 47.70.Fw, 67.40.Pm, 67.65.+z, 68.03.Kn

One of the most pronounced examples of the 2D Bose gas is spin-polarized atomic hydrogen adsorbed on the liquid-helium surface (2D H↓) [1]. The aspect ($\sim 10^7$) of a 2D H↓ sample is several orders of magnitude larger and the number of atoms in this sample is much greater (up to 10^{13}) than the respective values for ultracold vapors of alkali metals in anisotropic traps [2]. Therefore, the effects of finite sizes and a finite number of particles are virtually excluded. At the same time, in contrast to superfluid-helium films with a thickness of several atomic layers, where the transition to the superfluid state has been actively investigated both theoretically and experimentally [3], 2D hydrogen is gaseous down to $T = 0$. The surface flow observed in this work for 2D H↓ with a density close to quantum degeneracy opens the real possibility of observing the superfluidity in the 2D Bose gas.

In experiments on thermal compression [4], a high density of 2D H↓ is reached on a small part of the surface cooled to temperature T_s that is much lower than the temperature T_c of the remaining walls of the cell. The initial proposal for thermal compression [5, 6] implies the equality of the local rates of adsorption and desorption. Owing to this equality, the 2D density σ that is approximately related to the density n in the cell volume as $\sigma \approx n\Lambda\exp(E_a/T)$ (Λ is the thermal wavelength and $E_a = 1.14(1)$ K is the binding energy of a hydrogen atom with the surface of isotopically pure ^{4}He [7] covering the walls of the sample cell) necessarily increases exponentially on such a "cold spot." The cold spot is located perpendicularly to the external magnetic field $B = 4.6$ T at the center of the flat mirror of the Fabri–Perot resonator of the ESR spectrometer [8], which ensures the direct diagnostics of both adsorbing and bulk phases of atomic hydrogen.

The evolution of the ESR spectrum in the process of the decay of the H↓ sample that is primarily caused by nuclear relaxation on the cell walls with sequential recombination into H_2 molecules is detected in the experiment (Fig. 1). The total power P released in the sample due to recombination is simultaneously measured (constant temperature in the cell is maintained by means of a temperature controller). The behavior of the power $P(t) \propto |dn/dt|$ is described with a high accuracy by the approximate rate equation

$$-\frac{dn}{dt} = K_{bbb}^{\text{eff}} n^3 + 2G_1^{\text{eff}} n, \tag{1}$$

which has a simple analytical solution. The fitting parameters are the zero ($n \longrightarrow 0$) power level and effective rate constants K_{bbb}^{eff} and G_1^{eff}, which correspond to the three-body recombination and nuclear relaxation, respectively, on the cell walls. The fit gives the zero power level with an accuracy of no worse than 0.01% and the rate constants with an accuracy of no worse than 1%.

It can be verified that Eq. (1) approximates the solution of the exact rate equations for the populations of two lower hyperfine states of hydrogen $|a\rangle$ and $|b\rangle$ down to $n \simeq 10^{10}$ cm^{-3}. For this density, the difference between the exact and approximate solutions does not exceed 20% (note that the measured power cannot be separated from noise even at $n \sim 10^{12}$ cm^{-2}). The con-

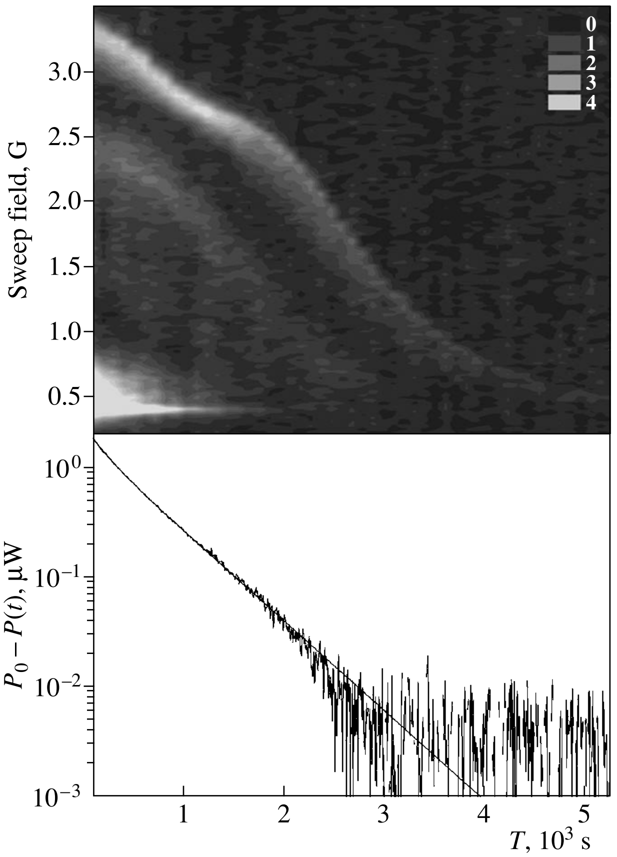

Fig. 1. (Upper panel) Evolution of the ESR spectrum of atomic hydrogen for T_c = 113 mK and T_s = 43 mK and low microwave power. Brightness represents adsorption amplitude. An intense signal near 0.5 G corresponds to H↓ atoms in the cell volume. (Lower panel) Evolution of the recombination power released in the sample cell. The smooth line is the fit by the solution of Eq. (1).

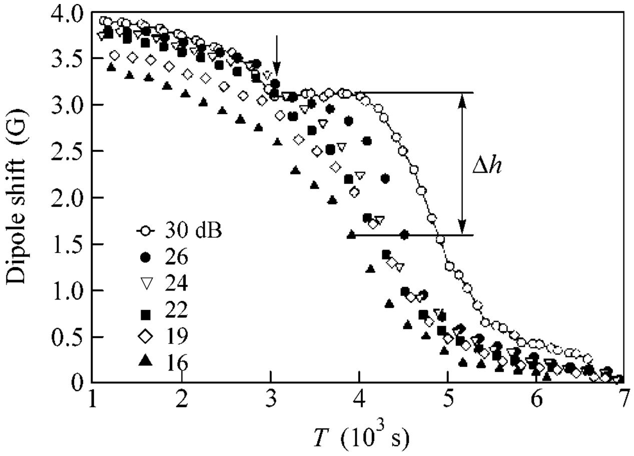

Fig. 2. Evolution of the density of 2D H↓ on the ^{3}He–^{4}He mixture in the process of the decay of the sample for various microwave powers (in dB) with respect to the level with the amplitude $H_1 \simeq 1.6$ mG. Time scales are taken so that all $P(t)$ curves coincide with each other (cf. Fig. 1) and, therefore, the corresponding volume densities $n(t)$ are identical.

servation of the exponential character of the sample decay until such low densities is explained by exchange recombination on the cold spot of hydrogen atoms in the mixed hyperfine state $|a\rangle$. The 2D density of atoms in the state $|b\rangle$ on the spot is high enough and temperature, on the contrary, low. Therefore, the recombination probability for $|a\rangle$ atoms colliding with the spot surface is comparable with the desorption probability. As a result, the exchange recombination on the cold spot is so fast that the decay of the sample is limited by the one body nuclear relaxation $|b\rangle \longrightarrow |a\rangle$ on the cell walls. For this reason, we believe that the integration of Eq. (1) with the rate constants found from the fit allows the determination of the bulk density even far beyond the resolution of the thermal-controller signal. The densities presented below for the range $n \lesssim 10^{12}$ cm^{-3} were obtained by means of such an extrapolation.

The ESR signal of 2D H↓ is shifted from the bulk signal (see Fig. 1) by a value of the demagnetizing, or dipole, field that is created by polarized H↓ dipoles on each other and is proportional to their density: $h = -A\sigma$, where $A = 1.0(1) \times 10^{-12}$ G cm^2 [9]. The dipole shift h is a quantity that is most accurately determined from the spectrum, which makes it possible to determine the 2D hydrogen density in the center of the cold spot. The ambient field is quite spatially uniform on the flat mirror of the resonator and the natural linewidth of adsorbed atoms is small [9]. Therefore, the shape of the surface signal represents the spatial distribution of the 2D density.

The instability of the ESR spectrum of 2D H↓ is observed at high microwave powers: the line acquires a triangular shape and the maximum of the adsorption signal peak is shifted from the undisturbed position that is observed for low powers (see Fig. 2). The peak shift Δh corresponds to a decrease Δσ in the surface density on the cold spot.

As was previously mentioned in [4, 10], the transport of hydrogen atoms over the surface can noticeably affect the conditions of appearing the instability of the ESR spectrum. In order to reveal the role of the 2D hydrogen flow, experimental results for isotopically pure ^{4}He are compared with the results for the ^{3}He–^{4}He mixture containing a low (of the order of 10^{12} cm^{-2}) surface concentration of ^{3}He. The idea is to use an analogy between the hydrogen flow and heat transfer over the liquid-helium surface, which is known to occur through the hydrodynamic flow of ripplon gas [11]. For the ^{3}He–^{4}He mixture, the ripplon scattering on the surface ^{3}He quasiparticles leads to the drag of the flow, which is manifested in a decrease in the effective heat conductance of the surface as compared to pure ^{4}He. Similarly, the H–^{3}He scattering should lead to the dissipation of the 2D hydrogen flow.

Figure 3 shows a decrease Δσ in the surface hydrogen density for T_c = 113 mK and T_s = 43 mK on pure ^{4}He and on the ^{3}He–^{4}He mixture due to the spectrum instability for the same microwave power. The $\Delta\sigma$ plot for the mixture clearly splits into two parts. At the beginning of the decay, i.e., for high densities, its behavior coincides with the behavior for pure ^{4}He. For low densities, two plots strongly differ from each other: the decrease $\Delta\sigma$ in the density is much larger for the mixture for the same power. It is also seen that the time dependence of the 2D density $\sigma(t)$ has a singularity at the point marked by the arrow in Fig. 2, where the indicated difference begins. An additional important observation is that the power at which the instability arises in the spectrum of 2D H↓ on the mixture is lower than that for pure ^{4}He by 3(1) dB.

Returning to the analogy with ripplons, we recall that, for a sufficiently high temperature gradient (i.e., the gradient of the ripplon-gas pressure), the complete sweeping of ^{3}He from certain sections of the surface was observed [11]. The above behavior of $\Delta\sigma$ can be treated as a similar effect caused by the scattering of adsorbed hydrogen atoms on the surface ^{3}He atoms. In this case, the coincidence of $\Delta\sigma$ values on the mixture and on pure ^{4}He means the sweeping of ^{3}He from the cold spot. For such a sweeping, the hydrogen flow should be directed outwards from the spot center. At the same time, the direction of the flow for low densities σ is obviously opposite; i.e., from the warm periphery to the cold center, because this direction is dictated by the gradient of the ripplon pressure. Therefore, the hydrogen flow changes its direction at a certain time in the process of the decay of the sample. This time (we call it the turning point) is of particular interest due to the absence of the transport of particles over the surface.

The conclusion that the hydrogen flow changes its direction is qualitatively corroborated by the behavior of σ for low powers, i.e., in the absence of the spectrum instability (see Fig. 4). It is easily seen that, for high densities, when 2D H↓ spreads from the cold spot, σ is lower on "smooth" pure ^{4}He than on the "rough" mixture. At the same time, for low powers and, therefore, a flow toward the center, the opposite pattern is observed. The turning point obviously corresponds to the intersection of $\sigma(t)$ curves for pure ^{4}He and for the mixture: in the absence of the flow, the effect of ^{3}He disappears and the surface density is identical for both cases.

It is necessary to emphasize that, in the absence of the transport over the surface, i.e., when the adsorption rate is equal to the desorption rate, the density on the mixture is necessarily lower, because the adsorption energy E_a is lower [7]. However, the difference between the σ values on pure ^{4}He and on the ^{3}He–^{4}He mixture for high densities has the opposite sign, which can be considered as additional direct evidence of the 2D hydrogen flow.

We use the above evidence of the 2D H↓ flow in order to estimate the rates of momentum transfer between the components of 2D mixture. In the absence of ^{3}He, the velocities of the steady flow of ripplons and hydrogen are given by the respective expressions [10]

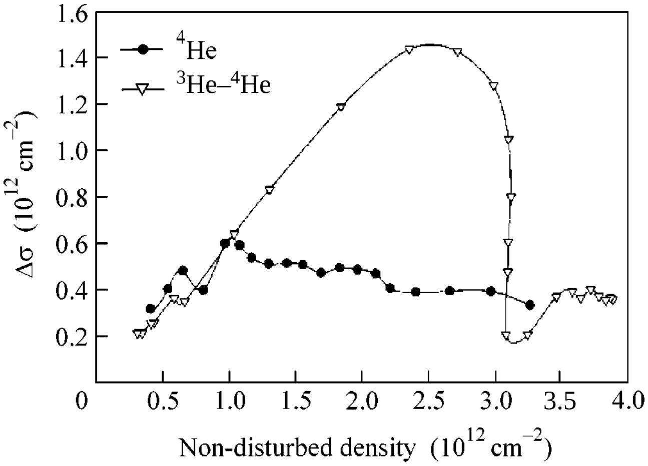

Fig. 3. Quantity $\Delta\sigma$ on pure ^{4}He and on the ^{3}He–^{4}He mixture for the same power level of 19 dB (cf. Fig. 2). A sharp change in $\Delta\sigma$ at $\sigma = 3.1 \times 10^{12}$ cm^{-2} is associated with the sweeping of ^{3}He from the cold spot by the flow of the hydrogen–ripplon mixture.

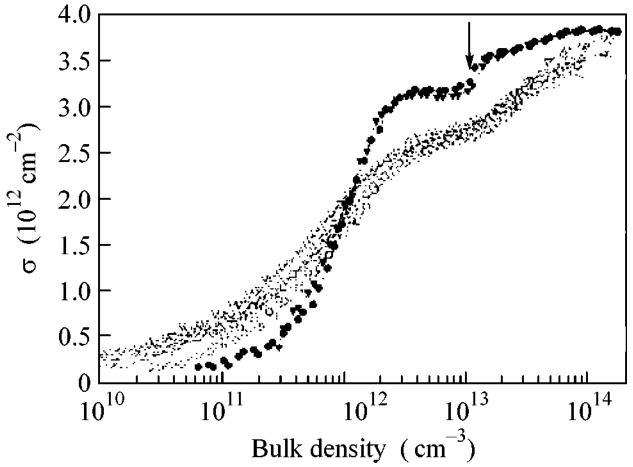

Fig. 4. Evolution of the density of 2D H↓ on (open symbols) pure ^{4}He and (closed symbols) the ^{3}He–^{4}He mixture for a low microwave power. Different symbols correspond to different samples under identical conditions.

$$\mathbf{u}_{\mathrm{H}} = -\frac{\tau_{\mathrm{R}}}{\rho_{\mathrm{R}}}(\nabla P + x\nabla P_{\mathrm{H}}), \quad \mathbf{u}_{\mathrm{R}} = -\frac{\tau_{\mathrm{R}}}{\rho_{\mathrm{R}}}\nabla P, \qquad (2)$$

where $P = P_{\mathrm{H}} + P_{\mathrm{R}}$ is the total pressure and $x = (\rho_{\mathrm{R}}/\rho_{\mathrm{H}})(\tau_{\mathrm{HR}}/\tau_{\mathrm{R}})$. We define the effective surface temperature $T_{\mathrm{eff}}(\sigma, n)$ as a value at which the adsorption rate is equal to the desorption rate for given σ and n values. We also introduce the effective pressure P_{eff} of hydrogen–ripplon mixture calculated for T_{eff} and measured σ

value. Disregarding recombination losses, we obtain $T = T_{\mathrm{eff}}$ and $P = P_{\mathrm{eff}}$ for $\mathbf{u}_{\mathrm{H}} = 0$ in the limit of low microwave power. At the same time, for $\mathbf{u}_{\mathrm{R}} = 0$, we have $\nabla P = 0$; i.e., the total pressure is uniform and is equal to its value P_c on the warm cell walls of the cell. The latter value is easily calculated from the known bulk density n and cell temperature T_{c}.

In Fig. 4, the turning point of the hydrogen flow $\mathbf{u}_{\mathrm{H}} = 0$ (intersection of the curves for pure ^{4}He and for the mixture) occurs for $\sigma = 1.7(3) \times 10^{12}$ cm^{-2} and $n = 1.0(2) \times 10^{12}$ cm^{-3} so that $T_{\mathrm{eff}} = 77(1)$ mK. Then, we obtain $P = 0.83(7)P_{\mathrm{c}}$ and $P_h = 0.43(7)P_{\mathrm{c}}$, which provide the estimate $x \sim 0.4$. At the same time, comparison of τ_{R} measured by Mantz *et al.* [11] and τ_{HR} calculated by Zimmerman and Berlinsky [12] gives $x = 0.01$. We emphasize that the numerical solution of transport equations presented in [10] also agrees with experimental data only if the time τ_{R} is much shorter than the value measured by Mantz *et al.* [11] (otherwise, the hydrogen flow towards the spot center at the end of the sample decay would be so fast that the 2D density σ on the spot would remain high much longer than the interval actually observed). Such a discrepancy may be caused by the dependence of τ_{R} on the substrate surface roughness [13].

Knowing the pressure drop of the hydrogen–ripplon mixture necessary for the sweeping of ^{3}He from the cold spot, one can estimate the ^{3}He density on the warm walls of the sample cell. For a flow from the center to the periphery, $T_{\mathrm{eff}} > T$ and, hence, $P_{\mathrm{eff}} > P > P_{\mathrm{c}} + P_3$. Therefore, the difference $P_{\mathrm{eff}} - P_{\mathrm{c}}$ provides an upper estimate for the pressure $P_3 = n_3 k_{\mathrm{B}} T_{\mathrm{c}}$ of 2D ^{3}He on the cell walls. Under the conditions corresponding to Figs. 3 and 4, the sweeping of ^{3}He from the spot occurs for $\sigma = 3.1 \times 10^{12}$ cm^{-2} and $n = 1.0 \times 10^{13}$ cm^{-3} so that $T_{\mathrm{eff}} = 87$ mK. Therefore, $P_{\mathrm{eff}} - P_{\mathrm{c}} \sim 1.5 \times 10^{-5}$ dyne/cm and, finally, $n_3 \lesssim 9.5 \times 10^{11}$ cm^{-2}. For low densities of hydrogen, e.g., at the end of decay, n_3 at the center may increase to $\sim 6 \times 10^{12}$ cm^{-2} due to the flow of ripplons towards the center of the spot. This increase leads to a decrease in the hydrogen adsorption energy E_{a} by ~1% [7] and thereby to an increase in the desorption rate. However, the corresponding decrease in the density $\sigma \lesssim 10\%$ is negligibly small compared to the difference between the values observed on pure ^{4}He and the ^{3}He–^{4}He mixture.

The deviation of the surface temperature from the undisturbed value in the case of the instability of the ESR spectrum is given by the expression

$$\Delta T \approx \frac{f D_{\sigma}}{2\tau_{\mathrm{ESR}}(\partial Q_{\mathrm{RP}}/\partial T)} \qquad (3)$$

and is related to the deviation of the density on pure ^{4}He and the ^{3}He–^{4}He mixture as [10]

$$mc^2 \Delta\sigma_4 \simeq -\left[\frac{S_{\mathrm{R}}}{1+x} + \left(\frac{\partial P_{\mathrm{H}}}{\partial T}\right)_{\sigma} + \frac{x\tilde{S}}{1+x}\right]\Delta T, \qquad (4)$$

$$mc^2 \Delta\sigma_{\mathrm{mix}} \simeq mc^2 \Delta\sigma_4 - \left(\frac{\tau_{\mathrm{HR}}}{\tau_{\mathrm{H3}}}\right)\tilde{S}\Delta T, \qquad (5)$$

respectively. Here, $\tilde{S} \simeq \sigma(E_a/T)\tau_*^2(\tau_s\tau_{\mathrm{HR}})^{-1}$, where $\tau_* = r_*\sqrt{m/2T} \simeq 2.3 \times 10^{-5}$ s is the characteristic time of the propagation of sound over the spot and $r_* \simeq 0.8$ mm is the radius of the cold spot [4, 9]. According to the above expressions, $\Delta\sigma$ on pure ^{4}He is larger than that on the ^{3}He–^{4}He mixture for the same microwave power in agreement with the experiment.

For the microwave field amplitude $H_1 \simeq 10^{-5}$ G that is slightly higher than the critical value for arising instability, $\Delta\sigma/\sigma \simeq 0.1$ on pure ^{4}He. Then, we obtain $\Delta T \simeq 2.3$ mK and $E_{\mathrm{a}}\Delta T/T^2 \simeq 0.3$, which corroborates the validity of the linear approximation used in [10] to derive Eqs. (4) and (5). At the turning point of the hydrogen flow ($\sigma = 1.7 \times 10^{12}$ cm^{-2}, $T = 77$ mK, $\tau_{\mathrm{ESR}} \simeq 1.3$ s), from Eq. (3) we obtain the fraction of recombination energy locally released at the place of an elementary act, $f \simeq 0.014$, in agreement with the previous results [14]. However, it is worth noting that the real f value may be masked by the diffusion of excited H_2^* molecules in a gap of the width $d = 0.6$ mm and radius $R = 5$ mm between the flat mirror of the resonator and a Kapton film located above it [4]. The average number of collisions between a molecule and walls before the molecule leaves the gap is $N \sim R^2/d^2$ and is comparable with the number of collisions $N_{1/2} \sim 150$ that is necessary for loosing half the excitation energy [14]. Therefore, a considerable fraction of energy released in the recombination on the cold spot remains in the gap and is distributed over the surfaces bounding it. The fraction $r_0^2/2R^2 \sim 0.01$ returning to the cold spot is comparable with the above f value that thereby should be treated as an upper estimate.

The ratio of the critical microwave powers at which the instability arises in the ESR spectrum of 2D H↓ on pure ^{4}He and on the mixture is equal to 2.0(5). Since $\Delta\sigma$ is proportional to the power, this ratio is equal to the ratio of the respective $\Delta\sigma$ values observed for the same power. At the turning point, from Eqs. (4) and (5), we obtain $\tau_{\mathrm{HR}}/\tau_{\mathrm{H3}} = 2.1(8)$ and, finally, $\tau_{\mathrm{H3}} = 3.9(1.5) \times 10^{-8}$ s in the complete agreement with a value of 3×10^{-8} s calculated from the mean-field parameter U_{30} for the interaction between H and ^{3}He [10].

Finally, we discuss the conclusion made by Reynolds *et al.* [15] that the weak coupling of ripplons with film phonons and comparatively high heat conductivity of ripplons have negative consequences for the success of experiments with the cold spot. For low hydrogen densities, the result is opposite to the statement made in [15]: the weaker the coupling of ripplons with the substrate, the higher the velocity of the ripplon flow towards the center of the spot and, therefore, the higher the density of hydrogen entrained by the ripplon flow to the spot. Moreover, weak coupling with the substrate equalizes the total pressure P rather than the ripplon temperature. On the contrary, the temperature undergoes a sharp jump at the spot boundary reflecting the drop of the density and pressure of hydrogen.

The above evidence of the hydrodynamic flow of the 2D Bose gas of H↓ atoms open the wide possibilities for studying the interaction of hydrogen with ripplons and ^{3}He quasiparticles on the helium surface, which is demonstrated by the above estimates of the time constants of momentum transfer. A further advance to the quantum degeneracy region may require the combination of thermal and magnetic compression of 2D hydrogen. The main difficulty in this way seems to be the conservation of the high uniformity of the magnetic field in the region of dense 2D H↓ that is necessary for direct detection by ESR.

We are deeply grateful to S.A. Vasilyev, J. Järvinen, and S. Jaakkola for invaluable contribution to the preparation and conduction of measurements at Wihuri Physical Laboratory, University of Turku, Finland, as well as for numerous fruitful discussions. This work was supported by the Ministry of Education and Science of the Russian Federation, INTAS (grant no. 2001-0552), the Russian Foundation for Basic Research (project nos. 02-02-16652-a and 05-02-16858-a), and the Wihuri Foundation.

REFERENCES

1. A. I. Safonov, S. A. Vasilyev, I. S. Yasnikov, *et al.*, Phys. Rev. Lett. **81**, 4545 (1998).
2. A. Görlitz, J. M. Vogels, A. E. Leanhardt, *et al.*, Phys. Rev. Lett. **87**, 130 402 (2001).
3. D. J. Bishop and J. D. Reppy, Phys. Rev. B **22**, 5171 (1980).
4. S. A. Vasilyev, A. I. Safonov, J. Järvinen, *et al.*, Phys. Rev. Lett. **89**, 153 002 (2002).
5. B. V. Svistunov, T. W. Hijmans, G. V. Shlyapnikov, and J. T. M. Walraven, Phys. Rev. B **43**, 13 412 (1991).
6. A. Matsubara, T. Arai, S. Hotta, *et al.*, Physica B (Amsterdam) **194–196**, 899 (1994).
7. A. I. Safonov, S. A. Vasilyev, A. A. Kharitonov, *et al.*, Phys. Rev. Lett. **86**, 3356 (2001).
8. S. A. Vasilyev, J. Järvinen, E. Tjukanoff, *et al.*, Rev. Sci. Instrum. **75**, 94 (2004).
9. S. A. Vasilyev, J. Järvinen, A. I. Safonov, and S. Jaakkola, Phys. Rev. A **69**, 023610 (2004).
10. A. I. Safonov, A. A. Kharitonov, and I. I. Lukashevich, J. Low Temp. Phys. **138**, 295 (2005).
11. I. B. Mantz, D. O. Edwards, and V. U. Nayak, Phys. Rev. Lett. **44**, 66 (1980) [Erratum: Phys. Rev. Lett. **44**, 1094 (1980)].
12. D. S. Zimmerman and A. J. Berlinsky, Can. J. Phys. **61**, 508 (1983).
13. A. I. Safonov, S. S. Demukh, and A. A. Kharitonov, Pis'ma Zh. Éksp. Teor. Fiz. **79**, 362 (2004) [JETP Lett. **79**, 304 (2004)].
14. S. A. Vasilyev, E. Tjukanov, M. Mertig, *et al.*, Europhys. Lett. **24**, 223 (1993).
15. M. W. Reynolds, I. D. Setija, and G. V. Shlyapnikov, Phys. Rev. B **46**, 575 (1992).

Translated by R. Tyapaev

JETP Letters, Vol. 82, No. 3, 2005, pp. 150–154. From Pis'ma v Zhurnal Éksperimental'noĭ i Teoreticheskoĭ Fiziki, Vol. 82, No. 3, 2005, pp. 166–170.
Original English Text Copyright © 2005 by Pruisken, Baranov, Burmistrov.

Non-Fermi Liquid Theory of Quantum Hall Effects¶

A. M. M. Pruisken[a], M. A. Baranov[b, c], and I. S. Burmistrov[a, d]
[a] *Institute for Theoretical Physics, University of Amsterdam, 1018 XE Amsterdam, The Netherlands*
[b] *Van der Waals–Zeeman Institute for Experimental Physics, University of Amsterdam, 1018 XE Amsterdam, The Netherlands*
[c] *Russian Research Centre Kurchatov Institute, Moscow, 123182 Russia*
[d] *Landau Institute for Theoretical Physics, Russian Academy of Sciences, Moscow, 117940 Russia*
e-mail: burmi@itp.ac.ru

Received June 28, 2005

Within the Grassmannian $U(2N)/U(N) \times U(N)$ nonlinear σ-model representation of localization, one can study the low-energy dynamics of both a free and interacting electron gas. We study the crossover between these two fundamentally different physical problems. We show how the topological arguments for the exact quantization of the Hall conductance are extended to include the Coulomb interaction problem. We discuss dynamical scaling and make contact with the theory of variable range hopping. *© 2005 Pleiades Publishing, Inc.*

PACS numbers: 71.10.Pm, 72.10.–d, 73.43.–f

Over the last few years, much effort has been devoted to the problem of localization and interaction effects in the quantum Hall regime [1–6]. By now, it is well understood that the Coulomb interaction problem falls into a non-Fermi liquid universality class of transport problems with a novel symmetry, called $\mathcal{F}$ *invariance* [2]. Although the results for scaling are in many ways similar to those obtained for a free electron gas [7], it is important to bear in mind that the Coulomb interaction problem is a far richer one. Unlike the free-particle problem, for example, the field theory for interacting particles provides a platform for the unification of the *fractional quantum Hail regime* and the quantum theory of metals [2, 4–6]. The principal features of this unification are encapsulated in a scaling diagram for the *longitudinal* and *Hall conductances* σ_{xx} and σ_{xy}, respectively (figure). The Finkelstein approach to localization and interaction phenomena [8, 9], the topological concept of an instanton vacuum [10], as well as the Chern–Simons statistical gauge fields [11], are all essential in composing this diagram.

The main objective of this letter is to embark on the most fundamental aspect of the theory, the *observability* and *precision* of the quantum Hall effect. This experimental phenomenon is represented in the figure by the infrared stable fixed points located at $\sigma_{xx} = 0$ and $\sigma_{xy} = k$ (integer effect) as well as $\sigma_{xy} = k/(2k + 1)$ (Jain series) [12]. These fixed points, however, define the strong coupling phase of the unifying action, where analytic work is generally impossible. In spite of ample experimental evidence for its existence, the *robust quantization* of the Hall conductance has yet to be established as a fundamental but previously unrecognized feature of the topological θ vacuum concept [10].

In what follows, we shall benefit from the advancements reported in [13]. In particular, since the Finkelstein theory is formally defined as a σ model on the Grassmann manifold $U(2N)/U(N) \times U(N)$ with N equal to N_r (number of *replicas*) times N_m (number of *Matsubara frequencies*), we can now use our general knowledge on the strong coupling behavior of the the-

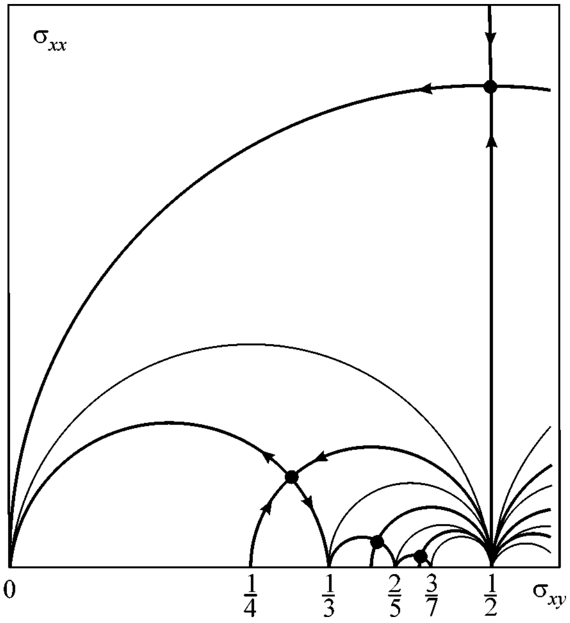

Unified scaling diagram for the quantum Hall effects in the σ_{xx}, σ_{xy} conductivity plane. The arrows indicate the direction towards the infrared.

[¶] The text was submitted by the authors in English.

ory and probe, for the first time, the quantum Hall phases in the interacting electron gas.

To achieve our goals, we shall first outline some of the recent advancements in the field. It is important to emphasize that a *complete* effective action for interacting particles now exists [2]. This action includes the coupling to external potentials and/or Chern–Simons gauge fields. This leads to a detailed understanding of the electrodynamic $U(1)$ gauge invariance and provides invaluable information on the renormalization of the theory that was not available before.

Second, it is necessary to have a more detailed understanding of how the subtleties of interaction effects can be understood as a field theory. For this purpose, we report new results on the Grassmannian nonlinear σ model with $N_r = 0$ and varying N_m. These show explicitly how the crossover takes place between a theory of *free particles* at finite values of N_m and a *many-body* theory that is generally obtained only in the limit $N_m \longrightarrow \infty$. Armed with these insights, we next point out how the Coulomb interaction problem, at zero temperature (T), displays the general topological features and θ dependence that were discovered in [13].

As a third and final step toward the strong coupling phase, we discuss the subject of dynamical scaling. As a unique product of our effective action procedure, we obtain a distinctly different behavior at finite T, depending on the specific regime of the interacting electron gas that one is interested in. We establish, at the same time, a correspondence with the theory for *variable range hopping* [14].

The action. Following Finkelstein [8], the effective quantum theory for disordered (spin-polarized or spinless) electrons is given in terms of a generalized σ model involving the unitary matrix field variables $Q^{\alpha\beta}_{nm}(\mathbf{r})$, which obey $Q^2(\mathbf{r}) = \mathbf{1}$. Here, α and β represent the replica indices and n and m are the indices of the Matsubara frequencies $\omega_k = \pi T(2k + 1)$. In terms of ordinary unitary rotations $\mathcal{T}^{\alpha\beta}_{nm}$, one can write

$$Q = \mathcal{T}^{-1}\Lambda\mathcal{T}, \quad \Lambda = \Lambda^{\alpha\beta}_{nm} = \operatorname{sgn}(\omega_n)\mathbf{1}^{\alpha\beta}_{nm} \tag{1}$$

indicating that the Q describes a Goldstone manifold of a broken symmetry between positive and negative frequencies. A $U(1)$ gauge transformation in frequency space is represented by a unitary matrix $\mathcal{W}^{\alpha\beta}_{nm}$

$$\mathcal{W} = \exp\left\{i\sum_{n,\alpha}\phi^{\alpha}(\mathbf{r}, \nu_n)I^{\alpha}_n\right\}, \tag{2}$$

with $\nu_n = 2\pi Tn$. Here, $[I^{\gamma}_k]^{\alpha\beta}_{nm} = \delta^{\alpha\gamma}\delta^{\beta\gamma}\delta_{n,\, m+k}$ denote the $U(1)$ generators. In finite frequency space with a cutoff (N_m), the I matrices no longer span a $U(1)$ algebra. To define the $U(1)$ gauge invariance in a truncated frequency space, we have developed a set of rules ($\mathcal{F}$ *algebra* [2]). These involve one more (frequency) matrix, $\eta^{\alpha\beta}_{nm} = n\delta^{\alpha\beta}_{nm}$, that is used to represent ω_n. The effective action for electrons in a static magnetic field B and coupled to external potentials and/or Chern–Simons fields $a^{\alpha}_{\mu}(\mathbf{r}, \nu_n)$ with $\nu_n \neq 0$ can now be written as [2]

$$S_{\text{eff}} = S_{\sigma} + S_F + S_U + S_0. \tag{3}$$

Here, S_{σ} is the free-electron piece [7]

$$\begin{aligned} S_{\sigma} = {} & -\frac{\sigma_{xx}}{8}\int d\mathbf{r}\,\mathrm{tr}[D_i, Q][D_i, Q] \\ & + \frac{\sigma_{xy}}{8}\int d\mathbf{r}\,\mathrm{tr}\epsilon_{ij}Q[D_i, Q][D_j, Q], \end{aligned} \tag{4}$$

where $D_j = \nabla_j - i\sum_{n\alpha}a^{\alpha}_j(\mathbf{r}, \nu_n)I^{\alpha}_n$ is the covariant derivative. Next, the two pieces S_F and S_U are linear in temperature T and represent interaction terms. S_F is gauge-invariant and contains the *singlet interaction* term [8]

$$S_F = \pi zT\int d\mathbf{r}\left[\sum_{\alpha n}\mathrm{tr}I^{\alpha}_n Q\,\mathrm{tr}I^{\alpha}_{-n}Q + 4\mathrm{tr}\eta Q - 6\mathrm{tr}\eta\Lambda\right]. \tag{5}$$

The (Coulomb) term S_U contains the scalar potential

$$\begin{aligned} S_U = {} & -\pi T\sum_{\alpha n}\int d\mathbf{r}d\mathbf{r}'\left[\mathrm{tr}I^{\alpha}_n Q(\mathbf{r}) - \frac{1}{\pi T}\tilde{a}^{\alpha}_0(\mathbf{r}, \nu_{-n})\right] \\ & \times U^{-1}(\mathbf{r} - \mathbf{r}')\left[\mathrm{tr}I^{\alpha}_{-n}Q(\mathbf{r}') - \frac{1}{\pi T}\tilde{a}^{\alpha}_0(\mathbf{r}', \nu_n)\right]. \end{aligned} \tag{6}$$

The S_0 contains the magnetic field $b^{\alpha} = \epsilon_{ij}\nabla_i a^{\alpha}_j$:

$$S_0 = -\frac{\rho^2_B}{2\rho T}\int d\mathbf{r}\sum_{\alpha n}b^{\alpha}(\mathbf{r}, \nu_n)b^{\alpha}(\mathbf{r}, \nu_{-n}). \tag{7}$$

We have defined (dropping the replica index α on a_{μ})

$$\tilde{a}_0 = a_0 - \frac{i\rho_B}{\rho}b, \quad U(q) = \rho^{-1} + U_0(q). \tag{8}$$

Here, the density of states $\rho = (\partial n/\partial\mu)_{T,\,B}$ and the quantity $\rho_B = (\partial n/\partial B)_{T,\,\mu}$ are thermodynamic quantities, n and μ being the particle density and the chemical potential, respectively. The statement of gauge invariance now means that the theory is invariant under the following transformation:

$$Q \longrightarrow \mathcal{W}^{-1}Q\mathcal{W}, \quad a_{\mu} \longrightarrow a_{\mu} + \partial_{\mu}\phi. \tag{9}$$

Using Eq. (9), it is easy to see that the action is invariant under spatially independent gauge transformations $\phi = \phi(\nu_n)$ provided the interaction potential U_0 has an infinite range. This global invariance, termed $\mathcal{F}$ *invariance*, is an exact symmetry of the Coulomb interaction problem which in two spatial dimensions is represented by $U_0^{-1}(q) = \Gamma|q|$.

Static versus dynamic response. Our introduction of external potentials (statistical gauge fields) a_μ can be exploited immediately to elucidate the fundamental aspects of the quantum transport problem in strong B. For this purpose, we consider $S_{\mathrm{eff}}[a_\mu]$ obtained after elimination of the Q fields. Defining the particle density $n_m = T\delta S_{\mathrm{eff}}/\delta a_0(\nu_{-m})$, we obtain, at a tree level, the continuity equation [2]

$$\begin{aligned}\nu_m(n_m + i\sigma_{xy}b) &= \nabla[\sigma_{xx}(\mathbf{e} + \nabla(U_0 n_m)) \\ &\quad - D_{xx}\nabla(n_m + i\rho_B b)].\end{aligned} \tag{10}$$

Here, $D_{xx} = \sigma_{xx}/\rho$ denotes the diffusion constant and $\mathbf{e}$ and b are the external electric and magnetic fields, respectively. This result is familiar from the theory of metals [15], where the quantity ρ_B is usually neglected. Notice that, in the static limit $\nu_n \longrightarrow 0$, both quantities σ_{ij} drop out and the equation now contains only the thermodynamic quantities ρ, ρ_B, and U_0. Since the fields $a_\mu(\mathbf{r}, \nu_n = 0)$ are completely decoupled from the Q field variables, the static response is actually determined by a different, underlying theory. This means that ρ, ρ_B, U_0, and, hence, S_U and S_0 should not have any quantum corrections in general, either perturbatively or nonperturbatively. This observation can be used as a general physical constraint that must be imposed on the quantum theory. The only quantities that are allowed to have quantum corrections are the transport parameters σ_{xx}, σ_{xy}, and the singlet interaction amplitude z.

As an important check on the statements of gauge invariance and renormalization, we have evaluated the quantum theory in $2 + \epsilon$ spatial dimensions to order ϵ^2. The results of the computation, along with an extensive analysis of dynamical scaling, have been reported in [6].

$\mathcal{F}$ invariance. The renormalizability can be addressed more formally by establishing a correspondence with the theory of ordinary nonlinear sigma models [16]. For this purpose, we drop the external potentials from the action and recall that, for finite size matrices Q, operators like S_F play the role of infrared regulators that do not affect the singularity structure of the theory at short distances. We know, in particular, that the theory is renormalizable in two dimensions. Besides the coupling constant or σ_{xx}, one additional renormalization constant is needed for the operators linear in the Q matrix field and two more are generally needed for the operators bilinear in the Q (i.e., the symmetric and antisymmetric representation, respectively) [17]. These general statements apply to the Finkelstein action as well, since the latter only demands that the number of Matsubara frequencies N_m is taken to infinity (along with $N_r \longrightarrow 0$). To completely elucidate this point, we have computed the crossover functions for the theory, where the quantity $U^{-1}(\mathbf{r} - \mathbf{r}')$ in S_U (Eq. (6)) is replaced by its most relevant part

$$U^{-1}(\mathbf{r} - \mathbf{r}') \longrightarrow z(1-c)\delta(\mathbf{r} - \mathbf{r}'). \tag{11}$$

Notice that $0 < c < 1$ represents the finite range interaction case. The extreme cases $c = 0$ and 1 describe the free electron gas and the Coulomb system, respectively. $\mathcal{F}$ invariance is retained only for $c = 1$ and broken otherwise.

The following renormalization-group functions have been obtained for the parameters z, c and the dimensionless resistance $g = \mu^\epsilon/\pi\sigma_{xx}$ in $2 + \epsilon$ spatial dimensions (μ denotes an arbitrary momentum scale) [18]:

$$\frac{dg}{d\ln\mu} = \epsilon g - 2g^2\left[f + \frac{1-c}{c}\ln(1-cf)\right], \tag{12}$$

$$\frac{d\ln z}{d\ln\mu} = gcf, \tag{13}$$

$$\frac{dc}{d\ln\mu} = gc(1-cf). \tag{14}$$

Here, $f = M^2/(\mu^2 + M^2)$ is a μ-dependent function with $M^2 = 8\pi zTN_m/\sigma_{xx}$ which depends on the cutoff N_m.

For $f = 0$ ($\mu \gg M$ or short distances), we obtain the well-known results for free particles [16, 17]; i.e., $dg/d\ln\mu$ has no one-loop contribution, z has no quantum corrections in general, and the result for c coincides with the renormalization of symmetric operators, bilinear in Q.

For $f = 1$ ($\mu \ll M$ or large distances), we obtain the peculiar Finkelstein results of the interacting electron gas [3, 9]. The symmetry-breaking parameter c now affects the renormalization of all the other parameters. The concept of $\mathcal{F}$ invariance ($c = 1$) manifests itself as a new (non-Fermi liquid) fixed point in the theory. The problem with $0 < c < 1$ lies in the domain of attraction of the Fermi liquid line $c = 0$, which is stable in the infrared.

Notice, however, that the $\mathcal{F}$-invariant fixed point $c = 1$ only exists if the mass M in the theory remains finite at zero T. This clearly shows that, in order for $\mathcal{F}$ invariance to represent an exact symmetry of the problem, N_m must be infinite. The time τ plays the role of an extra, nontrivial dimension, and this dramatically complicates the problem of plateau transitions in the quantum Hall regime. The Coulomb interaction problem, unlike the free electron theory, is given as a (2 + 1)-dimensional field theory, thus invalidating any attempt toward exact solutions of the experimentally observed critical indices [19–22].

The quantum Hall effect. Next, we turn to the most interesting aspect of the theory, the σ_{xy} term (θ term), which is invisible in perturbative expansions. However, we may proceed along the same lines as pointed out in

[13] and separate, in the theory for $T = 0$, the *bulk* quantities from the *edge* quantities [10, 23]

$$\sigma_{xy} = \nu_B = k + \frac{\theta}{2\pi}, \quad k \in \mathbb{Z}, \quad -\pi < \theta \le \pi, \tag{15}$$

where ν_B stands for the filling fraction. Specifying to the Coulomb interaction problem ($c = 1$) in two spatial dimensions, we next make use of the principle of $\mathcal{F}$ invariance and formulate an effective action for the edge. Introducing a change of variables $Q = t^{-1}Q_0 t$ [10], we now have [24] ($q = t^{-1}\Lambda t$)

$$S_{\text{eff}}[q] = S_{\text{bulk}}[q] + 2\pi i k C[q],$$
$$e^{S_{\text{bulk}}[q]} = \int_{\partial V} D[Q_0] e^{\tilde{S}_\sigma[t^{-1}Q_0 t] + S_F[t^{-1}Q_0 t]}. \tag{16}$$

Here, $\tilde{S}_\sigma$ is the same as S_σ with σ_{xy} replaced by its *unquantized* bulk piece θ. Recall that the symbol ∂V reminds us that the functional integral is performed with a fixed value $Q_0 = \Lambda$ at the edge. It is important to notice that the interaction piece S_F cannot be left out, since it affects, following Eqs. (12)–(14), the renormalization of the theory at $T = 0$.

The definition of $S_{\text{eff}}[t]$ is precisely the same as the *background field* methodology adapted to the Coulomb interaction problem [1, 3]. The result is of the form

$$S_{\text{bulk}}[q] = \tilde{S}'_\sigma[q] + S'_F[q], \tag{17}$$

where the primes indicate that the parameters σ_{xx}, θ, and z are replaced by renormalized ones, σ'_{xx}, θ', and z', respectively, which are defined for system size L.

This leads to the most important statement of this letter: provided a *mass* is generated for *bulk* excitations, the renormalized theory $\sigma'_{xx} = \sigma_{xx}(L)$, $\theta' = \theta(L)$, and $z' = z(L)$ should vanish for large enough L; i.e., the bulk of the system is insensitive to changes in the boundary conditions, except for corrections exponentially small in L. Under these circumstances, $S_{\text{eff}}[q]$ reduces to the action of *massless chiral edge excitations* [4, 5]. The integer k equals the number of edge modes and is now identified as the *quantized Hall conductance.*

These results describe the strong coupling "integer quantum Hall" fixed points (figure) that were previously conjectured on phenomenological grounds. From the weak coupling side, a detailed analysis of Eqs. (16) and (17) leads to the following expressions [1] for the renormalization-group functions:

$$\frac{d\sigma_{xx}}{d\ln\mu} = \beta_\sigma = \beta_\sigma^0(\sigma_{xx}) + D\sigma_{xx}^2 e^{-2\pi\sigma_{xx}}\cos\theta, \tag{18}$$

$$\frac{d\sigma_{xy}}{d\ln\mu} = \beta_\theta = D\sigma_{xx}^2 e^{-2\pi\sigma_{xx}}\sin\theta, \tag{19}$$

$$\frac{d\ln z}{d\ln\mu} = \gamma_z = \gamma_z^0(\sigma_{xx}) + D_\gamma\sigma_{xx}e^{-2\pi\sigma_{xx}}\cos\theta. \tag{20}$$

Here, $D \approx 13.58$ and $D_\gamma \approx 2.26$ are determined by the instanton determinant [24] and β_σ^0 and γ_z^0 are the perturbative results that recently have been extended to two-loop order ($\mathcal{A} \approx 1.64$) [3, 6]

$$\beta_\sigma^0(\sigma_{xx}) = \frac{2}{\pi} + \frac{4\mathcal{A}}{\sigma_{xx}}, \tag{21}$$

$$\gamma_z^0(\sigma_{xx}) = \frac{1}{\pi\sigma_{xx}} + \frac{18 + \pi^2}{6\pi^2\sigma_{xx}^2}. \tag{22}$$

In summary, there is now fundamental support, both from the weak and strong coupling side, for the scaling diagram of the integral quantum Hall effect [1].

Finite *T*. At finite T, the infrared of the system is controlled by the interaction terms S_F and S_U. In this case, one must go back to the original theory (Eqs. (3)–(7)) and obtain the transport parameters from linear response in the field a_μ [3]. Specifying to the $a_0 = 0$ gauge as well as $\nabla \cdot \mathbf{a} = \nabla \times \mathbf{a} = 0$, we can write

$$S_{\text{eff}}[a] = T\sum_{n>0}\int d\mathbf{r}\,\nu_n[\sigma'_{xx}\delta_{ij} + \sigma'_{xy}\epsilon_{ij}]a_i(\nu_n)a_j(-\nu_n), \tag{23}$$

where the expressions for σ'_{ij} are known as the *Kubo formulas* [3]. We stress that these expressions are exactly the same as those obtained from the background field procedure, $\sigma'_{xx} = \sigma_{xx}(L)$ and $\sigma'_{xy} = k + \theta(L)/(2\pi)$ (Eqs. (17)–(20)), provided $S_{\text{eff}}[a]$ is evaluated at $T = 0$ and with $Q = \Lambda$ at the edge [2, 3].

The scaling results at finite T generally depend on the specific regime and/or microscopics of the disordered electron gas that one is interested in. Here, we consider the most interesting cases, where $\theta \approx \pm\pi$ and $\theta \approx 0$, respectively. The first case is realized when the Fermi level passes through the center of the Landau band, where the electron gas is quantum critical and the transition takes place between adjacent quantum Hall plateaus [7]. Provided the bare parameter σ_{xx} of the theory is close to the critical fixed point σ_{xx}^* at $\sigma_{xy} = 1/2$ (figure), the following universal scaling law is observed [7]:

$$\sigma'_{xx} = \sigma_{xx}(X), \quad \sigma'_{xy} = k + \frac{\theta(X)}{2\pi}, \tag{24}$$

where $X = (zT)^{-\kappa}\Delta\nu_B$. Here, $\Delta\nu_B$ is the filling fraction ν_B of the Landau levels relative to the critical value ν_B^*, which is half-integer. The correlation (localization) length ξ of the electron gas diverges algebraically: $\xi \propto |\Delta\nu_B|^{-1/\nu}$. The critical indices κ and ν are a major objective of experimental research [19–22], and the results have been discussed extensively and in many places [1, 4, 6, 14].

Next, we consider $\theta \approx 0$, which is entirely different. This happens when the Fermi energy is located at the tail end of the Landau bands corresponding to the center of the quantum Hall plateau. The bare parameter σ_{xx} of the theory is now close to zero [4]. This means that the T dependence is determined by the strong coupling asymptotic of the renormalization (θ, $\sigma_{xx} \longrightarrow 0$). Notice that the γ_z function (Eqs. (18)–(22)) indicates that the singlet interaction term S_F eventually becomes irrelevant as compared to the Coulomb term S_U (with $U^{-1}(q) = \Gamma|q|$) which, as we mentioned before, is not affected by the quantum theory. One now expects S_U to become the dominant infrared regulator such that the scaling variable X in Eq. (24) is now given by $X = T\Gamma\xi$.

This asymptotic limit of the theory can be identified as the Effros–Shklovskii regime of *variable range hopping* for which the following result is known: $\sigma'_{xx} = \sigma_{xx}(T\Gamma\xi) = \exp(-2/\sqrt{T\Gamma\xi})$ [14]. We therefore conclude that the dynamics of the electron gas is generally described by distinctly different physical processes and controlled by completely different fixed points in the theory.

This work was completed during a visit to the Indian Institute of Science, Bangalore, India by one of the authors (A.M.M.P.). The research was funded in part by the Dutch Science Foundation FOM, INTAS (Grant for Basic Research no. 99-1070), the Russian Science Support Foundation, and the Russian Ministry of Education and Science.

REFERENCES

1. A. M. M. Pruisken and M. A. Baranov, Europhys. Lett. **31**, 543 (1995), and references therein.
2. A. M. M. Pruisken, M. A. Baranov, and B. Škorić, Phys. Rev. B **60**, 16 807 (1999).
3. M. A. Baranov, A. M. M. Pruisken, and B. Škorić, Phys. Rev. B **60**, 16 821 (1999).
4. A. M. M. Pruisken, B. Škorić, and M. A. Baranov, Phys. Rev. B **60**, 16 838 (1999).
5. B. Škorić and A. M. M. Pruisken, Nucl. Phys. B **559**, 637 (1999).
6. M. A. Baranov, I. S. Burmistrov, and A. M. M. Pruisken, Phys. Rev. B **66**, 075317 (2002).
7. A. M. M. Pruisken, Phys. Rev. Lett. **61**, 1297 (1988).
8. A. M. Finkelstein, Pis'ma Zh. Éksp. Teor. Fiz. **37**, 436 (1983) [JETP Lett. **37**, 517 (1983)]; Zh. Éksp. Teor. Fiz. **86**, 367 (1984) [Sov. Phys. JETP **59**, 212 (1984)]; Physica B (Amsterdam) **197**, 636 (1994).
9. C. Castellani, C. Di Castro, P. A. Lee, and M. Ma, Phys. Rev. B **30**, 527 (1984).
10. For a recent review see A. M. M. Pruisken and I. S. Burmistrov, Ann. Phys. (N.Y.) **316**, 285 (2005).
11. See, e.g., *Composite Fermions*, Ed. by O. Heinonen (World Sci., Singapore, 1998).
12. J. K. Jain, Phys. Rev. Lett. **63**, 199 (1989).
13. A. M. M. Pruisken, M. A. Baranov, and M. Voropaev, cond-mat/0206011 (unpublished).
14. See, e.g., D. G. Polyakov and B. I. Shklovskii, Phys. Rev. Lett. **73**, 1150 (1994). Their idea of "one parameter scaling," however, is in conflict with our results.
15. D. Pines and P. Noziéres, *Theory of Quantum Liquids* (Benjamin, New York, 1966; Mir, Moscow, 1967).
16. E. Brezin, S. Hikami, and J. Zinn-Justin, Nucl. Phys. B **165**, 528 (1980).
17. A. M. M. Pruisken, Phys. Rev. B **31**, 416 (1985).
18. I. S. Burmistrov, M. A. Baranov, and A. M. M. Pruisken (unpublished).
19. H. P. Wei, D. C. Tsui, M. A. Palaanen, and A. M. M. Pruisken, Phys. Rev. Lett. **61**, 1294 (1988).
20. R. T. F. van Schaijk, A. de Visser, S. M. Olsthoorn, *et al.*, Phys. Rev. Lett. **84**, 1567 (2000).
21. D. T. N. de Lang, L. A. Ponomarenko, A. de Visser, *et al.*, Physica E (Amsterdam) **12**, 666 (2002).
22. A. M. M. Pruisken, D. T. N. de Lang, L. A. Ponomarenko, and A. de Visser, cond-mat/0109043 (unpublished).
23. A. M. M. Pruisken, M. A. Baranov, and M. Voropaev, cond-mat/0101003 (unpublished).
24. A. M. M. Pruisken and I. S. Burmistrov, cond-mat/0502488 (unpublished).

JETP Letters, Vol. 82, No. 3, 2005, pp. 155–159. Translated from Pis'ma v Zhurnal Éksperimental'noĭ i Teoreticheskoĭ Fiziki, Vol. 82, No. 3, 2005, pp. 171–175.
Original Russian Text Copyright © 2005 by Zaĭtsev.

Ferromagnetism of Metallic Compounds with the Perovskite Structure

R. O. Zaĭtsev
Russian Research Centre Kurchatov Institute, pl. Kurchatova 1, Moscow, 123182 Russia
e-mail: agydel@veernet.ru

Received May 24, 2005; in final form, June 30, 2005

On the basis of the concept of strong interaction in one unit cell, it is stated that ferromagnetic instability can occur in a system with hops between oxygen anions and transition metal (Me) cations in $A_{1-x}B_xMeO_3$ compounds. A phase diagram is constructed to describe the occurrence of ferromagnetic ordering as a function of the average number of holes ($h_{t,d}$) and (h_p) in the low-spin t_{2g}^6 or high-spin $3d^{10}$ shell of the transition metal and in the $2p^6$ shells of O^{2-}. © *2005 Pleiades Publishing, Inc.*

PACS numbers: 71.10.–w, 75.50.Cc

In this work, electronic properties of the simplest metallic compounds with the $A_{1-x}B_xMeO_3$ perovskite structure are studied. Here, A and B are cations of different valence with incompletely filled outer shells, which are located at the cube center. Magnetic properties are studied based on the generalized Hubbard model in which the lowest energy states with a maximum spin are used as a zero approximation and splitting by the total orbital moment is not taken into account.

In the metallic phase, the long-range part of the Coulomb and exchange interactions is substantially screened, so that only transitions between the nearest neighbors caused by the overlap of wave functions are taken into account below. Correspondingly, the Hamiltonian takes the form

$$\hat{H} = \sum_{\mathbf{r},\mathbf{r}'} V^{\alpha,k}(\mathbf{r},\mathbf{r}')\{\hat{d}^{+}_{\alpha,\sigma}(\mathbf{r})\hat{p}_{k,\sigma}(\mathbf{r}') + \text{h.c.}\} + \sum_{\mathbf{r},\sigma}(\epsilon_d - \sigma H)\hat{d}^{+}_{\alpha,\sigma}(\mathbf{r})\hat{d}_{\alpha,\sigma}(\mathbf{r}) + \sum_{\mathbf{r},\sigma}(\epsilon_p - \sigma H)\hat{p}^{+}_{k,\sigma}(\mathbf{r})\hat{p}_{k,\sigma}(\mathbf{r}). \quad (1)$$

Here, indices α run over the values that correspond to five degenerate $3d$-electron states of the transition cation and indices k run over three values that correspond to three degenerate p states of the oxygen anions.

One-particle energies $\epsilon_{p,d}$ are considered to be prescribed energy parameters. The magnetic phase diagram will be calculated for all possible values of ϵ_p and ϵ_d.

The overlap integral matrices $V^{\alpha,k}(\mathbf{r},\mathbf{r}')$ are the same as in the tight-binding approximation for the given crystal lattice. In this case, it is assumed that the transitions occur with no change in the sign of the spin projection $\sigma = \pm$.

For a given arrangement of the lowest atomic multiplet states, the collectivization of the transitions between ($N-1$)- and N-particle states is determined by the poles of the one-particle Green's function. To calculate this function, the creation and annihilation operators will be expanded in terms of Hubbard X operators

$$\hat{d}^{+}_{\alpha,\sigma}(\mathbf{r}) = \sum_{\boldsymbol{\beta}} b_{\boldsymbol{\beta}}(\alpha,\sigma)\hat{X}^{\boldsymbol{\beta}}_{\mathbf{r}}; \qquad \hat{p}^{+}_{k,\sigma}(\mathbf{r}) = \sum_{\boldsymbol{\upsilon}} g_{\boldsymbol{\upsilon}}(k,\sigma)\hat{Y}^{\boldsymbol{\upsilon}}_{\mathbf{r}}. \quad (2)$$

Here, $\boldsymbol{\beta}$ and $\boldsymbol{\upsilon}$ are the numbers of one-particle d- and p-transitions; $b_{\boldsymbol{\beta}}$ and $b_{\boldsymbol{\upsilon}}$ are so-called fractional parentage coefficients, which will be found for each particular transition type.

In the end, it is necessary to calculate the mean occupation number of each multiplet component as a function of the applied magnetic field H.

Below, a one-loop approximation is used, which is a generalization of the zero-loop approximation known in the literature as the Hubbard I approximation [1]. In the zero-loop approximation, each self-energy part of the one-particle Green's function is determined by the so-called terminal factor $f_{\boldsymbol{\beta}}$ equal to the sum of the occupation numbers of the initial and final states corresponding to the given transition $\boldsymbol{\beta}$.

The one-loop approximation involves taking into account the self-energy parts, which, in this approximation, are independent of both the momentum and the frequency and depend on the magnetic field through the one-particle Green's function. The total Green's function $\hat{D}_\omega(\mathbf{q})$ is the product of the virtual Green's function $G_\omega^{\boldsymbol{\alpha},\boldsymbol{\upsilon}}(\mathbf{q})$ by the terminal factor $f_{\boldsymbol{\upsilon}}$. The virtual Green's function itself fulfills the Dyson equation

$$\begin{aligned} D_\omega^{\boldsymbol{\alpha},\boldsymbol{\upsilon}}(\mathbf{q}) &= G_\omega^{\boldsymbol{\alpha},\boldsymbol{\upsilon}}(\mathbf{q}) f(\boldsymbol{\upsilon}), \\ \hat{G}_\omega^{-1}(\mathbf{q}) &= (\hat{G}_\omega^{(0)})^{-1} - \hat{W} - \hat{\Sigma}. \end{aligned} \tag{3}$$

The matrix elements of $\hat{W}$ are determined through the fractional parentage coefficients (Eq. (2)) of the creation and annihilation operators after their substitution into the Hamiltonian (Eq. (1))

$$W_{\boldsymbol{\beta},\boldsymbol{\upsilon}}(\mathbf{q}) = f_{\boldsymbol{\beta}} \sum_{\alpha,k} g_{\boldsymbol{\beta}}(\alpha) \sum_k V^{\alpha,k}(\mathbf{q}) g_{\boldsymbol{\upsilon}}(k). \tag{4}$$

In the chosen one-loop approximation, the self-energy parts are expressed through the products of the matrix elements of the kinematic interaction by the off-diagonal components of the one-particle Green's function summed over momenta and frequencies:

$$\Sigma_{\boldsymbol{\alpha}} = A_{\boldsymbol{\alpha},\boldsymbol{\beta}} Y_{\boldsymbol{\beta}}^{\sigma} + B_{\boldsymbol{\alpha},\boldsymbol{\beta}} Y_{\boldsymbol{\beta}}^{-\sigma}. \tag{5}$$

Here, $A_{\boldsymbol{\alpha},\boldsymbol{\beta}}$ and $B_{\boldsymbol{\alpha},\boldsymbol{\beta}}$ are specified numerical matrices corresponding to the transition amplitudes of the kinematic interaction [2, 3]. The $Y_{\boldsymbol{\beta}}^{\sigma}$ functions have the following general form:

$$\begin{aligned} Y_{\boldsymbol{\beta}}^{\sigma} &= T \sum_{\omega,\mathbf{p},\boldsymbol{\gamma}} L_{\boldsymbol{\beta},\boldsymbol{\gamma}}(\mathbf{q}) (G_\omega(\mathbf{p}))_{\boldsymbol{\beta}}^{\boldsymbol{\gamma}}, \\ L_{\boldsymbol{\beta},\boldsymbol{\gamma}}(\mathbf{q}) &= \sum_{\boldsymbol{\alpha},k} g_{\boldsymbol{\beta}}(\alpha) \sum_k V^{\alpha,k}(\mathbf{q}) g_{\boldsymbol{\gamma}}(k). \end{aligned} \tag{6}$$

All possible N-particle occupation numbers corresponding to the $\boldsymbol{\alpha}((N-1)_k, (N)_s)$ transition at a given temperature T and a given chemical potential are calculated through diagonal matrix elements of the one-particle Green's function using the following general equation:

$$\begin{aligned} n_N(s) &= T \sum_{\omega,\mathbf{q}} \exp(i\omega\delta) D_\omega^{\boldsymbol{\alpha},-\boldsymbol{\alpha}}(\mathbf{q}), \\ \delta &= 0+, \quad \omega = (2n+1)\pi T. \end{aligned} \tag{7}$$

Here, the symbol $-\boldsymbol{\alpha}$ designates the number of the transition inverse with respect to $\boldsymbol{\alpha}$.

The right-hand side of Eq. (7) can be determined using Eqs. (3)–(5) through terminal factors and self-energy parts entering into the definition of Green's functions (Eq. (3)).

The mean occupation numbers can be expressed through terminal factors and self-energy parts, so that a closed system of equations can be obtained for the variations of all terminal factors as functions of the magnetic field.

Finally, equations can be obtained for the calculation of the magnetic permeability as a function of temperature and the mean number of holes h_d and h_p per unit cell.

Ferromagnetic instability is determined from the condition of the occurrence of an infinite spin magnetic susceptibility.

In the limit of $H = 0$, the equations of state are written through the diagonal components of the virtual Green's function $G_\omega^{(kk)}(\mathbf{q})$, which, in turn, are expressed through the normal coordinates $A^{(\pm\lambda)}(\mathbf{q})$ and the hopping integral for the nearest neighbors (t):

$$h_d = [h_d] + R_d f_d K_d, \quad h_p = [h_p] + z f_p K_p, \tag{8}$$

$$\begin{aligned} K_p &= 2n_F(\epsilon_p) + \sum_{\mathbf{q},\lambda=\pm} A_{\mathbf{q}}^{(\lambda)} n_F(\xi_{\mathbf{q}}^{(\lambda)}), \\ K_d &= \sum_{\mathbf{q},\lambda=\pm} A_{\mathbf{q}}^{(-\lambda)} n_F(\xi_{\mathbf{q}}^{(\lambda)}), \end{aligned} \tag{9}$$

$$\begin{aligned} A_{\mathbf{q}}^{(\pm)} &= \frac{1}{2}\left[1 \pm \frac{\operatorname{sgn}(r)}{\sqrt{1 + s(1-\epsilon_{\mathbf{q}})}}\right], \\ z = 1/3, \quad r &= \epsilon_p - \epsilon_d, \quad s = \frac{4t^2 g^2 f_p f_d}{r^2}. \end{aligned} \tag{10}$$

Here, the square brackets $[h_d]$ designate the integer part, R_d designates the degeneracy order of $(1 + [h_d])$ hole states, $f_p = 1 - 5h_p/6$, and $n_F(\epsilon)$ is the Fermi distribution. The R_d and f_d factors and the sums of the fractional parentage coefficients $g^2 \equiv g_d^2 = \sum b_k^2$ are written in the tables below;

$$\begin{aligned} \xi_{\mathbf{q}}^{(\pm)} &= \pm\frac{|r|}{2}\sqrt{1 + s(1-\epsilon_{\mathbf{q}})} - \mu, \\ \mu &= -\frac{1}{2}(\epsilon_p + \epsilon_d), \quad \epsilon_{\mathbf{q}} = \cos(q_x)\cos(q_y). \end{aligned} \tag{11}$$

The one-loop self-energy parts depend on neither the momentum nor the frequency, so that their role at a zero magnetic field is reduced to a correction to the values of r and μ and is not taken into account below.

The condition for the occurrence of ferromagnetic instability is found using the differentiation of the equations of state and the self-energy parts [2, 3]. In the limit of $T = 0$, the general equation for the determination of the boundary between the paramagnetic and ferromagnetic phases takes the following form:

$$\begin{aligned} &K_d(1-K_d)(1-zK_p)R_1(Q) \\ &= V_d f_p (1 - zK_p)[g^2(\Gamma_d + K_d) f_d R_1(Q) \\ &\quad + zK_d(1-K_d)R_3(Q)] \end{aligned}$$

$$
\begin{aligned}
&+g^2V_pf_dK_d(1-K_d)[1+z(f_p-K_p)]R_1(Q)\\
&-g^2zV_d^2f_df_p^2(1-zK_p)R_3(Q)(\Gamma_d+K_d)\\
&-V_p^2zg^4f_pf_d^2K_d(1-K_d)R_1(Q) \qquad (12)\\
&-g^2V_pV_d[g^2(1-zK_p)(\Gamma_d+K_d)R_1(Q)\\
&+z^2K_d(1-K_d)f_pR_3(Q)]\\
&+zg^2K_d(1-K_d)f_pf_d[zE_{pd}W_2R_3(Q)\\
&+g^2W_4E_{2d}f_dR_1(Q)]\\
&+g^2(1-zK_p)f_pf_d(\Gamma_d+K_d)[g^2f_dE_{pd}W_2R_1(Q)\\
&+zf_pW_4E_{2p}R_2(Q)]+\beta zCW_4f_p^2f_d(1-zK_p).
\end{aligned}
$$

Here, $z = 1/3$; Γ_d, β, and $R_k(Q)$ are dimensionless scattering amplitudes calculated for each integer interval of the mean occupation numbers h_d, which are written in the tables below;

$$V_d = f_d\frac{\delta K_d}{\delta f_d} = T\sum_{\omega,\mathbf{q}}\frac{E_pt_{\mathbf{q}}^2}{(E_pE_d-\nu|t_{\mathbf{q}}|^2)^2},$$

$$V_p = f_p\frac{\delta K_p}{\delta f_p} = T\sum_{\omega,\mathbf{q}}\frac{E_dt_{\mathbf{q}}^2}{(E_pE_d-\nu|t_{\mathbf{q}}|^2)^2},$$

$$\omega = \pi T(2n+1),$$

$$E_{pd} = T\sum_{\omega,\mathbf{q}}\frac{E_pE_d}{(E_pE_d-\nu|t_{\mathbf{q}}|^2)^2},$$

$$W_k = T\sum_{\omega,\mathbf{q}}\frac{t_{\mathbf{q}}^k}{(E_pE_d-\nu|t_{\mathbf{q}}|^2)^2},\quad E_{p,d} = i\omega-\epsilon_{p,d}, \qquad (13)$$

$$E_{2d} = \frac{\delta K_p}{\delta\epsilon_p} = T\sum_{\omega,\mathbf{q}}\frac{E_t^2}{(E_pE_d-\nu|t_{\mathbf{q}}|^2)^2},$$

$$E_{2p} = \frac{\delta K_d}{\delta\epsilon_d} = T\sum_{\omega,\mathbf{q}}\frac{E_p^2}{(E_pE_d-\nu|t_{\mathbf{q}}|^2)^2},$$

$$C = T\sum_{\omega,\mathbf{q}}\frac{E_p}{E_d(E_pE_d-\nu|t_{\mathbf{q}}|^2)},$$

$$Q = \frac{[K_d-n_F(\epsilon_d)]}{g^2f_d},\quad \nu = g^2f_df_p;$$

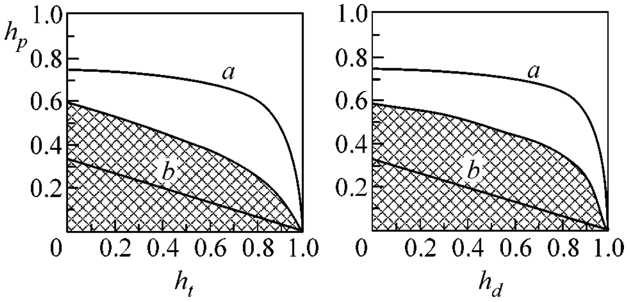

Fig. 1. Magnetic phase diagram at $T = 0$; the ferromagnetic areas are shaded; the calculations were performed in the flat band approximation; (*a*) the filling boundary of the lower subband and (*b*) the electroneutrality line $3h_p + h_{t,d} = \max\{h_{t,d}\}$.

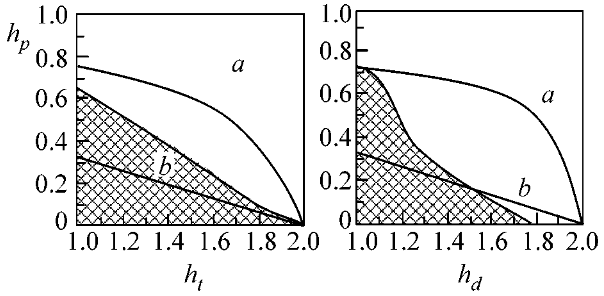

Fig. 2. Magnetic phase diagram at $T = 0$. The designations are the same as in Fig. 1.

and $g^2 = \sum b_k^2$ is the sum of squares of fractional parentage coefficients calculated with regard to the degeneracy order for a specified group of selected transitions.

The condition for ferromagnetic instability establishes a functional relation between the ϵ_p and ϵ_d energy parameters. The substitution of this dependence into the equations of state allows the phase boundary to be determined in the (h_p, h_d) variables (see Figs. 1–5).

In the simplest case of $0 < h_d < 1$ and $0 < h_p < 1$, when the system resonates between the zero-hole and one-hole states, the following set of coefficients is obtained:

Table 1a (t_{2g} states)

g^2	R_d	f_d	Γ_d	$R_{1,2,3}(Q)$	β
1	6	$1 - 5h_d/6$	0	1	0

Table 1b (3*d* states)

g^2	R_d	f_d	Γ_d	$R_{1,2,3}(Q)$	β
1	10	$1 - 9h_d/10$	0	1	0

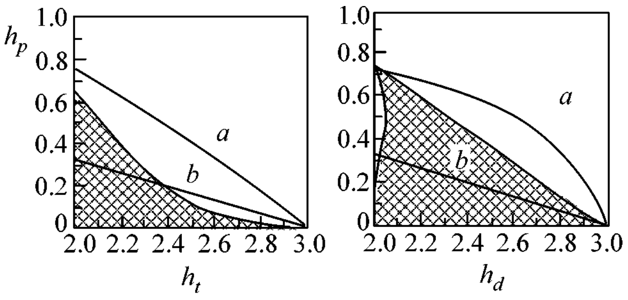

Fig. 3. Magnetic phase diagram at $T = 0$. The designations are the same as in Fig. 1.

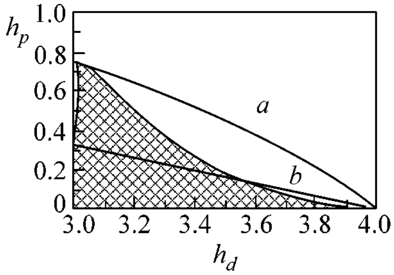

Fig. 4. Magnetic phase diagram at $T = 0$. The designations are the same as in Fig. 1.

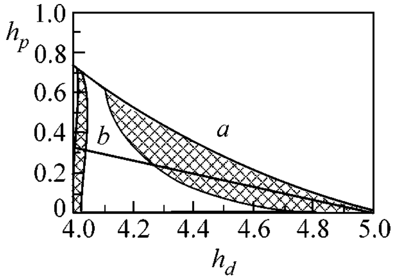

Fig. 5. Magnetic phase diagram at $T = 0$. The designations are the same as in Fig. 1.

Substituting these coefficients into the general equation (12) and also into the equations of state (9) yields the phase diagrams displayed in Fig. 1. The left-hand part of the figure relates to the low-spin t_{2g} states, and the right-hand part relates to the high-spin $3d$ states. The straight lines b are the electroneutrality lines $3h_p + h_{t,\,d} = 1$; curves a are the filling boundaries of the lower subband.

It is seen in Fig. 1 that the proposed mechanism of the occurrence of ferromagnetism corresponds to the Zener concept. According to this theory, the energy preference of states with unidirectional spins occurs if the jump to a neighboring cell proceeds with no change in the spin projection. However, with increasing energy of relative motion, the scattering amplitude of excitations with opposite spins changes its sign, which leads to the appearance of a boundary concentration starting with which the system remains paramagnetic at all temperatures (see Fig. 1).

In the case of $1 < h_d < 2$ and $0 < h_p < 1$, when the properties of the d system are determined by the transitions between one-hole and two-hole states, the following set of coefficients is obtained:

Table 2a (t_{2g} states)

g^2	R_d	f_d	Γ_d	$R_1(Q)$	$R_2(Q)$	$R_3(Q)$	β
3	9	$(4 - h_d)/18$	1/3	1	1	1	0

Table 2b (3*d* states)

g^2	R_d	f_d	Γ_d	$R_1(Q)$	$R_{2,\,3}(Q)$	β
6	30	$(5 - 2h_d)/30$	1/3	$3 + 14zQ$	$1 + 6zQ$	8

With the use of these coefficients and the main equation (12), the phase diagrams depicted in Fig. 2 are obtained.

The substantial difference between the left-hand (t_{2g} states) and right-hand (3*d* states) diagrams is due to the presence of the resonance term ~*C*, which has a logarithmic singularity. In the low-spin part of the phase diagram, electroneutrality line *b* corresponds to the $La^{3+}Mn^{3+}O_3^{2-}$ and $Sr^{2+}Ru^{4+}O_3^{2-}$ compounds, which exhibit ferromagnetic properties when exist in the undistorted cubic phase [4]. The $Bi^{3+}Mn^{3+}O_3^{2-}$, $Sr^{2+}Fe^{4+}O_3^{2-}$, and $Ba^{2+}Fe^{4+}O_3^{2-}$ orthoferrites, which have low transition temperatures (103, 160, and 180 K [5]) are also located in this line.

In the case of $2 < h_d < 3$ and $0 < h_p < 1$, when the *d* excitations are determined by the transitions between two-hole and three-hole states, the following coefficients are obtained:

Table 3a (t_{2g} states)

g^2	R_d	f_d	Γ_d	$R_1(Q)$	$R_{2,\,3}(Q)$	β
2	4	$(5h_d - 6)/36$	2/3	$9 - 2zQ$	$13 + 6zQ$	$-40/3$

Table 3b (3*d* states)

g^2	R_d	f_d	Γ_d	$R_1(Q)$	$R_{2,\,3}(Q)$	β
12	40	$(6 - h_d)/120$	2/3	1	1	0

With the use of these coefficients and Eq. (12), the phase diagrams shown in Fig. 3 are obtained.

The qualitative difference between the left-hand and right-hand diagrams is due to the occurrence of resonant scattering ($\beta \neq 0$), which is manifested in this case only in low-spin t_{2g} states. In accordance with this, the electroneutrality line $3h_p + h_t = 3$ crosses the ferromagnetic area in the restricted interval $2 < h_t < 2.4$. This circumstance agrees with the experimentally observed ferromagnetism of the $La_{1-x}Ca_xMnO_3$ and $La_{1-x}Sr_xMnO_3$ compounds, which is manifested only in a restricted doping range ($0 < x < 0.5$) [6].

In the high-spin part of the phase diagram, for which $\beta = 0$, the electroneutrality line crosses the ferromagnetic area in the entire range of concentrations h_d.

In the region $3 < h_t < 6$ and $0 < h_p < 1$, the contributions of the t_{2g} electrons and the $2p$ holes compensate each other, which leads to the absence of ferromagnetism.

In the case of $3 < h_d < 4$ and $0 < h_p < 1$, when the properties of the d system are determined by the transitions between three- and four-hole states, the following coefficients are obtained:

Table 4 (3*d* states)

g^2	R_d	f_d	Γ_d	$R_1(Q)$	$R_2(Q)$	$R_3(Q)$	β
10	25	$(3h_d - 4)/200$	1	1	$7 + 6zQ$	$3 + 2zQ$	–10

The corresponding phase diagram is shown in Fig. 4.

The electroneutrality line $3h_p + h_d = 4$ corresponds to the ferromagnetic $LaCoO_3$ and $FeTiO_3$ compounds [4, 6].

In the case of $4 < h_d < 5$ and $0 < h_p < 1$, when the properties of the d system are determined by the transitions between four- and five-hole states, the following coefficients are obtained:

Table 5 (3*d* states)

g^2	R_d	f_d	Γ_d	$R_1(Q)$	$R_{2,3}(Q)$	β
3	6	$(19h_d - 70)/150$	4/3	$15 - 26zQ$	$31 + 6zQ$	–112

The corresponding phase diagram is depicted in Fig. 5. In this case, Eq. (12) contains a resonance term with a large coefficient $|\beta| = 112$. For this reason, the electroneutrality line $3h_p + h_d = 5$ only partially crosses the ferromagnetic area (see Fig. 5). The ferromagnetic $LaFeO_3$ and $MnTiO_3$ compounds are located along this line.

In the remaining area of concentrations, $5 < h_d < 10$ and $0 < h_p < 1$, ferromagnetism is absent because of the substantial compensation of the contributions from the $3d$ electrons and the $2p$ holes.

Thus, in the generalized Hubbard model with strong electron–electron repulsion, the phase diagram is determined by the energy dependence of the amplitude of the kinematic interaction [2, 3]. At a small excitation energy, the amplitude of scattering with opposite spins has the positive sign, so that ferromagnetism exists in the region of a small number of holes. However, with increasing energy, the scattering amplitude decreases, which leads to the appearance of a critical concentration starting with which the system remains paramagnetic even at $T = 0$. If the transition element cations have $S > 1/2$, then resonant scattering by the local level with the energy ϵ_d adjacent to the upper edge of the lower hybridization band appears in the system. In this case, the amplitude has a logarithmic singularity of the Kondo type.

As a result, a qualitative change in the magnetic phase diagram occurs at $4 < h_d < 5$. In the region of finite concentrations, a rather wide ferromagnetic region appears, while the system remains paramagnetic in the intermediate region.

For the intermediate concentrations, $2 < h_t < 3$ and $1 < h_d < 4$, the effect of resonant scattering is reduced to a decrease in the ferromagnetic part of the phase diagram due to an increase in its paramagnetic part.

REFERENCES

1. J. Hubbard, Proc. R. Soc. London, Ser. A **277**, 237 (1964).
2. R. O. Zaĭtsev, Zh. Éksp. Teor. Fiz. **123**, 325 (2003) [JETP **96**, 286 (2003)].
3. R. O. Zaĭtsev, *Diagram Methods in the Theory of Superconductivity and Ferromagnetism* (URSS, Moscow, 2004) [in Russian].
4. S. Methfessel and D. C. Mattis, *Magnetic Semiconductors* (Springer, Heidelberg, 1968; Mir, Moscow, 1972).
5. S. Chikasumi, *The Physics of Ferromagnetism* (Syokabo, Tokyo, 1980; Mir, Moscow, 1983).
6. J. B. Goodenough, *Magnetism and the Chemical Bond* (Interscience, New York, 1963; Metallurgiya, Moscow, 1968).

Translated by A. Bagatur'yants

JETP Letters, Vol. 82, No. 3, 2005, pp. 160–163. Translated from Pis'ma v Zhurnal Éksperimental'noĭ i Teoreticheskoĭ Fiziki, Vol. 82, No. 3, 2005, pp. 176–179.
Original Russian Text Copyright © 2005 by Koronovskiĭ, Hramov, Khramova.

Synchronous Behavior of Coupled Systems with Discrete Time

A. A. Koronovskiĭ*, A. E. Hramov, and A. E. Khramova
Faculty of Nonlinear Processes, Saratov State University, Saratov, 410012 Russia
** e-mail: alkor@cas.ssu.runnet.ru*

Received May 25, 2005

The dynamics of one-way coupled systems with discrete time is considered. The behavior of the coupled logistic maps is compared to the dynamics of maps obtained using the Poincaré sectioning procedure applied to the coupled continuous-time systems in the phase synchronization regime. The behavior (previously considered as asynchronous) of the coupled maps that appears when the complete synchronization regime is broken as the coupling parameter decreases, corresponds to the phase synchronization of flow systems, and should be considered as a synchronous regime. A quantitative measure of the degree of synchronism for the interacting systems with discrete time is proposed. *© 2005 Pleiades Publishing, Inc.*

PACS numbers: 05.45.Tp, 05.45.Xt

The process of chaotic synchronization of dynamical systems is among the basic nonlinear phenomena extensively studied in recent years, and this process is also of considerable practical significance. The chaotic synchronization can be considered in systems with both discrete time (maps) and continuous time (flows). Although the two classes of dynamical systems are closely interrelated (it is well known that the systems with continuous time can be reduced to maps using the Poincaré sectioning procedure), there are substantial differences between such systems, which accounts for the fact that the phenomena of synchronization of flows and maps are described using different terms and notions [1].

Evidently, various types of synchronous behavior observed in flows and maps must be interrelated. The aim of this study was to compare the behavior of coupled chaotic systems with continuous time to the dynamics of coupled maps. In particular, it will be demonstrated that the regime of oscillations in coupled maps, which has been considered until recently as asynchronous [2], in fact exhibits signs of synchronism and corresponds to the phase synchronization regime in flow systems [1, 3].

As is known, two coupled identical systems with discrete time at a sufficiently large coupling parameter are featuring the regime of complete (identical) synchronization, whereby the states of these systems coincide. The influence of non-identical features on the regime of complete synchronization was considered in [4]. As the coupling parameter decreases, the saddle orbits built in the synchronous attractor of coupled systems lose stability in the transverse direction, and eventually the regime of complete synchronization (or lag synchronization in flow systems) breaks [2, 5–7] and the chaotic attractor also loses stability in the transverse direction.

It should be noted that analogous phenomena have also been observed in coupled flow systems [8, 9]. In the case of interaction between flow systems with slightly different parameters, the regime of complete synchronization is not established and, instead, the process of lag synchronization takes place. Evidently, by applying the procedure of Poincaré sectioning, it is possible to pass from flow systems to discrete maps. Accordingly, the obtained maps will exhibit complete synchronization. Thus, the complete and lag synchronization in flow systems refer to essentially the same type of synchronous behavior, which is consistent with our recent results [10, 11]. For this reason, below we will not distinguish the regimes of complete synchronization and lag synchronization in flow systems and will use the general term "complete synchronization."

As the coupling parameter decreases, the saddle orbits of coupled flow systems (like those of maps) lose stability in the transverse direction and eventually the regime of complete synchronization (or lag synchronization) in these flows breaks [8, 9]. In the maps obtained using the Poincaré sections, the destruction of synchronism proceeds exactly as described above.

Thus, up to the time when the complete synchronization (including the lag synchronization in flow systems) is broken, the synchronous regimes in flows and maps are completely analogous. It should also be noted that, in both flows [12] and maps [5], the destruction of the complete synchronization regime is accompanied by intermittency of the "on–off" type, which is characterized by the corresponding power laws with equal exponents for the systems with continuous and discrete time.

When the regime of complete synchronization between systems with continuous time is broken (as a result of a decrease in the coupling parameter), the sys-

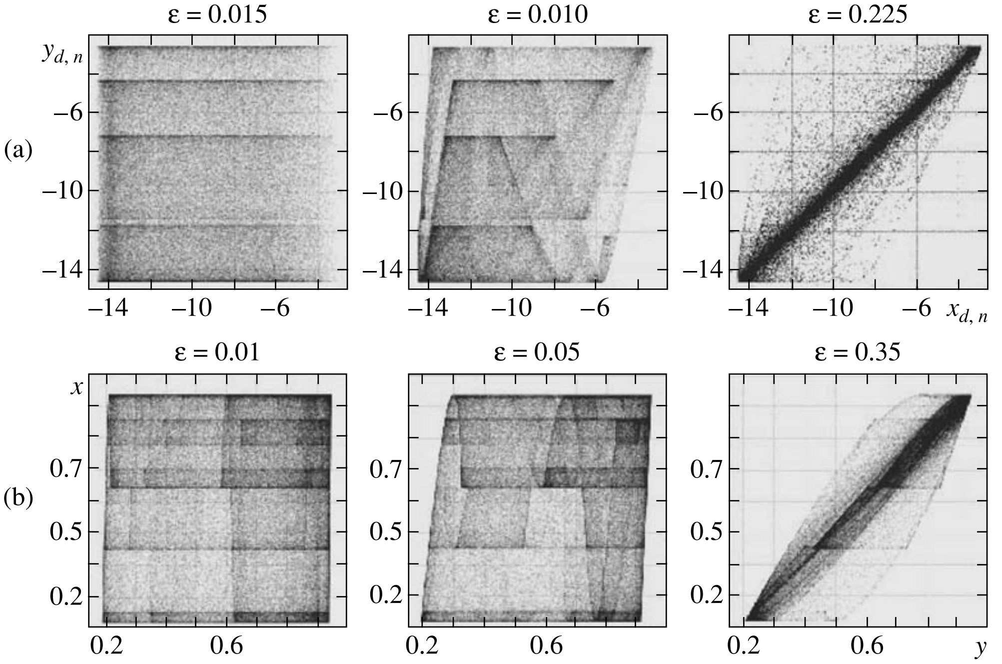

Fig. 1. Behavior of one-way coupled chaotic systems: (a) the states ($x_{d,n}$, $x_{r,n}$) of maps (3) obtained from the Rössler flows (1) by means of the Poincaré sectioning; for the coupling parameter ε = 0.015, the synchronization is absent; for ε = 0.10 and 0.225, the systems exhibit phase synchronization; (b) the states (*x*, *y*) of logistic maps (2) at various values of the coupling parameter ε.

tems pass to a regime of phase synchronization [12], which is a particular case of the time scale synchronization (whereby one part of the time scale is synchronized and the other is not) [10, 11]. At the same time, it is commonly accepted that the destruction of complete synchronization in maps is followed by the onset of asynchronous oscillations. Taking into account that, as was pointed out above, it is always possible to pass from flows to maps with the aid of the Poincaré section, we can pose the following question: "If the systems with continuous time exhibit phase synchronization, why is no such synchronous behavior observed for the maps obtained from these flows using the procedure of Poincaré sectioning?" It is traditionally assumed that this procedure, which reduces the flow systems to maps, excludes numerous states of the system from the consideration (leaving only the states belonging to the surface of the section), so that the residual data are insufficient to recognize the synchronism, and the map dynamics exhibits asynchronous character.

However, as will be shown below, the maps obtained using the Poincaré sections for flow systems occurring in the regime of phase synchronization still carry an "imprint" of the synchronous dynamics and, hence, their behavior has to be considered as synchronized. Moreover, since other discrete maps (e.g., logistic) exhibit generally the same behavior as the maps obtained using the Poincaré sections from flow systems, their dynamics (previously considered as asynchronous) exhibits the features of synchronous behavior and should be considered as synchronized.

The above consideration will be illustrated using a model representing one-way coupled Rössler systems with slightly mismatched parameters:

$$\begin{aligned}\dot{x}_d &= -\omega_d y_d - z_d, \quad \dot{x}_r = -\omega_r y_r - z_r + \varepsilon(x_d - x_r),\\ \dot{y}_d &= \omega_d x_d + a y_d, \quad \dot{y}_r = \omega_r x_r + a y_r,\\ \dot{z}_d &= p + z_d(x_d - c), \quad \dot{z}_r = p + z_r(x_r - c),\end{aligned} \tag{1}$$

where ε is the coupling parameter. The values of the control parameters are selected by analogy with those used in [13]: $a = 0.15$, $p = 0.2$, $c = 10.0$, $\omega_r = 0.95$, $\omega_d = 0.93$. We also consider the logistic maps

$$\begin{aligned}x_{n+1} &= f(x_n, \lambda_x),\\ y_{n+1} &= f(y_n, \lambda_y) + \varepsilon(f(x_n, \lambda_x) - f(y_n, \lambda_y)),\end{aligned} \tag{2}$$

where ε is also the coupling parameter, $f(x, \lambda) = \lambda x(1 - x)$, $\lambda_x = 3.75$, and $\lambda_y = 3.79$. Using sections of the phase flow by the Poincaré surfaces $y_d = 0$, $\dot{y}_d < 0$ and $y_r = 0$, $\dot{y}_r < 0$, the drive and response systems with continuous time (1) were reduced to the following coupled two-dimensional maps:

$$\begin{aligned}x_{d,n+1} &= F_x(x_{d,n}, z_{d,n}, \omega_d),\\ z_{d,n+1} &= F_z(x_{d,n}, z_{d,n}, \omega_d),\\ x_{r,n+1} &= G_x(x_{r,n}, z_{r,n}, x_{d,n}, z_{d,n}, \omega_d, \varepsilon),\\ z_{r,n+1} &= G_z(x_{r,n}, z_{r,n}, x_{d,n}, z_{d,n}, \omega_d, \varepsilon).\end{aligned} \tag{3}$$

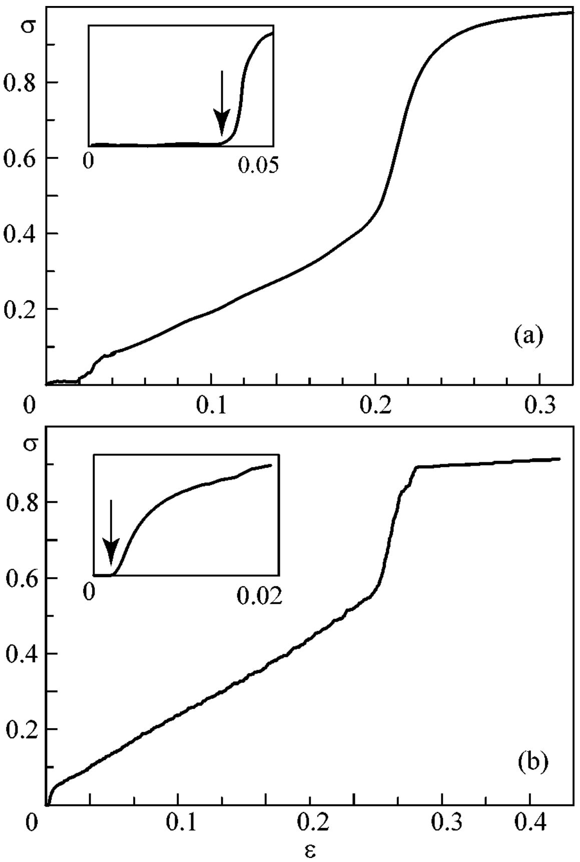

Fig. 2. Plots of the geometric measure of synchronism σ(ε) for (a) maps (3) obtained from the Rössler flows (1) by means of the Poincaré sectioning and (b) the logistic maps (2). The insets show the behavior of σ(ε) in the vicinity of zero in a greater scale; arrows indicate the onset of phase synchronization in the Rössler systems σ(ε) and the corresponding point for the coupled maps.

A criterion of synchronism in the coupled maps is provided by the condition that the points in the (x_n, y_n) plane adhere to the diagonal $y_n = x_n$ (where x_n and y_n are the states of the interacting maps at the *n*th moment of discrete time. If the behavior of coupled maps corresponds to the $y = x$ diagonal in the (x_n, y_n) plane, the system features the regime of complete synchronization. If the points are scattered over this plane, the regime is asynchronous.

Let us consider the $(x_{d,n}, x_{r,n})$ plane of maps (3) obtained from flows (1) by means of the Poincaré section for various values of the coupling parameter ε (Fig. 1a). For the coupling parameter ε = 0.015 at which the phase synchronization is absent (a threshold for the phase synchronization onset with the given control parameters is $\varepsilon_p \approx 0.04$), the points uniformly fill a square in the $(x_{d,n}, x_{r,n})$ plane. If the phase synchronization takes place (ε = 0.10 and 0.225), the points in the $(x_{d,n}, x_{r,n})$ plane occupy a region having the shape of an irregular quadrangle extended along the $x_r = x_d$ diagonal. The area $S = S(\varepsilon)$ of this region decreases with increasing the coupling parameter, is maximal in the absence of coupling, and tends to zero (the points adhere to the diagonal) in the case of complete synchronization.

Thus, we can introduce the geometric measure defined as

$$\sigma(\varepsilon) = \frac{S(0) - S(\varepsilon)}{S(0)}, \qquad (4)$$

which characterizes the degree of synchronization of the interacting systems, where $S(\varepsilon)$ is the area of a region covered by points in the $(x_{d,n}, x_{r,n})$ plane at a fixed value of the coupling parameter ε.

Figure 2a shows the behavior of σ(ε) for maps (3). As can be seen, σ(ε) is close to zero in the absence of phase synchronization, increases with the coupling parameter in the interval corresponding to the phase synchronization, and tends to unity in the complete synchronization regime. It should be noted that the behavior of the proposed geometric measure of synchronism of the interacting systems is consistent with the energetic measure of synchronism introduced previously [10]. Thus, even using the analysis of maps obtained by means of the Poincaré sectioning, it is possible to form a conclusion on the synchronous behavior in a system despite the fact that a significant part of the information about the behavior of the initial flow system was excluded from the consideration.

Now let us consider the behavior of one-way coupled logistic maps (2). In this case, the initial flow system (such as in the above example) is absent and, hence, it is impossible to judge on the presence (or absence) of phase synchronization. Nevertheless, the behavior of coupled systems with discrete time is completely analogous to the behavior of maps (3) obtained by reduction of the Rössler systems (see Figs. 1b and 2b). A figure covered by points in the (x_n, y_n) plane also has the shape of a quadrangle extended along the $x = y$ diagonal, its area decreases with increasing coupling parameter ε, and the geometric measure of synchronism σ(ε) monotonically grows in a certain interval of ε and tends to unity in the case of complete synchronization. It is also important to note the presence of a certain interval $[0, \varepsilon_p]$ of the coupling parameter where this measure is zero, which corresponds to asynchronous behavior of the maps obtained by reduction of the flow systems (see the insets in Figs. 2a and 2b).

Thus, based on the above considerations, we may conclude that the behavior of the two coupled systems with discrete time observed when the complete synchronization regime is broken as the coupling parameter decreases corresponds to the regime of phase synchronization in slightly non-identical flow systems and has to be considered as a synchronous regime rather than asynchronous as it was commonly accepted until now. Using the proposed quantitative measure of the degree of synchronism in interacting systems, it is possible to unambiguously distinguish the asynchronous behavior of maps from a synchronized regime corresponding to the phase synchronization in coupled flow systems. This approach can be used for the diagnostics of phase synchronism in coupled systems with continuous time.

This study was supported by the Ministry of Education and Science of the Russian Federation (program "Development of Scientific Potential of High School," project no. 333); the Russian Foundation for Basic Research (project no. 05-02-16273); the Council of the President of the Russian Federation for Support of Young Russian Scientists and Leading Scientific Schools (project no. NSh-1250.2003.02); and the Science and Education Center "Nonlinear Dynamics and Biophysics" at the Saratov State University (sponsored by the US Civilian Research and Development Foundation, grant no. REC-006). We also gratefully acknowledge support from the "Dynasty" Foundation and the International Center for Fundamental Physics in Moscow (ICFPM).

REFERENCES

1. S. Boccaletti, J. Kurths, G. Osipov, *et al.*, Phys. Rep. **366**, 1 (2002).
2. V. Astakhov, A. Shabunin, T. Kapitaniak, *et al.*, Phys. Rev. Lett. **79**, 1014 (1997).
3. M. G. Rosenblum, A. S. Pikovsky, and J. Kurths, Phys. Rev. Lett. **76**, 1804 (1996).
4. V. Astakhov, M. Hasler, T. Kapitaniak, *et al.*, Phys. Rev. E **58**, 5620 (1998).
5. P. Ashwin, J. Buescu, and I. Stewart, Nonlinearity **9**, 703 (1996).
6. S. C. Venkataramani, B. R. Hunt, and E. Ott, Phys. Rev. E **54**, 1346 (1996).
7. E. Ott and J. C. Sommerer, Phys. Lett. A **188**, 39 (1994).
8. O. V. Sosnovtseva, A. G. Balanov, T. E. Vadivasova, *et al.*, Phys. Rev. E **60**, 6560 (1999).
9. D. Pazó, M. Zaks, and J. Kurths, Chaos **13**, 309 (2002).
10. A. E. Hramov and A. A. Koronovskii, Chaos **14**, 603 (2004).
11. A. E. Hramov, A. A. Koronovskii, M. K. Kurovskaya, *et al.*, Phys. Rev. E **71**, 056204 (2005).
12. M. G. Rosenblum, A. S. Pikovsky, and J. Kurths, Phys. Rev. Lett. **78**, 4193 (1997).
13. Z. Zheng and G. Hu, Phys. Rev. E **62**, 7882 (2000).

Translated by P. Pozdeev

JETP Letters, Vol. 82, No. 3, 2005, pp. 164–168. Translated from Pis'ma v Zhurnal Éksperimental'noĭ i Teoreticheskoĭ Fiziki, Vol. 82, No. 3, 2005, pp. 180–184.
Original Russian Text Copyright © 2005 by Bogdanov, Galeev, Kulik, Maslennikov, Moreva.

Reconstruction of the Polarization States of a Biphoton Field

Yu. I. Bogdanov[a], R. F. Galeev[b], S. P. Kulik[b], G. A. Maslennikov[b], and E. V. Moreva[c]
[a] *Institute of Physics and Technology, Russian Academy of Sciences, Nakhimovskiĭ pr. 34, Moscow, 117218 Russia*
[b] *Faculty of Physics, Moscow State University, Vorob'evy gory, Moscow, 119899 Russia*
[c] *Moscow Engineering Physics Institute (State University), Kashirskoe sh. 31, Moscow, 115409 Russia*

Received June 7, 2005

A method for reconstructing an arbitrary quantum state of an optical system in Hilbert space with dimension $d = 4$ is discussed. Such states can be realized using a collinear frequency-nondegenerate regime of generating spontaneous parametric down-conversion. The method has been tested for a number of polarization states of a biphoton field. The high accuracy of the reconstruction of the states (above 99%) indicates that the procedures proposed for reconstructing the quantum state of the system are adequate. *© 2005 Pleiades Publishing, Inc.*

PACS numbers: 03.67.Hk, 42.25.Ja, 42.50.Dv

Methods for reconstructing quantum states have been extensively discussed in recent years. First, the properties of such states are studied in the theory of quantum information and quantum calculations. Second, this interest is stimulated by the growing requirements of experimental physics, which is closely approaching manipulation of single quantum objects. We have in mind attempts to control three stages of the evolution of quantum systems: preparation, transformation, and measurement. Quantum optical multilevel systems present a rich class of states that is very attractive for the transmission and storage of quantum information. At present, nearly complete control has apparently been achieved over two-level optical systems—polarization, spatial, and frequency states of single photons. This statement is corroborated by operating devices for quantum key distribution that are based on certain procedures for encoding information using single photons.

At the same time, multilevel states of the field are also of considerable interest [1]. In addition to fundamental aspects, an increase in the dimension is associated with an increase in the security of existing quantum key distribution systems (against certain classes of attacks on quantum key distribution protocols) [2]. A method for complete control over the preparation [3] and measurement [4, 5] of three-level polarization optical systems was recently proposed and realized. Procedures for generating and measuring other three-level optical states are being actively investigated in realization on spatial field modes [6], three-arm interferometers [7], and entangled states of biphotons [8]. Unfactorized states of two qubits based on biphotons were analyzed in detail in [9], where the complete statistical reconstruction (density matrix) of the initial state was realized. The preparation of unfactorized triplet states in four-dimensional Hilbert space on the basis of biphoton field was probably reported for the first time in [10]. The removal of frequency degeneracy was used in [11] to generate a Bell singlet state in a single-beam (wavevector-degenerate) mode.

This paper is devoted to discussing a method for reconstructing an arbitrary state of a four-level quantum system realized on polarization states of a frequency-degenerate biphoton field.

1. BIPHOTONS AS FOUR-LEVEL SYSTEMS

As a result of spontaneous parametric down-conversion in the presence of the action of laser pumping on a crystal without an inversion center, pairs of correlated photons (biphotons) are formed. The sum of the frequencies of photons produced under stationary conditions is equal to the pumping frequency, and the scattering directions satisfy the phase-synchronism conditions [12]: $\omega_1 + \omega_2 = \omega_p$ and $\mathbf{k}_1 + \mathbf{k}_2 = \mathbf{k}_p$. The state vector of the biphoton field in an arbitrary pure polarization state has the form

$$|\Psi\rangle = c_1|H_1, H_2\rangle + c_2|H_1, V_2\rangle + c_3|V_1, H_2\rangle + c_4|V_1, V_2\rangle, \tag{1}$$

where

$$c_i = |c_i|\exp\{i\varphi_i\} \text{ and } \sum_{i=1}^{4}|c_i|^2 = 1$$

and, for example, $|H_1, H_2\rangle$ means that two photons are in the horizontal polarization mode and $|H_1, V_2\rangle$ implies that the photons in modes 1 and 2 have the horizontal and vertical polarizations, respectively.[1] If unpolarized

---

[1] Modes 1 and 2 are traditionally called signal and idler modes, respectively.

modes are degenerate, i.e., $|H_1\rangle = |H_2\rangle = |H\rangle$, $|V_1\rangle = |V_2\rangle = |V\rangle$, then state (1) is transformed to the form

$$|\Psi\rangle = c_1|H, H\rangle + c_2|H, V\rangle + c_4|V, V\rangle, \qquad (2)$$

which corresponds to a three-level optical system or a qutrit [3–5]. Such a regime of generation of biphotons is called collinear and frequency-degenerate. The degeneracy can be removed by various methods. The first method is based on the choice of a crystal orientation such that spontaneous parametric scattering leads to the production of two photons with different frequencies in one spatial mode. The second method is based on the determination of the arrival times of photons with different polarizations, which can be realized by means of delay lines with polarization anisotropy. Since state (1) is represented as the expansion in terms of four basis states, it was called ququart by analogy with qubit and qutrit, which are the states of two- and three-level systems, respectively.[2]

The polarization properties of a two-mode biphoton field are completely determined by the coherence matrix introduced by Klyshko [13]. This matrix consisting of 16 fourth-order moments of the field can be obtained as the product of the coherence matrices of both photons [14] and is written as

$$K_4 = \begin{pmatrix} A & E & F & G \\ E^* & B & I & K \\ F^* & I^* & C & L \\ G^* & K^* & L^* & D \end{pmatrix}. \qquad (3)$$

The diagonal matrix elements are real quantities characterizing the strength of correlations between photons in two frequency–angular modes with parallel $[(K_4)_{11}, (K_4)_{44}]$ or orthogonal $[(K_4)_{22}, (K_4)_{33}]$ polarizations:

$$\begin{aligned} A &= \langle a_1^+ a_2^+ a_1 a_2 \rangle = |c_1|^2, \quad B = \langle a_1^+ b_2^+ a_1 b_2 \rangle = |c_2|^2, \\ C &= \langle b_1^+ a_2^+ b_1 a_2 \rangle = |c_3|^2, \quad D = \langle b_1^+ b_2^+ b_1 b_2 \rangle = |c_4|^2. \end{aligned} \qquad (4)$$

The off-diagonal elements are complex quantities and are determine relative phases between basis states

$$\begin{aligned} E &= \langle a_1^+ a_2^+ a_1 b_2 \rangle = c_1^* c_2, \quad F = \langle a_1^+ a_2^+ b_1 a_2 \rangle = c_1^* c_3, \\ G &= \langle a_1^+ a_2^+ b_1 b_2 \rangle = c_1^* c_4, \quad I = \langle a_1^+ b_2^+ b_1 a_2 \rangle = c_2^* c_3, \qquad (5) \\ K &= \langle a_1^+ b_2^+ b_1 b_2 \rangle = c_2^* c_4, \quad L = \langle b_1^+ a_2^+ b_1 b_2 \rangle = c_3^* c_4. \end{aligned}$$

Here, a^+ (a) and b^+ (b) are the operators of creation (annihilation) of a photon in the horizontal and vertical modes, respectively. For a pure ququart state, the reduced polarization density matrix coincides with coherence matrix (3).

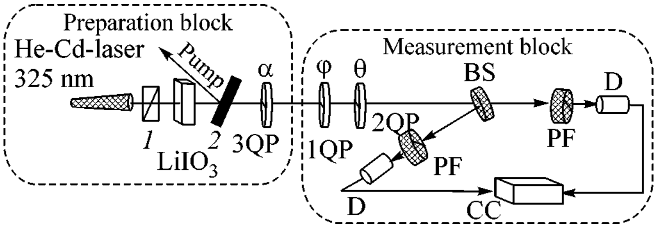

Fig. 1. Layout of the experimental setup for the complete tomography of ququarts: (*1*) horizontally oriented polarizer; (*2*) filter reflecting ultraviolet pumping radiation, (3QP) driving quartz plate, (1QP) and (2QP) quartz plates, (PF) polarization filter, (D) photodetector, and (CC) coincidence scheme. The preparation and measurement blocks are enclosed by the dashed lines.

Three real moments (4) and six complex moments (5) completely determine an arbitrary ququart state. Thus, if all moments are measured, the initial state of the density matrix can be reconstructed. This procedure can be performed by projecting an unknown state on certain states, as is done in medical tomography.[3] The optimum tomography procedure is reduced to finding the minimum set of projectors from which the initial density matrix or state vector can be reconstructed.

In this work, frequency-nondegenerate collinear states of biphotons are investigated. For this reason, the ququart is represented in the form

$$\begin{aligned} |\Psi\rangle &= c_1|H_{\omega_1}, H_{\omega_2}\rangle + c_2|H_{\omega_1}, V_{\omega_2}\rangle \\ &+ c_3|V_{\omega_1}, H_{\omega_2}\rangle + c_4|V_{\omega_1}, V_{\omega_2}\rangle. \end{aligned} \qquad (6)$$

2. EXPERIMENT

An experimental setup for studying an arbitrary ququart (Fig. 1) consists of two blocks, “preparation” and “measurement.”

2.1. The preparation block includes a lithium iodate crystal with length L = 1.5 cm and a driving quartz plate 987.7 μm in thickness. Pumping is the horizontally polarized 325-nm radiation of a He–Cd laser. The angle between the pumping wavevector and optical axis of the crystal is equal to 58°. Under these conditions, the state $|\Psi_0\rangle = |V_{\omega_1}, V_{\omega_2}\rangle$ (type-1 phase matching) is generated in the crystal. The driving phase plate

---

[2] These terms relating to energy states are incompletely correct, because no real “levels” exist in these systems. They imply the expansion of states in orthonormalized bases with two (qubit), three (qutrit), and four (ququart) basis vectors. We also use this accepted terminology.

[3] The corresponding procedure is often called quantum tomography, and the complete set of measurements that provides the reconstruction of the initial state is called the quantum tomography protocol.

transforms the vector $|\Psi_0\rangle$ according to the rule $|\Psi_{\text{in}}\rangle = G|\Psi_0\rangle$, where the matrix

$$G = \begin{pmatrix} t_1t_2 & t_1r_2 & r_1t_2 & r_1r_2 \\ -t_1r_2^* & t_1t_2^* & -r_1r_2^* & r_1t_2^* \\ -r_1^*t_2 & -r_1^*r_2 & t_1^*t_2 & t_1^*r_2 \\ r_1^*r_2^* & -r_1^*t_2^* & -t_1^*r_2^* & t_1^*t_2^* \end{pmatrix} \qquad (7)$$

is the direct product of the matrices describing the polarization transformations for each of photons composing a biphoton. It depends on the complex reflection and transmission coefficients $r_j = i\sin\delta_j\sin2\alpha$ and $t_j = \cos\delta_j + i\sin\delta_j\cos2\alpha$, respectively, where δ_j is the optical thickness of the plate, α is the angle between the optical axis of the plate and vertical, and subscripts $j = 1$ and 2 refer to the photons with frequencies ω_1 and ω_2, respectively. Since the frequencies are nondegenerate, the optical densities of the plate $\delta_j = \pi(n_{ej} - n_{0j})h/\lambda_j$, where h is the geometric thickness of the plate, for the signal and blank photons differ from each other. By varying the angle α, one can modify the matrix G and, therefore, obtain various states of ququart. The photon frequencies are chosen arbitrarily such that they satisfy the relation $\omega_1 + \omega_2 = \omega_p$. In our scheme, in order to choose the frequency of one of the photons, a narrowband filter with the maximum transmission at a wavelength of 635 nm was used. In this case, the wavelength of the conjugate photon was equal to 667.4 nm. The spectral width of each of the photons was determined by the length of the crystal and was equal to 2 nm.

2.2. The measurement block consists of two quartz plates placed in front of the Brown–Twiss scheme with a polarization-insensitive light splitter and polarization filters in both arms. The polarization filters separate the vertical (V) polarization. Counts in each arm are detected by photodetectors pulses from which are directed to a coincidence scheme. The trigger window of the coincidence scheme was $T = 1.7$ ns. A feature of the experimental setup is the absence of filters in front of the detectors. Owing to this feature, each detector is recorded photons with both frequencies. A recorded event is a coincidence-scheme count that occurs when one detector records a photon with the frequency ω_1 and the other detector records a photon with the frequency ω_2. Since the vertical polarization component is separated, projection occurs on the state $|\Psi_{VV}\rangle \equiv |V_{\omega_1}, V_{\omega_2}\rangle$. In the framework of the proposed measurement method, the thickness of plates may be chosen arbitrarily. In our experiment, plates with thicknesses $h_1 = 821.5$ μm and $h_2 = 712$ μm were used.

3. MEASUREMENT PROCEDURE

The joint action of two plates and polarization filters provides the basis for the procedure of projecting the initial (generally unknown) state. The quantum tomography of an arbitrary ququart state is performed by means of the detection of pair coincidences of photocounts of detectors for various positions of the quartz plates. In order to reconstruct the initial state, it is necessary to carry out no less than $d^2 = 16$ measurements of the projections (where $d = 4$ is the dimension of Hil-bert space). This procedure is mathematically expressed as a system of independent linear equations relating combinations of imaginary and real parts of moments (4) and (5) to the number of detected events. Such a system can be obtained by choosing four different positions of the first plate (1QP). Then, for each fixed rotation angle, it is sufficient to conduct four measurements for various angles of the second plate (2QP). However, measurements in the experiment were carried out for a larger number of the second plate. The extra measurements make it possible to increase in the set of statistical data for more accurate reconstruction of the density matrix of the initial state [5].

The transformations made by the plates are expressed in the form

$$|\Psi_{\text{out}}\rangle_{kl} = G(\delta_1, \theta_k)G(\delta_2, \varphi_l)|\Psi_{\text{in}}\rangle, \qquad (8)$$

where φ_l and θ_k are the rotation angles of the first and second plates, respectively. Disregarding the normalization, the number of events detected in the experiment (pair coincidences of the photocounts R_{kl}) is the projection of the transformed state $|\Psi_{\text{out}}\rangle$ onto the state $|\Psi_{VV}\rangle$ determined by the orientation of the polarization filters. This projection is given by the expression $R_{kl} \propto |\langle\Psi_{VV}|\Psi_{\text{out}}\rangle_{kl}|^2$. Thus, the coincidence rate for each run is determined by the rotation angles of the plates 1QP and 2QP.

The experiment was aimed at reconstructing ququart states obtained for several angles of the driving plate. Specifically, the states corresponding to the plate orientation $\alpha = 0$ and 20° are analyzed. For each input state, four measurement runs were conducted. Each run is specified by the plate orientation angle of the 1QP plate $\varphi = 90°$, 105°, 120°, and 135° for the complete rotation of the 2QP plate by 360° with a step of 10°; i.e., it includes 148 measurements. Figure 2 shows the normalized coincidence number for 30 s as a function of the orientation angle of the 2QP plate for $\alpha = 20°$. When processing experimental data, the random coincidence rate N_{ran}, which is expressed in terms of the rate of averaged single counts from each photodetector and the coincidence-window width of the scheme as $N_{\text{ran}} = \langle N_1\rangle\langle N_2\rangle T$, is extracted from the coincidence number.

To compare the reconstructed quantum state with the theoretical one, the fidelity concept is used. For pure states, this quantity is defined as

$$F = |\langle\Psi_{\text{exp}}|\Psi_{\text{theor}}\rangle|^2. \qquad (9)$$

The F value lies in the range from 0 to 1. If the reconstructed state is identical to the theoretical one, $F = 1$. If

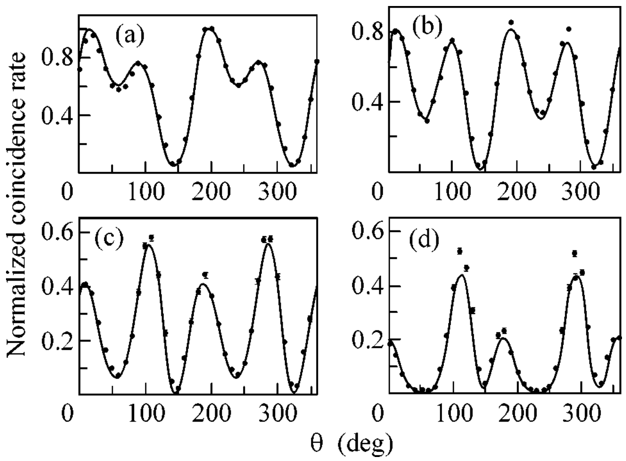

Fig. 2. Normalized coincidence rate vs. the rotation angle of the second quartz plate 2QP for the rotation angles of the first plate (1QP) φ = (a) 90°, (b) 105°, (c) 120°, and (d) 135°. The solid lines are the theoretical calculations.

the states are orthogonal, $F = 0$. To reconstruct the initial state, we used the root approach that was developed in [15, 16] and was successively applied to reconstruct states of optical qutrits [3–5]. When processing the experimental data, we separate two types of errors—instrumental and statistical—that lead to the difference of the reconstructed state from the ideal state. The former errors are caused by the quite rough inclusion of the effect of random coincidences, errors in the specification of the plate rotation angles, error of determination of the optical thickness of the plates, finite width of the biphoton-field spectrum, etc. The latter errors are associated with statistical fluctuations caused by the Poisson character of the detected-event number. As was shown in [5], the effect of statistical fluctuations is negligibly small compared to the effect of instrumental errors if the total number of detected events is much larger than the so-called coherence volume. Numerical calculations show that the coherence volume in a given experimental run is estimated as 2140 on average and does not exceed 4340 with a C.L. of 95%. At the same time, the total number of detected counts in the experiment was 280 000. Thus, errors of the statistical reconstruction of ququart states in the experiment under consideration were associated with instrumental errors.

Results of the statistical processing of experimental data. The left column presents the angle of the quartz plate 3QP specifying the input (reconstructed) state. The second column contains the theoretical (known) components of the prepared vector of state. The third column presents the result of the reconstruction of the state. The fourth column shows the fidelity of the experimental and theoretical values

	State vector		Fidelity
α	theory $\vert\psi\rangle_{\text{theor}} = (c_1, c_2, c_3, c_4)$	experiment $\vert\psi\rangle_{\text{exp}} = (c_1, c_2, c_3, c_4)$	F
0°	0	–0.0555 – 0.0204i	0.996
	0	–0.0059 + 0.005i	
	0	–0.0425 + 0.0052i	
	1	0.9973	
20°	0.8097	0.8067	0.998
	–0.4568 – 0.3527i	–0.4847 – 0.3304i	
	–0.0103 – 0.0859i	0.023 – 0.0554i	
	–0.0316 + 0.0529i	–0.0174 + 0.0413i	

The table presents the results of the measurement of states $|\Psi_{\text{in}}\rangle$. The high values of fidelity F corroborate the applicability of the proposed tomography procedure to the reconstruction of ququart states.

We emphasize that the states $|\Psi_{\text{in}}\rangle$ prepared in the experiment do not cover the entire set of states (1), because they were obtained under separate phase-plate-induced SU(2) transformations (7) of each of the photons composing the biphoton. They present a class of so-called factorized states when $|\Psi\rangle = |\Psi_{\omega_1}\rangle \otimes |\Psi_{\omega_2}\rangle$. However, to verify the applicability of the general reconstruction method, the choice of this class of states is sufficient.

4. CONCLUSIONS

A procedure has been proposed for reconstructing an arbitrary state of a quantum optical system in Hilbert space with the dimension $d = 4$. The procedure was tested in application to pure factorized ququart states, which are obtained as a result of the phase-plate-induced unitary transformation of the polarized state of an initial biphoton. The main feature of this reconstruction method is that a quantum state is subjected to unitary transformation as a whole indivisible object, which can be transmitted both through open space and fiber optic lines.

This work was supported in part by the Russian Foundation for Basic Research (project no. 03-02-16444a) and the Council of the President of the Russian Federation for Support of Young Russian Scientists and Leading Scientific Schools (project no. NSh-166.2003.02).

REFERENCES

1. R. T. Thew, K. Nemoto, A. G. White, and W. J. Munro, Phys. Rev. A **66**, 012303 (2002).
2. H. Bechmann-Pasquinucci and W. Tittel, Phys. Rev. A **61**, 062308 (2000).
3. Yu. I. Bogdanov, M. V. Chekhova, S. P. Kulik, *et al.*, Phys. Rev. Lett. **93**, 230503 (2004).
4. Yu. I. Bogdanov, L. A. Krivitsky, and S. P. Kulik, Pis'ma Zh. Éksp. Teor. Fiz. **78**, 804 (2003) [JETP Lett. **78**, 352 (2003)].
5. Yu. I. Bogdanov, M. V. Chekhova, L. A. Krivitsky, *et al.*, Phys. Rev. A **70**, 042 303 (2004).

6. N. Langford, R. B. Dalton, M. D. Harvey, and J. L. O'Brien, Phys. Rev. Lett. **93**, 053601 (2004).
7. R. T. Thew, A. Acin, H. Zbinden, and N. Gisin, Quantum Inform. Comput. **4**, 93 (2004).
8. J. C. Howell, A. Lamas-Linares, and D. Bouwmeester, Phys. Rev. Lett. **88**, 030401 (2002).
9. D. F. V. James, P. G. Kwiat, W. J. Munro, and A. G. White, Phys. Rev. A **64**, 052312 (2001).
10. Y. H. Kim, S. P. Kulik, and Y. Shih, Phys. Rev. A **63**, 060301 (2001).
11. A. V. Burlakov, S. P. Kulik, Yu. I. Rytikov, and M. V. Chekhova, Zh. Éksp. Teor. Fiz. **122**, 738 (2002) [JETP **95**, 639 (2002)].
12. D. N. Klyshko, *Photons and Nonlinear Optics* (Nauka, Moscow, 1980) [in Russian].
13. D. N. Klyshko, Zh. Éksp. Teor. Fiz. **111**, 1955 (1997) [JETP **84**, 1065 (1997)].
14. M. Born and E. Wolf, *Principles of Optics,* 6th ed. (Pergamon, New York, 1986; Nauka, Moscow, 1973).
15. Yu. I. Bogdanov, *Fundamental Problem of Statistical Data Analysis: Root Approach* (Mosk. Inst. Élektron. Tekh., Moscow, 2002) [in Russian]; physics/0211109.
16. Yu. I. Bogdanov, Opt. Spektrosk. **96**, 735 (2004) [Opt. Spectrosc. **96**, 668 (2004)].

Translated by R. Tyapaev